

Syntheses of Colloidal F:In₂O₃ Cubes: Fluorine-Induced Faceting and Infrared Plasmonic Response

Shin Hum Cho,^{†,‡,§} Sandeep Ghosh,^{†,‡,§} Zachariah J. Berkson,^{§,‡,§} Jordan A. Hachtel,^{||} Jianjian Shi,[‡] Xunhua Zhao,[‡] Lauren C. Reimnitz,[†] Clayton J. Dahlgren,^{†,‡,§} Yujing Ho,[†] Anni Yang,[†] Yuanyue Liu,^{‡,§} Juan-Carlos Idrobo,^{||} Bradley F. Chmelka,^{*,§,§} and Delia J. Milliron^{*,†,§}

[†]McKetta Department of Chemical Engineering and [‡]Texas Materials Institute and Department of Mechanical Engineering, The University of Texas at Austin, Austin, Texas 78712, United States

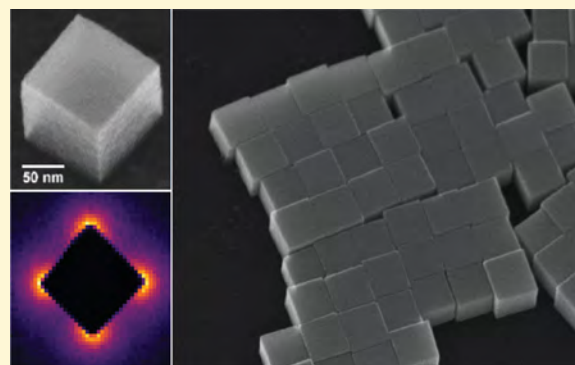
[§]Department of Chemical Engineering, University of California, Santa Barbara, Santa Barbara, California 93106, United States

^{||}Center for Nanophase Materials Science, Oak Ridge National Laboratory, Oak Ridge, Tennessee 37831, United States

[⊥]Materials Department, University of California, Santa Barbara, Engineering II Building 1355, Santa Barbara, California 93106-5050, United States

Supporting Information

ABSTRACT: Cube-shaped nanocrystals (NCs) of conventional metals like gold and silver generally exhibit localized surface plasmon resonance (LSPR) in the visible region with spectral modes determined by their faceted shapes. However, faceted NCs exhibiting LSPR response in the infrared (IR) region are relatively rare. Here, we describe the colloidal synthesis of nanoscale fluorine-doped indium oxide (F:In₂O₃) cubes with LSPR response in the IR region, wherein fluorine was found to both direct the cubic morphology and act as an aliovalent dopant. Single-crystalline 160 nm F:In₂O₃ cubes terminated by (100) facets and concave cubes were synthesized using a colloidal heat-up method. The presence of fluorine was found to impart higher stabilization to the (100) facets through density functional theory calculations that evaluated the energetics of F-substitution at surface oxygen sites. These calculations suggest that the cubic morphology results from surface binding of F atoms. In addition, fluorine acts as an anionic aliovalent dopant in the cubic bixbyite lattice of In₂O₃, introducing a high concentration of free electrons leading to LSPR. We confirmed the presence of lattice fluorine dopants in these cubes using solid-state ¹⁹F and ¹¹⁵In nuclear magnetic resonance spectroscopy. The cubes exhibit narrow, shape-dependent multimodal LSPR extinction peaks due to corner- and edge-centered modes. The spatial origin of these different contributions to the spectral response is directly visualized by electron energy loss spectroscopy in a scanning transmission electron microscope.



Typically, doping strategies in plasmonic metal oxide NCs (e.g., Sn:In₂O₃,¹¹ Al:ZnO,¹² and In:CdO¹³ NCs) have focused on aliovalent cation substitution. Halogen anions, meanwhile, can act as surface capping agents¹⁴ that have been used for shape control of metal,¹⁵ metal oxide,¹⁶ and metal chalcogenide^{17,18} NCs. In some metal oxide NCs, fluorine has been incorporated as an anionic co-dopant (e.g., F:In:CdO,¹⁹ F:Sn:In₂O₃²⁰). Very little has been reported regarding fluorine doping alone to induce LSPR, as in fluorinated TiO₂ NCs.²¹ Furthermore, whereas anionic doping in nanocrystalline F:SnO₂ has been demonstrated, the effects of fluorine on faceting or LSPR properties of metal oxide NCs have not been well explored.²² A comprehensive material characterization is yet needed to simultaneously unravel the

INTRODUCTION

Colloidal syntheses of doped metal oxide nanocrystals (NCs) have emerged recently as new means of extending localized surface plasmon resonance (LSPR) to the infrared (IR) range,¹ although shape control is yet to be broadly established.² A wide range of morphologies have been reported for colloidal gold and silver NCs,³ including cubes^{4,5} and octopods,⁶ leading to the observation of shape-dependent LSPR and strongly enhanced electromagnetic near-fields around corners and edges. Yet, metal NCs intrinsically possess high free carrier concentrations exceeding 10²³ cm⁻³ so the optical response of isotropic NCs tends to be restricted to the visible region of the electromagnetic spectrum.^{7,8} On the other hand, controlled doping of semiconductor NCs allows lower carrier concentrations around 10²¹ cm⁻³, resulting in IR-range LSPR.^{9,10} In this study, we demonstrate shape-controlled colloidal syntheses of highly faceted, fluorine-doped indium oxide (F:In₂O₃) cubes with an LSPR response in the IR range.

Typically, doping strategies in plasmonic metal oxide NCs (e.g., Sn:In₂O₃,¹¹ Al:ZnO,¹² and In:CdO¹³ NCs) have focused on aliovalent cation substitution. Halogen anions, meanwhile, can act as surface capping agents¹⁴ that have been used for shape control of metal,¹⁵ metal oxide,¹⁶ and metal chalcogenide^{17,18} NCs. In some metal oxide NCs, fluorine has been incorporated as an anionic co-dopant (e.g., F:In:CdO,¹⁹ F:Sn:In₂O₃²⁰). Very little has been reported regarding fluorine doping alone to induce LSPR, as in fluorinated TiO₂ NCs.²¹ Furthermore, whereas anionic doping in nanocrystalline F:SnO₂ has been demonstrated, the effects of fluorine on faceting or LSPR properties of metal oxide NCs have not been well explored.²² A comprehensive material characterization is yet needed to simultaneously unravel the

Received: March 5, 2019

Revised: March 11, 2019

Published: March 21, 2019

role of fluorine in LSPR-inducing internal doping and shape-inducing surface faceting effect for metal oxide NCs.

Faceted NCs give rise to shape-dependent LSPR phenomena not observed for spherical NCs, including highly enhanced near-field hot spots around corners and edges²³ that, in conventional metals, have been leveraged for plasmonic nanoantennae^{24,25} and surface-enhanced Raman spectroscopy.^{26,27} Shape effects and the understanding of plasmonic behavior have advanced in other classes of non-noble metal plasmonic materials, such as copper chalcogenides,^{28,29} and been extended in refractory metal nitrides.^{8,30,31} Disks and elongated NCs of copper chalcogenides have been reported in shape effects on their LSPR properties,²⁹ which are likely to be strongly influenced by crystalline anisotropy as well.³² Yet, shape-dependent studies of LSPR specific to doped metal oxide NCs are few,^{13,32} motivating the development of new strategies for synthetic shape control, as large cube NC sizes,²⁰ and well-defined corners¹⁰ can lead to higher magnitude in near-field enhancement for doped metal oxide NCs. Focal to this work, access to larger NC sizes with larger volume-to-surface ratios allow F:In₂O₃ NCs to be model materials in decoupling the roles of internal fluorine dopants and surface fluorine, supported by extensive material characterization and high spatial resolution for single-particle analysis.

We succeed in modulating the shape of F:In₂O₃ NCs by varying the ratio of InF₃ to In(acac)₃ precursors and observe multimodal shape-dependent LSPR extinction features. The role of fluorine in defining NC facets and inducing LSPR spectral response is attributed to the presence of fluorine on the external surfaces and internally within the NCs, respectively. Through X-ray photoelectron spectroscopy (XPS) and solid-state ¹⁹F magic-angle-spinning (MAS) nuclear magnetic resonance (NMR) spectroscopy correlated with density functional theory (DFT) calculations, fluorine is found to occupy surface sites on dominantly exposed {100} facets. Fluorine dopant species internal to the NCs are probed by X-ray diffraction (XRD), energy dispersive X-ray (EDX) spectroscopy, time of flight secondary ion mass spectrometry (TOF-SIMS), and ¹⁹F MAS-NMR spectroscopy. Aliovalent substitutional fluorine doping on oxygen lattice sites leads to free carrier compensation, inducing LSPR. The local metallic environments of the subsurface fluorine and indium atoms in the NC lattices are established by analyses of ¹⁹F spin-lattice *T*₁ relaxation times and wide-line ¹¹⁵In NMR spectra, which are shown to exhibit temperature and frequency dependencies that are characteristic of coupling to free (metallic) electron carriers. Arising from the free carriers and highly faceted NC shape, single-NC LSPR spatial modes are directly visualized by monochromated electron energy loss spectroscopy (EELS) performed in a scanning transmission electron microscope (STEM) to assign the observed multimodal features to distinct spatial dipolar modes. The observed material characteristics lead to IR light near-field localization, making F:In₂O₃ NCs a foundation material for near-field enhancement applications in IR.

EXPERIMENTAL METHODS

Materials. Indium(III) acetylacetonate (In(acac)₃, 99.99%), indium(III) fluoride (InF₃, >99.9%), indium(III) chloride (InCl₃, 99.999%), indium(III) bromide (InBr₃, 99.999%), oleic acid (OA, 90%, technical grade), octylamine (OcAm, 99%), trioctylamine (TOA, 98%), and tetrachloroethylene (TCE, ≥99%) were purchased from Sigma-Aldrich. Toluene (99.5%) was purchased from Fisher

Chemical. All chemicals were used as received without any further purification.

Fluorine-Doped Indium Oxide (F:In₂O₃) Cube (3% InF₃) Synthesis. All synthesis procedures were carried out using standard Schlenk line techniques aided by a nitrogen-filled glovebox. For the growth of 3% doped F:In₂O₃ cubes, a mixture of In(acac)₃ (399.78 mg, 0.97 mmol), InF₃ (5.15 mg, 0.03 mmol), OA (1 mL), OcAm (0.5 mL), and TOA (3.5 mL) was loaded in a three-neck round-bottom flask in the glovebox. This precursor mixture was then stirred with a magnetic bar at 600 rpm and degassed under vacuum at 120 °C for 15 min. The mixture turned transparent during this operation, signifying the formation of indium oleate (In-OA). Thereafter, the flask was filled with nitrogen and further heated at a ramp rate of 15 °C/min to 320 °C. The reaction mixture turned cloudy and opaque, which signified cube growth and was designated as the growth reaction start time. The growth reaction was allowed to run for 5 min at 320 °C or the desired set point temperature. Subsequently, growth was terminated by removing the heating mantle and the reaction mixture was cooled by blowing an air jet on the flask. The cubes were washed and dispersed in toluene and centrifuged at 4500 rpm for 5 min. This washing process was repeated three times. The resultant cubes were redispersed in toluene for further analysis.

Varying concentrations of F doping in these NCs were achieved by controlling the molar ratio of InF₃ to In(acac)₃, while keeping other reaction parameters identical. Aliquots (0.1 mL), at various reaction times during growth, were extracted from the reaction mixture with a nitrogen-purged syringe needle and quenched into TCE for further analysis.

Indium Oxide (In₂O₃) NC Synthesis. Undoped indium oxide (In₂O₃) NCs were synthesized by adding In(acac)₃ (1 mmol) in the reaction flask without InF₃ while keeping other reaction parameters identical to the procedure described above for the F-doped NCs.

Chlorine/Bromine-Doped Indium Oxide (Cl:In₂O₃, Br:In₂O₃) NC Synthesis. Cl:In₂O₃ (3% InCl₃) NCs were synthesized by adding In(acac)₃ (0.97 mmol), substituting InCl₃ (0.03 mmol) precursor for InF₃ in the reaction flask, while keeping other reaction parameters identical. In a similar manner, InBr₃ (0.03 mmol) was used to synthesize Br:In₂O₃ (3% InBr₃) NCs, keeping other reaction parameters identical.

Fourier Transform IR (FTIR) Spectra. FTIR spectral measurements were conducted using a Bruker Vertex 70 FTIR at 4 cm⁻¹ resolution. Aliquot solutions were diluted in TCE and loaded into a liquid cell with KBr windows for FTIR measurements. NCs dispersed in TCE were sonicated for 1 h to prevent aggregation before loading into the liquid cell.

XRD Analysis. Samples for XRD measurements were prepared by drop-casting a 10 mg/mL dispersion of F:In₂O₃ NCs on silicon substrates. The data were collected with a Rigaku MiniFlex 600 X-ray diffractometer using Cu K α radiation, 1.54 Å, and analyzed with GSAS-II software.³³

Electron Microscopy. Samples were prepared by drop-casting NC dispersions onto carbon-coated 400 mesh copper grids (Ted Pella), and the imaging was performed in a Hitachi S5500 scanning electron microscope (SEM) operating in the STEM mode at an accelerating voltage of 30 kV. NC size analysis was performing with ImageJ software with 250 NC count. High-resolution transmission electron microscopy (HRTEM) images and selected-area electron diffraction (SAED) patterns were acquired with a JEOL 2010F transmission electron microscope (TEM) equipped with a charge-coupled device camera and a Schottky field emission gun operating at 200 kV.

Elemental Analysis. Elemental spectrum acquisition of F:In₂O₃ cubes drop-cast on silicon substrates was carried out using a Hitachi S5500 SEM with a Bruker XFlash EDX detector attachment at 5 kV. Elemental deconvolution was performed with the Bruker Quantax software reference library at zero-tilt angle P/B-ZAF correction. TOF-SIMS was conducted on TOF.SIMS 5, ION-TOF GmbH with Cs⁺ sputtering at 2 kV.

Thermogravimetric Analysis (TGA). Measurements were carried out using a Mettler Toledo TGA2 thermogravimetric analyzer.

Dried NC powders were loaded into alumina crucibles of 100 μL volume and heated from 25 to 1100 $^{\circ}\text{C}$ at a heating rate of 5 $^{\circ}\text{C}/\text{min}$ under nitrogen flow (50 sccm).

XPS. Samples were prepared by drop casting NC solutions on silicon substrates, and the measurements were performed in a Kratos Axis Ultra DLD spectrometer with a monochromatic Al $K\alpha$ source (1486.6 eV). Wide survey scans were acquired at analyzer pass energy of 80 eV, and the high-resolution narrow region scans were performed at a pass energy of 20 eV with steps of 0.1 eV. Spectral acquisitions were performed with photoelectron take-off angle at 0° with respect to the surface normal, and pressure in the analysis chamber was maintained at around 10^{-9} Torr. Data analysis was performed in CasaXPS software using the Kratos relative sensitivity factor library. The binding energy (BE) scale was internally referenced to the C 1s peak (BE for C–C = 284.8 eV).

DFT Calculations. DFT calculations were performed using the Vienna Ab initio Simulation Package (VASP)^{34,35} with projector augmented wave pseudopotentials³⁶ in the package. The Perdew–Burke–Ernzerhof exchange–correlation functional³⁷ was used in all DFT calculations. A $3 \times 3 \times 1$ Monkhorst–Pack k point mesh for the Brillouin zone integration was used, with a vacuum layer of 15 \AA to prevent interactions between periodic images of the slab. Further details are in Text S1, Supporting Information.

Solid-State ^{19}F and ^{115}In NMR Spectroscopy. Solid-state ^1H and ^{19}F MAS-NMR spectra were acquired on a Bruker ASCEND 400 MHz (9.4 T) solid-state dynamic nuclear polarization NMR spectrometer operating at Larmor frequencies of 400.202 and 376.532 MHz for ^1H and ^{19}F , respectively, and equipped with a variable temperature 2.5 mm triple-resonance H–F–X probehead. For the solid-state MAS-NMR measurements, the $\text{F}:\text{In}_2\text{O}_3$ NCs were mixed with KBr powder in a 1:1 ratio by mass. The KBr served as an internal temperature probe for accurate determination of the sample temperature under the different measurement conditions.^{38,39} The one-dimensional (1D) ^{19}F Hahn echo spectrum was acquired at 35 kHz MAS, at 395 K, and using a $90^{\circ}-\tau-180^{\circ}-\tau$ pulse sequence with rotor-synchronized τ delay times of one rotor period and 100 kHz radio frequency (rf) pulses. The two-dimensional (2D) $^1\text{H}\{^{19}\text{F}\}$ NMR correlation spectrum was acquired by using a 2D dipolar-mediated heteronuclear multiple quantum correlation (HMQC) pulse sequence, where the ^1H – ^{19}F nuclear dipole–dipole couplings were reintroduced by using SR26₄¹¹ recoupling⁴⁰ with 50 kHz rf power for recoupling. The ^{19}F spin-lattice (T_1) relaxation analyses relaxation times at different temperatures were measured by using a saturation-recovery pulse sequence with a Hahn echo detection.

The solid-state ^{115}In NMR spectrum of undoped bulk polycrystalline In_2O_3 (99.9% purity, Aldrich) was acquired on a Bruker AVANCE-III Ultrashield Plus 800 MHz (18.8 T) narrow-bore spectrometer operating at a Larmor frequency of 174.354 MHz for ^{115}In and using a Bruker 3.2 mm broadband double-resonance H–X probehead. The solid-state ^{115}In NMR spectrum of the $\text{F}:\text{In}_2\text{O}_3$ NCs was acquired on a 19.6 T Bruker DRX NMR spectrometer (National High Magnetic Field Laboratory) operating at a Larmor frequency of 182.266 MHz for ^{115}In and using a custom-built 3.2 mm double resonance H–X probehead. The ^{115}In NMR spectra were acquired using a quadrupolar Carr–Purcell–Meiboom–Gill (QCPMG) pulse sequence,⁴¹ which yields manifolds of very narrow, evenly spaced NMR signals (spikelets), which can be systematically acquired as a series that can be overlaid to map the full central transition (CT) region of the ^{115}In NMR spectra. Each ^{115}In NMR spectrum is presented as a mosaic overlay of 22 individual QCPMG subspectra (plotted in different colors) acquired at evenly spaced frequency intervals. The ^{115}In spectra were referenced to a 1 M $\text{In}(\text{NO}_3)_3$ solution at 0 ppm. Further details on the ^{19}F and ^{115}In NMR analyses are provided in Text S2, Supporting Information.

STEM-EELS. Plasmon mapping was performed in a Nion high-energy-resolution monochromated EELS STEM at Oak Ridge National Laboratory operated at 60 kV and a Nion prototype spectrometer.^{42,43} Using a variable slit we choose an energy resolution of 186 cm^{-1} (23 meV) to optimize the resolution between the plasmon peaks and the signal in the monochromated beam. For the

plasmon deconvolution, we use the non-negative matrix factorization (NMF) routine available in the Python HyperSpy library (<http://hyperspy.org/>). More details can be found in the Supporting Information (Text S3).

RESULTS AND DISCUSSION

NC Shape Control. The shapes of the $\text{F}:\text{In}_2\text{O}_3$ NCs were controlled by varying the molar ratio of InF_3 to $\text{In}(\text{acac})_3$ precursors during synthesis, which also determined the extent of fluorine incorporation in the resulting NCs. $\text{F}:\text{In}_2\text{O}_3$ NCs with well-defined morphology were produced for 1–3% InF_3 in the growth solution, as shown in Figure 1. SEM images

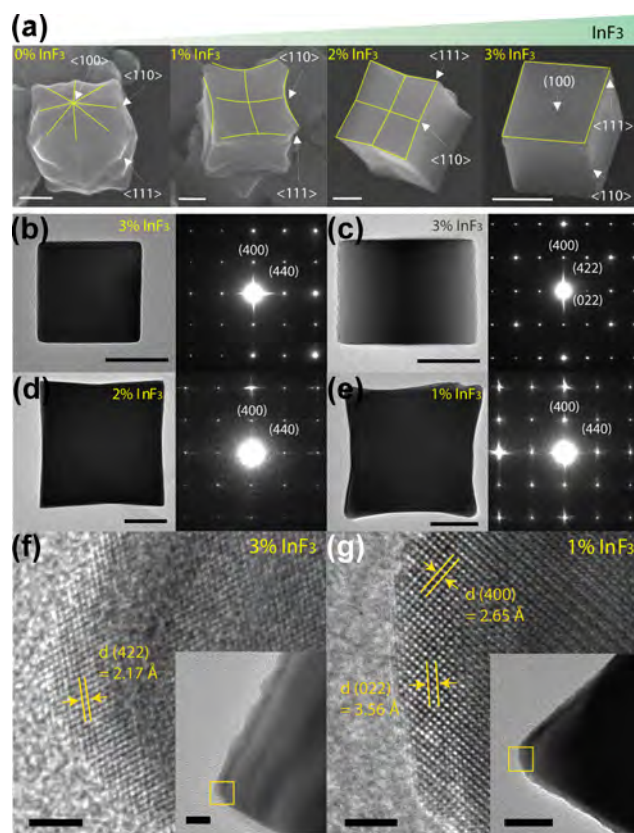


Figure 1. (a) SEM images showing the progressive effect of F on In_2O_3 NC morphology. Outlines are shown as guides to visualize the indicated facets. TEM images (left panels) and the corresponding SAED patterns (right panels) of (b) cube, (c) edge-oriented cube, (d) sharp concave cube, and (e) concave cube $\text{F}:\text{In}_2\text{O}_3$ NCs. Scale bars are 100 nm for (a)–(e). (f) HRTEM image of a single $\text{F}:\text{In}_2\text{O}_3$ cube corner with NC oriented on its edge (inset). (g) Extended corner of concave cube $\text{F}:\text{In}_2\text{O}_3$ NC (inset). Scale bars are 2 nm in (f) and (g) and 20 nm in the insets.

showed that monodisperse NCs (edge length $162.1 \pm 9.2 \text{ nm}$) with cubic morphology were obtained exclusively in the presence of InF_3 (3% in the molar ratio to $\text{In}(\text{acac})_3$) (Figure 1a, rightmost panel). By comparison, in the absence of InF_3 , during the synthesis, NCs with pseudospherical morphology were observed (Figure 1a, leftmost panel), with no cubic-shaped NCs observed. Intermediate amounts of InF_3 led to variations in the NC morphology, specifically forming concave cubes with edges protruding outward for 2% InF_3 (Figure 1a, second from right) and 1% InF_3 (Figure 1a, second from left). The cube morphology persists for higher concentrations of InF_3 (4 and 5%) as well, until a threshold is reached at 6%

Table 1. EDX Quantification of Fluorine in F:In₂O₃ NCs Synthesized with 1–12% InF₃ Precursor, and Halide Quantification for NCs Synthesized with 3% InCl₃ and 3% InBr₃ Precursors^a

sample	precursor In(acac) ₃ /InX ₃ (mmol)	initial at. X/In %	measured X/In % (EDX)	measured F/In % (TOF-SIMS)
1% InF ₃	0.99:0.01	3.0	6.65 ± 0.48	2.7
2% InF ₃	0.98:0.02	6.0	8.56 ± 1.59	9.2
3% InF ₃	0.97:0.03	9.0	11.76 ± 2.70	10.3
6% InF ₃	0.94:0.06	18.0	26.40 ± 0.36	22.7
12% InF ₃	0.88:0.12	36.0	30.58 ± 2.40	30.6
3% InCl ₃	0.97:0.03	9.0	0.32 ± 0.11	
3% InBr ₃	0.97:0.03	9.0	2.62 ± 0.06	

^aThe EDX fluorine quantification in F:In₂O₃ NCs is accompanied by TOF-SIMS results.

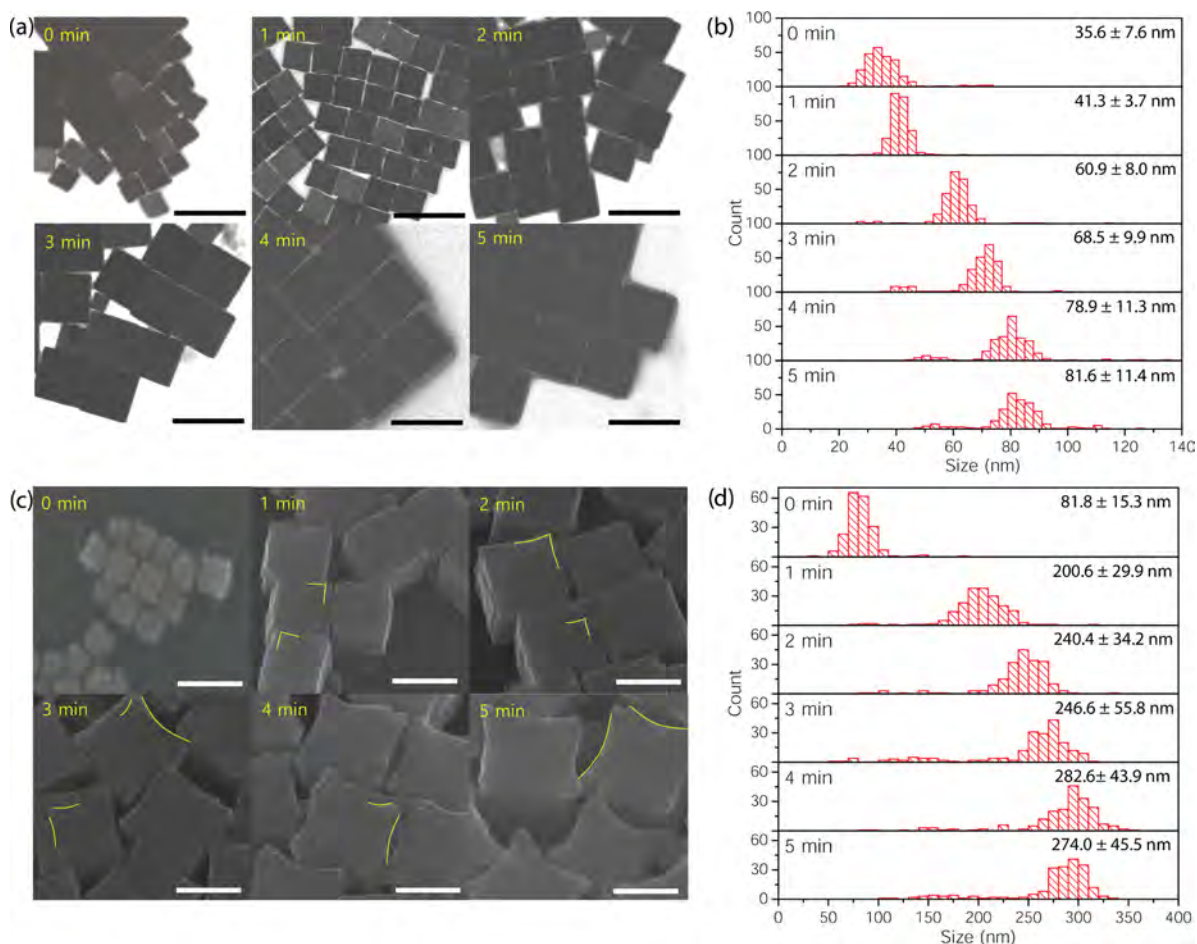


Figure 2. (a) SEM images of aliquots taken at different stages of F:In₂O₃ (3% InF₃) cube synthesis (0–5 min). Scale bars are 100 nm. (b) Size distribution histograms for the corresponding F:In₂O₃ cube aliquots (panel (a)) taken during the growth progression (250 particle count). (c) SEM images of aliquots taken during the growth of F:In₂O₃ (1% InF₃) concave cubes (0–5 min). Yellow lines are drawn as a visual guide to follow the gradual ledge-converging to eventually form the elongated corners. Scale bars at 200 nm. (d) Size distribution histograms for the corresponding F:In₂O₃ concave cube aliquots (panel (c)).

InF₃, beyond which NCs exhibit roughened surfaces (Figure S2).

The TEM images in Figure 1 show that the as-synthesized F:In₂O₃ cubes exhibit well-defined crystalline facets. Selected area electron diffraction (SAED) confirms that the F:In₂O₃ cubes are each single crystals and allows indexing of their surface facets. A TEM image of an F:In₂O₃ cube (3% InF₃) is shown in Figure 1b, which exhibits a flat (100) face and a well-defined edge. The cube is terminated with (100) facets of the In₂O₃ cubic bixbyite structure, corroborated by the position of the (400) reflections in the SAED pattern (Figure 1b, right). A cube on <110> zone axis orientation exhibits (422) reflections

in the SAED pattern (Figure 1c, right), corresponding to the (422) spacings observed by HRTEM (Figure 1f). Concave F:In₂O₃ cubes (1 and 2% InF₃) are also single crystalline, as observed in SAED patterns collected down the <100> zone axis (Figure 1d,e right). An HRTEM image of the elongated tip on a concave cube (1% InF₃) shows (022) lattice spacing (3.56 Å), along with (400) lattice spacing parallel to the facets (Figure 1g). Together, these observations indicate that the as-synthesized F:In₂O₃ cubes have cubic bixbyite {100}-dominant surface facets.

To quantify total fluorine incorporation in F:In₂O₃ NCs (Table 1), EDX spectroscopy (Figure S3) and TOF-SIMS

analysis were conducted (Figure S4). Because the emitted X-rays are of high energy, EDX has an effective probe depth of about 200 nm; the entire volume of the NCs is probed, and the results approximately reflect the overall F/In atomic (at.) composition ratio. However, owing to the low sensitivity of EDX to fluorine in the low-dopant-concentration NC samples, (e.g., 1% InF₃), TOF-SIMS was employed to quantify the F/In atomic ratio as a film of NCs was progressively etched. Both EDX and TOF-SIMS support a trend of increasing F atomic composition in F:In₂O₃ NCs as a function of InF₃ concentration employed during synthesis. Lower F/In was observed in 12% InF₃ when compared with the initial F/In, suggesting fluorine saturation within the NC lattice under excessive addition of dopant precursor. Syntheses with InCl₃ and InBr₃ precursors were observed to result in low halide (X = Cl, Br) incorporation instead.

Aliquots taken during the synthesis of F:In₂O₃ cubes (3% InF₃) were analyzed by FTIR spectroscopy to assess the chemical decomposition mechanism. Typically, In(acac)₃ and oleic acid were heated at 120 °C to form an indium oleate (In-OA) precursor. For F:In₂O₃ NCs, a ramp rate of 15 °C/min to 320 °C was used to rapidly decompose the indium precursors. In-OA and octylamine (OcAm) lead to the formation of indium monomers and amide by-products^{44,45} (Figure S5). The FTIR fingerprint region shows that the precursor undergoes an aminolysis reaction with OcAm during synthesis. The metal carboxylate (1614 and 1582 cm⁻¹) peak signals^{46,47} are significantly reduced in intensity after heating to 260 °C and continue to fall as the reaction progresses from 0 to 5 min, past this point. Concurrently, amide by-product C=O stretching (1688 cm⁻¹) and N–H bending (1651 cm⁻¹) signals^{48,49} increase as In-OA is decomposed (Figure S5). These observations indicate that aminolysis is a primary mechanism of growth, which entails nucleophilic attack of the alkylamine on the metal–alkylcarboxylate complex, which is a common NC growth mechanism for metal oxides.^{50,51} An aliquot taken during decomposition at 280 °C showed small irregularly shaped particles indicative of aggregative nucleation (Figure S5).⁵² Irregular nuclei cohere together through oriented attachment, as observed in HRTEM, resulting in large sized NC seeds. Average NC product yield was 54.3% by weight for all F:In₂O₃ NC samples. Differing from typical doped In₂O₃ NC syntheses,⁵³ such large sized (100 nm scale) NCs are enabled by a combination of aminolysis-driven growth, aggregative nucleation, and a concentrated precursor solution (0.2 mmol/mL) at a high reaction temperature (320 °C).

To evaluate the progression of NC shape with reaction time, SEM analyses were performed on aliquots collected during the growth of F:In₂O₃ cubes. As reaction time progresses and the precursors progressively decompose, NC size is expected to increase, accompanied by either shape retention or changes. Aliquots taken during the growth of F:In₂O₃ cubes (3% InF₃) show that the cube morphology is retained throughout the 5 min growth period (Figure 2a) as size increases from 35.6 ± 7.6 to 81.6 ± 11.4 nm (Figure 2b). This indicates {100} surface stabilization throughout growth at sufficient InF₃ concentration, allowing synthesis of well-defined cube-shaped NCs. The cubic morphology was established after an initial nuclei aggregation phase as irregular aggregates became cubic during growth. Aliquots over longer reaction times (at 5 min, 30 min, 1 h, and 2.5 h) at 320 °C were also taken to observe the morphology evolution. At extended reaction times, corner

rounding was observed. At longer reaction times of 2.5 h or more, the well-defined edge and corner morphology becomes a truncated cube with the appearance of {111} facets at the cube edges (Figure S6). At even longer growth times, pitting is apparent on the {100} facets, potentially due to corrosion by F⁻ ions or their reaction by-products.^{14,15}

For the concave F:In₂O₃ cubes (1% InF₃), SEM images of aliquots reveal progressive growth at the corners that results in morphological evolution (Figure 2c). The initial aliquot, taken when turbidity was first observed in the reaction flask (0 min), shows cube-shaped NCs that are 81.3 ± 15.3 nm in size. SEM images show a second stage involving rapid NC size growth (Figure 2d) and observation of ledges on the faces. In the final stage, ledges converge into elongated tip extensions that project in the <111> directions, from the corners. A smooth concave surface has replaced the flat {100} cube facets in the final 5 min aliquot to form 274.0 ± 45.5 nm sized F:In₂O₃ concave cubes with elongated corners. This suggests that the {100} facets may not be as stable for this case, compared with the cubes synthesized with 3% InF₃ in the reaction mixture. At longer reaction times of 2.5 h or more, further rounding of the elongated corners occurs (Figure S6).

The synthesis of well-defined F:In₂O₃ cubes was also found to depend on the reaction temperature. For the 3% InF₃ synthesis, which produced optimally structured cubes at 320 °C, the morphological evolution was studied for reactions at temperatures between 280 and 340 °C. Strongly faceted cube shapes were produced at reaction temperatures of 340 and 320 °C (Figure S6). However, at a lower reaction temperature (280 °C), smaller rounded cubes were observed after 5 min of reaction time, evolving after 30 min to more defined cubic shapes.

The concave cube morphology is more sensitive to reaction temperature. Synthesizing F:In₂O₃ NCs (1% InF₃) at an elevated reaction temperature (340 °C) resulted in irregular pseudospherical shapes with growth in randomly oriented directions (Figure S6). Apparently, the preference for growth in the <111> direction is weakened at higher growth temperatures, which is consistent with growth occurring without directional preference potentially due to enhanced monomer diffusion along the surface at high temperatures.⁵⁴ Synthesizing F:In₂O₃ NCs (1% InF₃) at a lower reaction temperature (280 °C) resulted in rounded NCs instead of a concave cube morphology, up to 2.5 h of reaction time (Figure S6).

Influences of Fluorine on NC Shape. SEM and HRTEM analyses indicate that fluorine has a facet-directing function in the growth of F:In₂O₃ NCs. The cube-shaped NCs were produced only in the presence of fluorine (Figure 1a, right), whereas the cubic shape is not observed in its absence (Figure 1a, left). To assess whether fluorine is unique compared with other halides as a morphology-directing agent under these synthesis conditions, InCl₃ and InBr₃ were used in place of InF₃. The bond dissociation energy is 439 kJ/mol for the In–Cl bond and 418 kJ/mol for the In–Br bond, which are lower than that for In–F at 506 kJ/mol.⁵⁵ In–F bonds, being stronger than In–O bonds (at 360 kJ/mol), are hypothesized to be highly stable at In₂O₃ NC surfaces, whereas weaker In–Cl or In–Br bonds are less favorable due to lower electronegativity than that of fluorine and differing ionic radii (Cl⁻: 1.81 Å and Br⁻: 1.96 Å) causing strain when substituting surface oxygen (O²⁻: 1.28 Å).^{14,56} The NC products synthesized in the presence of InCl₃ or InBr₃ were large and

rounded: 246.7 ± 16.6 nm for Cl:In₂O₃ NCs and 348.3 ± 58.1 nm for Br:In₂O₃ NCs with poorly defined facets (Figure S7), whereas F:In₂O₃ cubes synthesized with the same precursor ratio had well-defined shapes with edge lengths of 162.1 ± 9.2 nm (Figure S1).

Since fluorine plays an important role in the faceting of the In₂O₃ NCs, XPS was used to probe the presence of fluorine on their surfaces. XPS is sensitive to surface composition, since the escape depth of photoelectrons is only a few nanometers. The existence of fluorine on the F:In₂O₃ NC surfaces was revealed by XPS spectra acquired for the In 3d (Figure 3a) and F 1s (Figure 3b) regions. As shown in Figure 3a, the In 3d_{5/2} signal was deconvoluted into components that are assignable to lattice In–O (444.3 eV), In–OH (445.0 eV), and In–F (445.8 eV) species,⁵⁷ with the peak due to the In–F species becoming more dominant as the InF₃ precursor concentration is increased. Furthermore, the F 1s peak at 684.6 eV, flanked by the In 3p doublet peaks, also exhibits an increase in relative intensity as the InF₃ precursor concentration is increased (Figure 3b). Deconvolution of the O 1s signal is shown in Figure S8, with components that are assignable to lattice oxygen (530.0 eV), oxygen adjacent to oxygen vacancies, or other charged defects, such as F_O[•] (531.0 eV), surface hydroxyl (531.8 eV), and carboxyl (533.1 eV) species, respectively.⁵⁷ Overall, the undoped In₂O₃ NCs are observed to have more surface-adsorbed hydroxyl and carboxyl species, as compared to F:In₂O₃ NCs, which further signifies the incorporation of F species as surface-capping agents. XPS characterization thus suggests that fluorine adsorbs on the In₂O₃ NC surfaces, which may be linked to the stability and prevalence of {100} facets in cube-shaped NCs.

Fluoride anions have been described as facet-directing agents in metal oxide NCs,¹⁴ such as in the fluorinated synthesis of TiO₂ NCs,^{21,56} and may also have played this role in the synthesis of F and Sn co-doped In₂O₃ NCs.²⁰ Metal fluoride precursors, such as InF₃, decompose into HF in the presence of oleic acid during the reaction, releasing fluoride anions and passivating the In–O surfaces with In–F bonds.²¹ Walsh et al.⁵⁸ determined through density functional theory (DFT) calculations that for bixbyite In₂O₃, relaxed {111} facets are energetically preferred over oxygen-terminated {100} facets ($\gamma_{(111)} < \gamma_{(100)}$). However, surface passivation by F[−] in metal oxide NCs can be expected to alter the energetic sequence of the facets: F[−] passivation of the {100} facets results in surface energy inversion ($\gamma_{(111)} > \gamma_{(100)}$).⁵⁶ Correspondingly, F[−] functions as a favorable {100} facet capping agent over {111} in the bixbyite In₂O₃ NCs, which we expect hinders growth at F[−] terminated {100} surfaces due to fewer O sites available for In–OH monomer condensation to occur. We suggest that this directs the synthesis of well-defined F:In₂O₃ cube NCs (3% InF₃) wherein sufficient F[−] passivation occurs at the {100} facets.

To understand the surface effects of fluorine on the morphology of In₂O₃, DFT calculations were conducted (details in Text S1, Supporting Information) by calculating relative formation energies of F substituting at surface O atomic sites on (100) and (111) surfaces. The (111) surface was selected for comparison with (100) as it has been reported to have the lowest surface energy in In₂O₃ without F doping.⁵⁸ All possible F substitution sites were considered, and only the low formation energy surface configurations are shown in Figure 3c,d. F substitution is more energetically favorable on the (100) surfaces than the (111) surfaces, with F substitution

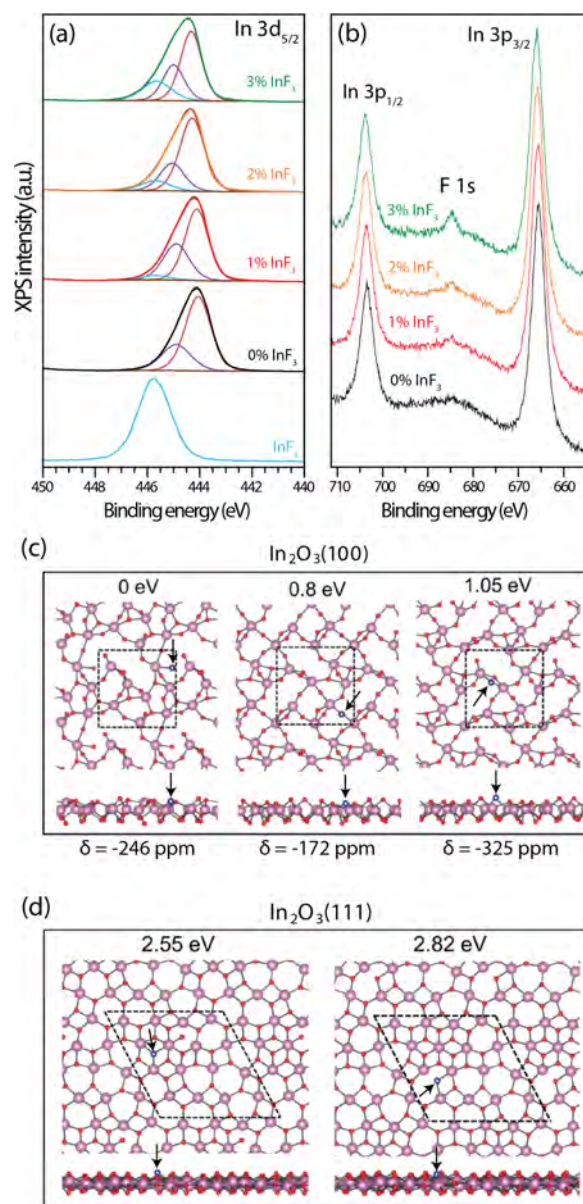


Figure 3. Rationalizing F incorporation in the F:In₂O₃ NCs by XPS and DFT. (a) In 3d_{5/2} XPS spectra showing the contributions of various components (red = In–O, purple = In–OH, and blue = In–F), and (b) F 1s (along with In 3p) XPS spectra for undoped In₂O₃ NCs (black curve), concave cubes (red curve), sharp concave cubes (orange curve), and cubes (green curve). Note that the In–F component (blue curve in panel (a)) increases in intensity as the InF₃ concentration used during synthesis is increased. In 3d_{5/2} spectrum for InF₃ is shown for reference (blue curve, bottom). DFT-calculated top and side views of an F atom substituting O on (c) (100) surface, and (d) (111) surface. Red: O; purple: In; blue: F (marked with arrows). For clarity, only the top In layer and the coordinated O and F are shown. The number on top of each panel shows the corresponding formation energy of the F/O substitution (see the Supporting Information) with respect to the most stable configuration (c, left). δ_{iso} is the calculated NMR isotropic chemical shift. Only low-energy structures for each surface are shown.

at (111) surfaces yielding formation energies (2.55, 2.82 eV) that are higher than the (100) surface configurations. Since growth through monomer deposition requires addition of new In and O atoms on oxygen-terminated sites,⁵⁹ it can be expected that this process is more difficult at fluorine-capped

(100) surfaces than on (111) surfaces. This explains why the (100) facets grow more slowly and become the dominant NC surface. NMR chemical shifts of ^{19}F atoms in different configurations on the (100) surface are calculated, with the most stable structure (Figure 3c, left) corresponding to a chemical shift of -246 ppm, to be compared below to experimental ^{19}F NMR spectra.

The complex concave cube shape of moderately passivated $\text{F}:\text{In}_2\text{O}_3$ NCs (1% InF_3) can be rationalized through the shape control model previously described for other halide-passivated NCs.^{14,15} Colloidal syntheses of NCs involve both thermodynamic and kinetic effects that impact the NC shape. The conceptual framework involves two monomer addition processes: deposition on facets with high surface energy (kinetic) and monomer surface diffusion to minimize the total surface energy of NC facets (thermodynamic).³ The high rate of In-OA precursor decomposition, driven by aminolysis, leads to a high rate of monomer deposition onto growth-favorable NC facets at a short reaction time (5 min). During fluorine-free synthesis, undoped In_2O_3 NCs exhibit growth in all $\langle 100 \rangle$, $\langle 110 \rangle$, and $\langle 111 \rangle$ directions into irregularly shaped NCs (Figure 1a, leftmost panel). With intermediate InF_3 concentrations (1–2% InF_3), the $\{100\}$ facets are partially capped by F^- , and In monomer deposition becomes unfavorable on $\{100\}$ facets with more F^- capped sites. Instead, the reaction conditions are favorable for selective monomer deposition on the less F^- surface occupied $\{111\}$ facets. Thus, F^- passivated $\{100\}$ facets have slower growth and monomers preferentially deposit on $\{111\}$ facets during NC growth.⁶⁰ Through this process, elongated $\langle 111 \rangle$ direction tips are seen in $\text{F}:\text{In}_2\text{O}_3$ concave cube NCs (1% InF_3), with concave $\{100\}$ facets (Figure 1a, second from left). Well-defined concave cube $\text{F}:\text{In}_2\text{O}_3$ NCs of 290.4 ± 17.9 nm size with sharp elongated $\langle 111 \rangle$ corners result when using a 2% InF_3 precursor content, showing distinct high-index quadrant boundaries on the $\{100\}$ facets (Figure 1a, second from right). With higher InF_3 concentration (3% InF_3), the $\{100\}$ facets become increasingly passivated by F^- capping, fluorine-terminated $\{100\}$ surface exposure is favored for minimizing the total surface energy, and well-defined cube-shaped NCs result.

Since metal oxide NC growth through monomer deposition requires addition of new In and O atoms on oxygen-terminated sites, the observed NC growth in higher InF_3 precursor ratio reaction is expected to be slower due to fluorine termination on the NC surfaces. This slower growth leads to the smaller NC size in 3% InF_3 compared to that in 1% InF_3 throughout the growth aliquot observed in Figure 2. Due to aggregative nucleation,⁵² we rationalize that the aggregative nuclei is also less prone to cohesion due to fluorine passivation of the oxygen-terminated NC nuclei surface. A higher InF_3 precursor would lead to smaller sized seeds and indicate a larger number of nuclei. The NC aliquot size in Figure 2 (0 min in Figure 2) is smaller in 3% InF_3 growth (35.6 nm) compared to that in a lower level of 1% InF_3 precursor (81.8 nm).

Although the XRD and electron diffraction patterns indicate substantial long- and short-range lattice order in the $\text{F}:\text{In}_2\text{O}_3$ NCs, the nonstoichiometric distributions of fluorine species introduce significant and important complexity to the NC structures that govern their growth and optical properties. The types, distributions, and electronic environments of fluorine atoms in $\text{F}:\text{In}_2\text{O}_3$ NCs are established by solid-state ^{19}F MAS NMR analyses. The solid-state 1D ^{19}F MAS NMR spectrum of $\text{F}:\text{In}_2\text{O}_3$ NCs (3% InF_3) in Figure 4a reveals four resolved ^{19}F

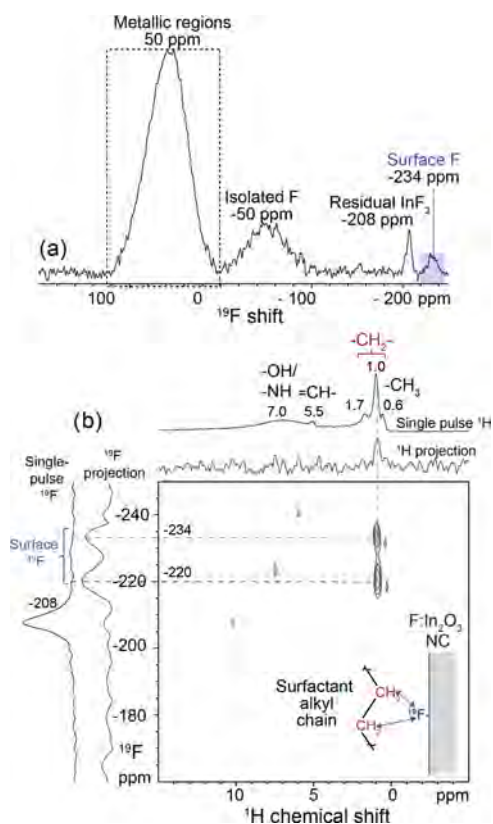


Figure 4. Solid-state (a) 1D ^{19}F echo and (b) 2D $^1\text{H}\{^{19}\text{F}\}$ correlation MAS NMR spectra of $\text{F}:\text{In}_2\text{O}_3$ NCs (3% InF_3) diluted in a 1:1 ratio by mass with KBr . Solid-state 1D single-pulse ^1H and ^{19}F spectra acquired under the same conditions are shown along the horizontal and vertical axes of the 2D spectrum in (b) for comparison with the 1D projections. The inset shows a schematic diagram of a surface ^{19}F moiety interacting with the alkyl chain of a surface-bound organic ligand, as indicated by arrows. The spectra were acquired at 9.4 T, (a) 35 kHz MAS and 395 K or (b) 25 kHz MAS and 327 K.

signals at 50, -50 , -208 , and -234 ppm, which are assigned on the basis of the 2D $^1\text{H}\{^{19}\text{F}\}$ NMR correlation spectrum and ^{19}F spin-lattice relaxation time analyses discussed below to ^{19}F nuclei in different types of chemical and electronic environments in the $\text{F}:\text{In}_2\text{O}_3$ NCs.

Importantly, dilute surface fluorine moieties are detected and identified in the solid-state two-dimensional (2D) $^1\text{H}\{^{19}\text{F}\}$ correlation NMR spectrum in Figure 4b. The spectrum is shown as a 2D contour plot, having ^1H and ^{19}F frequency axes (with units of ppm) on the abscissa and ordinate, respectively. Correlated signal intensities in the 2D spectrum arise only from ^1H species that are dipole–dipole-coupled with ^{19}F atoms over nanoscale distances (<0.5 nm for the short dipolar recoupling time, 0.96 ms, used here), thereby establishing the mutual proximities of the ^1H and ^{19}F species with associated signals. For comparison, a standard 1D ^1H MAS NMR spectrum is shown above the ^1H axis of the 2D spectrum, which exhibits signals at 0.6, 1.0, 1.7, 5.5, and 7.0 ppm that are all assigned to ^1H moieties on the octylamine, trioctylamine, or oleate organic surfactant molecules, as indicated by the labels above the respective ^1H signals. The 2D $^1\text{H}\{^{19}\text{F}\}$ correlation spectrum resolves two ^{19}F signals at -234 and -220 ppm that are correlated to ^1H signals at 1.0 ppm from $-\text{CH}_2-$ moieties on the organic surfactant molecules, unambiguously establishing the interactions and proximities of the corresponding ^1H

and ^{19}F species at the $\text{F}:\text{In}_2\text{O}_3$ particle surfaces. Notably, no correlated signal intensity is observed for the relatively narrow ^{19}F signal at -208 ppm (6 ppm full width half-maximum, FWHM), which is assigned to residual InF_3 precursor species.⁵¹ Furthermore, whereas ^1H signal intensity is detected in 1D $^1\text{H}\{^{19}\text{F}\}$ NMR spectra acquired with ^{19}F excitation at -210 ppm, the same excitation frequency was used to acquire the 2D spectrum in Figure 4b, no ^1H signal intensity is detected for ^{19}F excitation at different frequencies (Figure S10). These results indicate that only the ^{19}F signals in the -220 to -234 ppm frequency range correspond to ^{19}F surface species and that the other types of ^{19}F environments detected in the 1D ^{19}F MAS NMR spectra in Figure 4a are located in subsurface environments, within the detection limits of the NMR measurements.

From the quantitative single-pulse 1D ^{19}F MAS NMR spectrum (Figure S11), the ^{19}F signals in the frequency range from -220 to -234 ppm account for only 1–2% of all the ^{19}F signal intensity, indicating that <2% of all of the ^{19}F species in the $\text{F}:\text{In}_2\text{O}_3$ NCs are in surface environments. These surface-related ^{19}F signals in the range of -220 to -234 ppm are close to the shift values predicted by DFT calculations for the most energetically stable ^{19}F structure on the (100) surface (-246 ppm, Figure 3c, left). Although the DFT models neglect other possible adsorbates for computational simplicity and represent an idealized subset of numerous possible surface configurations, this agreement suggests that the DFT calculations capture the main effects of fluorine on the (100) surface. The combined solid-state 1D ^{19}F and 2D $^1\text{H}\{^{19}\text{F}\}$ NMR analyses and DFT calculations thus identify and quantify the small fraction of ^{19}F species at the surfaces of the $\text{F}:\text{In}_2\text{O}_3$ NCs that are hypothesized to direct the NC morphology by adsorbing on (100) facet surface sites.

Fluorine as an Anionic Dopant. The discussion regarding fluorine has so far been limited to the NC surface: F^- selectively passivates NC surfaces to influence shape. The possible impact on the crystal lattice when F^- is incorporated into the In_2O_3 NCs is investigated by analyzing XRD as a function of fluorine incorporation. Fluorine being more electronegative than oxygen and the crystal ionic radius⁶² of F^- (1.19 Å) being only slightly smaller than that of the O^{2-} site (1.28 Å) in bixbyite phase In_2O_3 would allow it to easily occupy oxygen sites.^{19,63} XRD patterns (Figure S12) of $\text{F}:\text{In}_2\text{O}_3$ NCs (1–12% InF_3) confirm that the cubic bixbyite In_2O_3 crystal structure is maintained⁶⁴ and reveal that the F^- doping induces lattice strain. Lattice contraction relative to undoped In_2O_3 NCs is observed on the basis of the shift in the position of the (400) diffraction reflection at a low doping level (1% InF_3), which is ascribed to the smaller ionic radius of F^- as a substitutional dopant occupying O lattice sites not only at the surface but also internal to the NCs (Figure S12). Lattice contraction is also observed at low dopant concentrations in $\text{Sn}:\text{In}_2\text{O}_3$ ⁶⁵ and $\text{F}:\text{SnO}_2$,⁶³ where it has been similarly ascribed to aliovalent dopants with smaller ionic radii substituting the larger ions in host lattices. Rietveld refinement³³ of the full XRD pattern was conducted to quantify this initial lattice contraction and revealed the subsequent displacements of the (400) and (222) reflections at higher concentrations of F^- doping that correspond to lattice expansion (Figure S12). Size-induced lattice expansion or contraction, although reported in sub 10 nm metal oxide NCs, can be excluded due to the large size (100 nm or larger) of the In_2O_3 NCs considered here.⁶⁶ Undoped In_2O_3 NCs have a lattice constant of $a = 10.126$ Å,

close to the reported bulk In_2O_3 value of $a = 10.119$ Å.⁶⁷ In low-doped 1% InF_3 concentration NCs, a contracted lattice constant of $a = 10.083$ Å was measured. However, lattice expansion occurs at higher dopant concentrations, similar to the structural changes reported in heavily doped $\text{F}:\text{SnO}_2$ and $\text{Sn}:\text{In}_2\text{O}_3$ films.^{65,68} The (400) reflection shifts with F^- incorporation to $a = 10.190$ Å in 12% InF_3 doped NCs, resulting in a maximum observed lattice expansion of 0.58% that is attributed to dopant-screening effects from electrostatic repulsions.⁶⁵ Residual InF_3 is evident by XRD in the $\text{F}:\text{In}_2\text{O}_3$ NCs prepared with 3–12% InF_3 and can likely be attributed to emergent indium fluoride (InF_3) or indium oxyfluoride (InOF) residuals⁶⁹ (Figure S12).

To further understand the fluorine incorporation in the synthesized NC lattice, TGA was performed, as fluorine is known to diffuse out of NCs during high-temperature annealing under inert conditions.⁷⁰ TGA analysis shows initial weight loss starting at 400 °C that is ascribed to the removal of organic ligands. Upon further heating to 1100 °C, $\text{F}:\text{In}_2\text{O}_3$ cubes exhibit 1.3% weight reduction by fluorine liberation (Figure 5), corresponding to $\text{F}/\text{In} = 9.6\%$ atomic composition

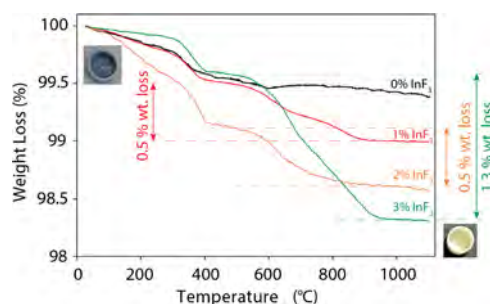
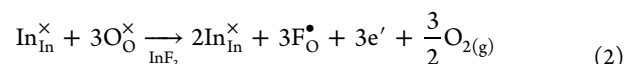
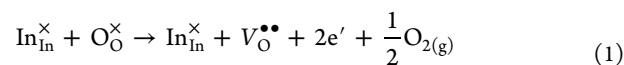


Figure 5. TGA curves for undoped In_2O_3 NCs (black curve), concave $\text{F}:\text{In}_2\text{O}_3$ cubes (red curve), sharp concave $\text{F}:\text{In}_2\text{O}_3$ cubes (orange curve), and $\text{F}:\text{In}_2\text{O}_3$ cubes (green curve). Photographs of the $\text{F}:\text{In}_2\text{O}_3$ cube sample (in an alumina crucible) before (left inset) and after TGA (right inset).

ratio. This TGA-based quantification agrees well with $\text{F}/\text{In} = 10.3\%$ quantified by TOF-SIMS. Concave $\text{F}:\text{In}_2\text{O}_3$ cubes show a 0.5% mass reduction corresponding to $\text{F}/\text{In} = 3.7\%$, whereas undoped In_2O_3 NCs show little or no weight loss that could be associated with fluorine when heated to high temperatures. SEM images reveal the $\text{F}:\text{In}_2\text{O}_3$ cube NCs sinter into irregularly shaped massive particles during high-temperature annealing (Figure S13).

Substitutional fluorine dopants incorporated in the NCs can be charge-compensated by free electrons. Fluorine is well-established as an anionic n-type dopant that induces high free-electron concentrations in fluorine-doped tin oxide ($\text{F}:\text{SnO}_2$) transparent conductive oxide films.^{22,63} The Kröger–Vink equation⁷¹ for oxygen vacancy formation demonstrates that such defects in the In_2O_3 lattice can be charge compensated by two electrons (eq 1).⁷² Oxygen substitution by F induces one free electron per fluorine ion (eq 2).^{73,74}



The band structure derived from DFT calculations predicts an elevated Fermi level when fluorine substitutes oxygen in In_2O_3 ,

as compared to undoped In_2O_3 . The Fermi level is calculated to be 1.1 eV above the conduction band minimum (Figure S14) with F dopants present in the In_2O_3 lattice unit cell (F/O = 1:47), due to free-electron carriers contributed to the conduction band, which leads to LSPR optical properties in F: In_2O_3 NC cubes. Electron paramagnetic resonance (EPR) spectroscopy provides evidence for free electrons in F: In_2O_3 NCs. The induced extra electrons are delocalized in the conduction band,^{75,76} leading to an observed EPR signal at $g \approx 2.20$ in doped F: In_2O_3 cubes. By comparison, undoped In_2O_3 NCs exhibit a weak EPR signal at $g \approx 2.00$ due to a low population of oxygen vacancy-induced free electrons or shallow donors (Figure S15).^{77,78} EPR spectra of the F: In_2O_3 cubes at cryogenic temperatures (100 K) showed increased signal intensity, which decreased at room temperature due to rapid free-electron relaxation.⁷⁹

The Kröger–Vink notation suggests that halogen dopants with the same valency as F^- should contribute to free-electron compensation. However, the large ionic radii of chloride (Cl^-) or bromide (Br^-) suggests that they are not suitable dopants to incorporate in In_2O_3 NCs. Doping of Cl or Br atoms into In_2O_3 NCs was attempted to check the viability of other halogen dopants. EDX quantification showed very low halide incorporation for these NCs, as compared with F: In_2O_3 NCs synthesized at the same dopant precursor concentration (3% InX_3 , X = F, Cl, Br) (Table 1). Cl: In_2O_3 NCs show only Cl/In = $0.32 \pm 0.11\%$ atomic composition ratio, and Br: In_2O_3 NCs had Br/In = $2.62 \pm 0.06\%$, whereas F: In_2O_3 cubes show higher F/In = $11.76 \pm 2.70\%$. The low anionic dopant concentration observed can be attributed to Cl^- (1.81 Å) having a much larger ionic radius than F^- (1.19 Å), which would yield a correspondingly large ionic radius mismatch (41.4%) with O^{2-} (1.28 Å) and cause significant lattice strain in the host lattice.⁶² Similarly, Br^- (1.96 Å) is not incorporated within the In_2O_3 NC lattice, consistent with similar straining (53.1%).⁶²

On the basis of quantitative 1D ^{19}F MAS NMR and ^{19}F spin-lattice relaxation time analyses, the majority of ^{19}F atoms in the F: In_2O_3 NCs are located in metallic subsurface environments. The 1D ^{19}F MAS NMR spectrum in Figure 4a shows two broad ^{19}F signals at 50 and -50 ppm with FWHM signal linewidths of 66 and 26 ppm, respectively. The ^{19}F signal at -50 ppm is similar to ^{19}F signals observed for some other metal oxyfluorides^{80–82} and is assigned to isolated F^- anionic dopant species in the F: In_2O_3 NCs. By comparison, on the basis of temperature-dependent analyses of ^{19}F spin-lattice (T_1) relaxation times, the ^{19}F signal at 50 ppm is confidently assigned to a distribution of ^{19}F species in metallic environments in the F: In_2O_3 NCs. In metallic materials, including degenerately doped semiconductors,⁸³ nuclear spins and conduction band electrons in s-like orbitals couple through Fermi contact interactions. These interactions give rise to two characteristic effects that are manifested in the ^{19}F NMR spectra of F: In_2O_3 NCs: a frequency displacement of the ^{19}F NMR signals called the Knight shift^{83–85} and a Korringa-type temperature dependence of the rate of ^{19}F nuclear spin-lattice relaxation.^{84,86,87} For the ideal case of isolated nuclear spins coupled to a degenerate gas of electron spins, the Korringa contribution to the relaxation rate, $T_{1,K}^{-1}$, is related to the Knight shift, K , by the well-known Knight–Korringa relation^{84,86}

$$T_{1,K}^{-1}(K, T) = \left(\frac{\gamma_n}{\gamma_e} \right)^2 \frac{4\pi k_B T}{\hbar} K^2 \quad (3)$$

where γ_n and γ_e are the gyromagnetic ratios of the nuclear and electron spins, respectively, k_B and \hbar are the Boltzmann and Planck constants, and T is the absolute temperature. The Knight–Korringa relation shows that the $T_{1,K}^{-1}$ values for nuclear spins in metallic environments are proportional to both temperature, T , and the square of the Knight shift, K^2 . Fluorine species in metallic environments may therefore be identified on the basis of analysis of the ^{19}F T_1^{-1} values as functions of both NMR frequency position and temperature.

Analyses of the 1D ^{19}F MAS NMR spectra and T_1^{-1} relaxation rates at temperatures of 276–395 K, shown in Figure 6, reveal that the broad ^{19}F signal at 50 ppm in Figure 4a corresponds to ^{19}F dopant atoms in metallic environments within the F: In_2O_3 NCs that exhibit Korringa-type relaxation behavior. By comparison, the ^{19}F signal at -50 ppm, which also manifests a broad distribution of ^{19}F environments, exhibits no Korringa-type temperature dependencies in its spin-lattice relaxation behavior, consistent with its assignment to a distribution of isolated ^{19}F dopants in the In_2O_3 lattice that experience chemical and/or paramagnetic shifts but not metallic Knight shifts. The ^{19}F frequency axis in Figure 4a is renormalized in Figure 6a such that the signal from isolated F^- dopant species (-50 ppm in Figure 4a) is set to a Knight shift K of 0 ppm. As shown in Figure 6a, the broad ^{19}F signal distribution at $K = 100$ ppm (50 ppm in Figure 4a) from ^{19}F species in metallic environments does not change significantly in width or position over the temperature range 276–395 K, consistent with the expected temperature invariance of Knight shifts for heavily doped semiconductors with the Fermi level above the conduction band minimum (Figure S14).⁸⁴ The ^{19}F T_1^{-1} values were measured by ^{19}F saturation recovery experiments, and the $T_{1,K}$ values for each isochromat across the ^{19}F Knight-shifted signal distribution were extracted by subtraction of the temperature-independent contribution ($T_{1,0}^{-1}$) from the overall relaxation rate, T_1^{-1}

$$T_{1,K}^{-1}(K, T) = T_1^{-1}(K, T) - T_{1,0}^{-1} \quad (4)$$

The temperature- and shift-independent term $T_{1,0}^{-1}$ depends on the MAS rate and was measured to be $6.9 \pm 0.3 \text{ s}^{-1}$ at 25 kHz MAS and $4.8 \pm 0.5 \text{ s}^{-1}$ at 35 kHz MAS. Due to the MAS dependence of $T_{1,0}^{-1}$, this term likely reflects the contribution to the ^{19}F T_1^{-1} relaxation rate of strong ^{19}F – ^{19}F and/or ^{19}F –electron dipole–dipole couplings, which are partially averaged under MAS conditions. Additional details on the ^{19}F T_1 relaxation analyses and the extraction of the $T_{1,0}^{-1}$ and $T_{1,K}^{-1}$ terms are provided in the Supporting Information (Figure S16). The square root of the temperature-dependent relaxation term, $T_{1,K}^{-1/2}$, is plotted as a function of K for the $K = 50$ –175 ppm region (the boxed region in Figure 4a) in Figure 6b. At temperatures of 395 K (red) and 276 K (blue), the measured $T_{1,K}^{-1/2}$ values show excellent agreement across the entire ^{19}F Knight shift distribution with the theoretical values predicted by the Knight–Korringa expression at the different temperatures (dotted lines), which notably has no adjustable parameters and is derived from first principles.^{83,84,86} Additionally, the Knight–Korringa relation holds across the entire temperature range of 276–395 K. The Korringa-type plot in Figure 6c shows a plot of the $T_{1,K}^{-1}$ values extracted at the maxima of the ^{19}F Knight shift distribution ($K = 100$ ppm), as

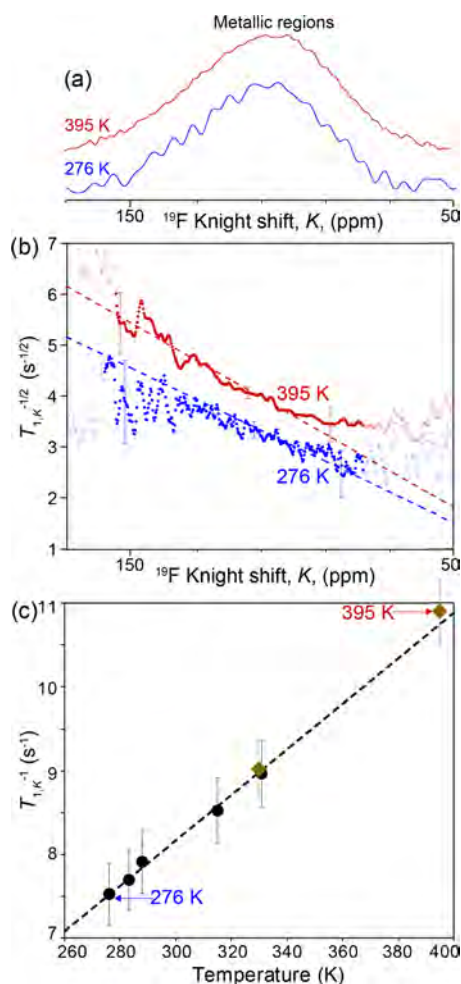


Figure 6. (a) Enlargement of the Knight-shifted ^{19}F spectral region (the boxed region in Figure 4a) showing a comparison of the 1D solid-state ^{19}F echo MAS NMR spectra of F: In_2O_3 NCs (3% InF_3) diluted in a 1:1 ratio by mass with KBr. The frequency axis is renormalized with the zero Knight shift peak at -50 ppm, corresponding to the signal from isolated F^- dopants in the F: In_2O_3 NCs. The spectra were acquired at 9.4 T at 35 kHz MAS and 395 K (red) and 25 kHz MAS and 276 K (blue). (b) Plot of the square root of the ^{19}F spin-lattice relaxation rate due to Korringa relaxation, $T_{1,K}^{-1/2}$, for different ^{19}F Knight shifts K in F: In_2O_3 NCs (3% InF_3), measured at 9.4 T at 35 or 25 kHz MAS and at 395 K (red) or 276 K (blue). Partially transparent data points correspond to spectral regions with little or no ^{19}F signal intensity, resulting in large uncertainties that are not pertinent to the analyses. (c) Plot of the ^{19}F $T_{1,K}^{-1}$ at the peak maximum of the Knight shift distribution ($K = 100$ ppm) as a function of temperature. Black circles and brown diamonds indicate $T_{1,K}^{-1}$ values measured under MAS conditions of 25 and 35 kHz, respectively. The dashed lines in (b) and (c) indicate theoretical values obtained from the Knight–Korringa equation (eq 3).

a function of temperature, revealing excellent agreement with the Knight–Korringa relation over the entire temperature range. This corroborates the conclusion that the broad ^{19}F signal at 50 ppm in Figure 4a arises from a distribution of Knight shifts that manifest a range of couplings of ^{19}F nuclei to conduction band electrons in regions of the F: In_2O_3 NCs with different extents of metallic character. The ^{19}F atoms, acting as anionic n-type dopants, therefore are sufficiently dense so that their associated unpaired electrons form a conductive network within the heavily doped In_2O_3 lattice.

Furthermore, on the basis of the quantitative single-pulse ^{19}F NMR spectrum of the F: In_2O_3 NCs (3% InF_3) (Figure S11), approximately $82 \pm 1\%$ of all of the ^{19}F species are in subsurface metallic environments in the In_2O_3 lattice, $17 \pm 1\%$ in residual InF_3 , which is assigned on the basis of the XRD pattern and long ^{19}F relaxation time (23 s), and $<1\%$ at isolated dopant sites in the In_2O_3 lattice. The combined solid-state 2D $^1\text{H}\{^{19}\text{F}\}$ NMR correlation and ^{19}F T_1 relaxation analyses establish that only a small percentage (1–2%) of ^{19}F species are at the surfaces of the F: In_2O_3 NCs. The majority of ^{19}F species are incorporated into the F: In_2O_3 NCs in subsurface metallic domains, consistent with F^- as an anionic dopant within the In_2O_3 lattice.

The metallic domains are also manifested by evidence of conduction band electron influences on local ^{115}In environments in the F: In_2O_3 crystal lattice. Specifically, analyses and comparison of the solid-state wide-line ^{115}In NMR spectra in Figure 7 of undoped bulk In_2O_3 and F: In_2O_3 NCs show

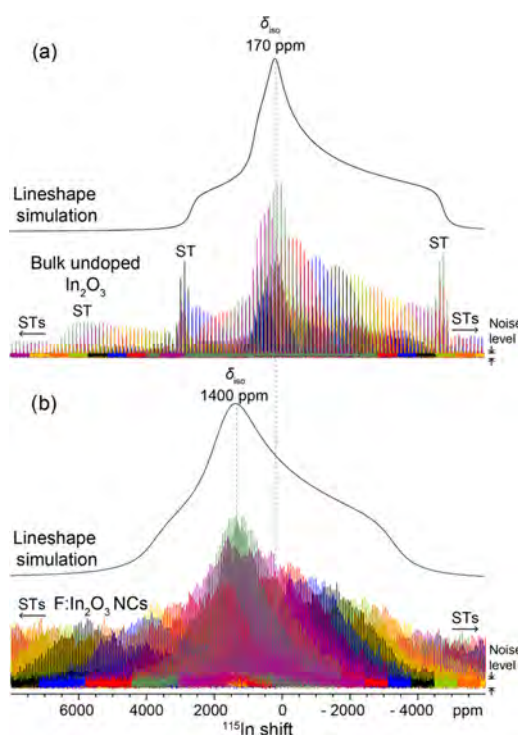


Figure 7. Solid-state 1D ^{115}In NMR spectra of (a) undoped microcrystalline In_2O_3 and (b) F: In_2O_3 NCs (3% InF) acquired at 295 K, under static conditions, and at magnetic field strengths of (a) 18.8 T and (b) 19.6 T. The spectra are an overlay of 22 different subspectra (shown as different colors) acquired at evenly spaced frequency intervals. Simulated ^{115}In NMR line shapes generated using the parameters in Table S1 are shown offset above the experimental ^{115}In NMR spectra. Signal intensities arising from ^{115}In satellite transitions are indicated by “ST.”

differences that are characteristic of the coupling of ^{115}In nuclei to free electrons. Acquisition of solid-state ^{115}In NMR spectra has been exceedingly challenging in the past due to the highly quadrupolar character of ^{115}In nuclei ($I = 9/2$), which often exhibit very broad (several MHz) and poorly resolved ^{115}In NMR signals.⁸⁸ Very few solid-state ^{115}In NMR spectra of inorganic materials have been reported, with emphases primarily on materials with ^{115}In atoms in symmetric environments, such as cubic zinc blende semiconductors, like

InP and InN,^{89,90} which yield narrower and more tractable line shapes. Nevertheless, recent wide line NMR techniques enable the detection and analysis of very broad NMR signals, even for quadrupolar nuclei in paramagnetic or conductive materials.^{91–93}

Here, the frequency-stepped quadrupolar Carr–Purcell–Meiboom–Gill (QCPMG) technique⁴¹ was used to measure the solid-state ¹¹⁵In NMR spectra of bulk undoped polycrystalline In₂O₃ and F:In₂O₃ NCs (Figure 7). The QCPMG pulse sequence yields manifolds of very narrow, evenly spaced NMR signals (spikelets) that cannot cover the entire ¹¹⁵In spectral range of these materials but can be systematically acquired as a series that can be overlain to map the full ~2 MHz broad central transition (CT) region of the ¹¹⁵In NMR spectrum. For example, the ¹¹⁵In NMR spectrum in Figure 7a of bulk undoped In₂O₃ is presented as a mosaic overlay of 22 individual QCPMG subspectra (plotted in different colors) that were acquired at evenly spaced frequency intervals. Although a detailed analysis of the ¹¹⁵In NMR line shapes is complicated by overlap of the numerous ¹¹⁵In satellite transitions (STs) of the quadrupolar ¹¹⁵In nuclei, the sensitivity and resolution of the wideline ¹¹⁵In QCPMG spectra are sufficient to simulate the ¹¹⁵In CT regions and estimate the quadrupolar coupling constant (C_Q), asymmetry parameter (η), and isotropic shift (δ_{iso}) for the bulk In₂O₃ (Table S1). Such NMR parameters are highly sensitive to the chemical and electronic environments of ¹¹⁵In species in In₂O₃ and to our knowledge have never previously been measured or reported.

Compared with bulk In₂O₃, the ¹¹⁵In NMR spectrum of F:In₂O₃ NCs is displaced and broadened, consistent with the coupling of ¹¹⁵In nuclei to unpaired conduction band electrons. Both undoped polycrystalline In₂O₃ (Figure 7a) and F-doped In₂O₃ NCs (Figure 7b) exhibit very broad spectral features in the –4000 to 4000 ppm range that arise from the CT of ¹¹⁵In nuclei in the different materials. The ¹¹⁵In CT regions for both materials are reproduced by a single simulated ¹¹⁵In lineshape with $C_Q \approx 130$ MHz and $\eta = 1$, although with different isotropic shifts (Figure 7, black spectra, see also Table S1). The bulk undoped In₂O₃ (cubic bixbyite phase by XRD, Figure S17) exhibits an isotropic ¹¹⁵In shift of 170 ppm, consistent with diamagnetic ¹¹⁵In environments in the In₂O₃ lattice. By comparison, the ¹¹⁵In spectrum of F:In₂O₃ NCs (3% InF) exhibits an isotropic ¹¹⁵In shift of 1400 ppm, displaced more than 1200 ppm from the position for diamagnetic In₂O₃. This displacement provides evidence that the majority of ¹¹⁵In species in the F:In₂O₃ lattice experience substantial Knight shifts⁸³ arising from interactions with unpaired conduction band electrons associated with the F dopant species. The ¹¹⁵In Knight shifts corroborate the ¹⁹F NMR and T_1 spin-lattice relaxation time analyses discussed above. The ¹¹⁵In NMR spectrum of the F:In₂O₃ NCs is also broadened compared to that of bulk undoped In₂O₃, indicating a larger distribution of chemical shifts, Knight shifts, and/or quadrupolar parameters (Table S1). The continuous distributions of signal intensity extending to higher and lower frequencies in both of the ¹¹⁵In NMR spectra in Figure 7 arise from the very broad and overlapping ¹¹⁵In satellite transitions, which are expected to span frequency regions of tens of MHz. To the best of our knowledge, the solid-state ¹¹⁵In NMR spectra presented here are the first ¹¹⁵In NMR analyses of In₂O₃, and evidence the sensitivity of ¹¹⁵In NMR to different electronic environments in technologically important In₂O₃ materials.

In summary, the solid-state ¹⁹F and ¹¹⁵In NMR analyses together provide complementary and consistent evidence for metallic ¹⁹F and ¹¹⁵In environments in the heavily doped F:In₂O₃ lattice. Free electrons at the conduction band and spatially internal to F:In₂O₃ NCs interact with the nuclear spins of extrinsic dopant (F) and NC lattice (In) atoms. This gives rise to characteristic effects manifested in the NMR spectra of the degenerately doped semiconductors including ¹⁹F and ¹¹⁵In Knight shifts and Korringa-type temperature dependencies of the ¹⁹F nuclear spin-lattice relaxation times.

Optical Properties. Considerations of charge compensation accompanying fluorine doping (eq 2) as well as the NMR analyses of the ¹⁹F and ¹¹⁵In species show that the anionically doped F:In₂O₃ NCs contain substantial free-electron populations leading to LSPR response. By eye, doped F:In₂O₃ NCs in solvent dispersions appear blue, in contrast to clear or white undoped In₂O₃ NCs (Figure S18). Liquid-cell FTIR spectra confirm that the F:In₂O₃ NCs exhibit IR range LSPR, with an absorption tail toward the visible region that is responsible for their blue appearance. The role of fluorine as an anionic dopant is apparent even in rounded F:In₂O₃ NCs (1% InF₃) synthesized at 280 °C. These NCs have a mean diameter of 338.0 ± 51.0 nm with 4.4 ± 0.4 atom % F by EDX, and exhibit an LSPR extinction peak at 3497 cm^{-1} (Figure 8). For

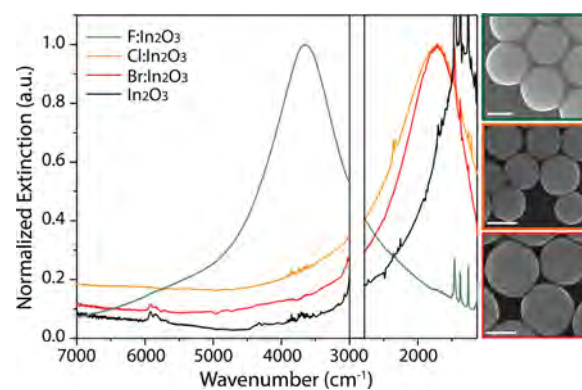


Figure 8. Liquid-cell FTIR spectra for spherical F:In₂O₃ (green line), Cl:In₂O₃ (orange line), Br:In₂O₃ (red line), and In₂O₃ NCs (black line). Spectral bands saturated by ligand absorption are shown as blank regions. (Inset) SEM images showing F:In₂O₃ (green), Cl:In₂O₃ (orange), and Br:In₂O₃ (red) NCs. Scale bars are 200 nm.

comparison, undoped pseudospherical In₂O₃ NCs show a low-energy LSPR peak located at 1370 cm^{-1} , consistent with a low concentration of free electrons induced by the presence of oxygen vacancies (eq 1)⁹⁴ (Figure 8). In both Cl:In₂O₃ and Br:In₂O₃ NCs, however, the LSPR peak is at 1743 cm^{-1} , indicating low free-electron concentration compared to that of F:In₂O₃ NCs due to low dopant incorporation (Figure 8). These comparative observations demonstrate that fluorine is a uniquely effective anionic halide dopant for In₂O₃ NCs to induce LSPR in the IR region.

In the F:In₂O₃ cubes, the highly defined corners and edges are expected to result in multimodal LSPR extinction peaks in the IR spectral range. F:In₂O₃ cubes (3% InF₃) have highly pronounced plasmon peaks at 3496 cm^{-1} (FWHM 1157 cm^{-1}) and 5469 cm^{-1} (Figure 9a, green), respectively, ascribed to corner- and edge-dominated LSPR modes, by comparison to analogous modes observed for silver cubes.⁹⁵ Through the Drude model, the free-carrier density within the F:In₂O₃ cube

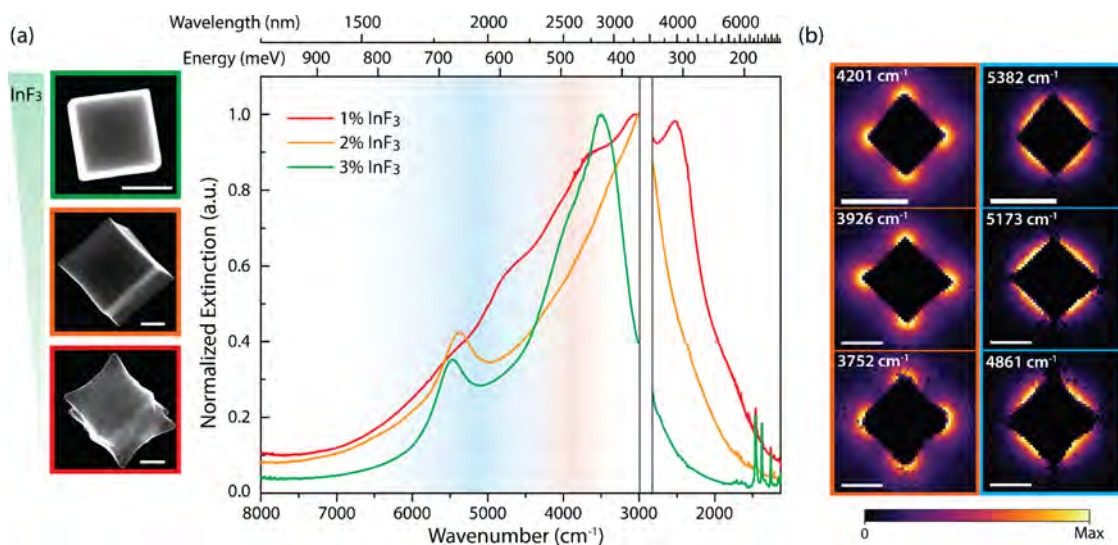


Figure 9. (a) Liquid cell FTIR spectra of F:In₂O₃ NCs with corresponding SEM images. F:In₂O₃ cube (green), F:In₂O₃ sharp concave cube (orange), and F:In₂O₃ concave cube (red). Scale bars are 100 nm. Spectral bands saturated by ligand absorption are shown as blank regions. Sharp peaks observed at 1000 cm⁻¹ region are assigned to surface-bound organic ligands. (b) F:In₂O₃ (3% InF₃) cube (top), F:In₂O₃ (2% InF₃) sharp concave cube (middle), and F:In₂O₃ (1% InF₃) concave cube (bottom) EELS maps for corner mode frequencies (around 3900 cm⁻¹, left, orange) and edge mode frequencies (around 5100 cm⁻¹, right, blue) LSPR mode. Scale bars are 200 nm.

(3% InF₃) is estimated to be $6.8 \times 10^{20} \text{ cm}^{-3}$ on the basis of the LSPR extinction spectrum (Figure S19). Estimated from the NMR results, the concentration of F atoms in metallic environments in the F:In₂O₃ cubes is $2.5 \times 10^{21} \text{ cm}^{-3}$, considering 80% of the F as being in a subsurface metallic environments and that the F/In atom ratio is 0.10. Combined, these estimates indicate that only a fraction of subsurface F atoms (27%) is activated and contributes electron carriers to the conduction band whereas the remainder of the internal F dopants are otherwise compensated.

Lower fluorine-doped F:In₂O₃ concave cube NCs exhibit changes in LSPR peak shape due to NC shape effects. Sharp concave cubes (2% InF₃) show well-defined modes with LSPR peaks at 2974 and 5378 cm⁻¹ (Figure 9a, orange). Concave cubes (1% InF₃) with elongated <111> directional corners exhibit a complex LSPR response centered at 3030 cm⁻¹ (Figure 9, red). Previous literature on plasmonic octopod Ag NCs has described the breakdown of simple cubic LSPR modes due to elongated corners.^{96,97} By contrast, no multimode LSPR peaks are observed for rounded F:In₂O₃ NCs (1% InF₃) grown at 280 °C due to their mostly spherical shape (Figure 8, green).¹⁰ During the growth of F:In₂O₃ NC cubes (3% InF₃), FTIR of aliquots demonstrate retention of both edge- and corner-mode LSPR peaks (Figure S20). The edge-mode LSPR at a higher wave number range is observed at 5690 cm⁻¹ and retained during 1–4 min of reaction time. The corner-mode LSPR peak is also retained at 3340 cm⁻¹ until the end of the growth reaction (2–4 min). It is observed that the F:In₂O₃ cube aliquot dopant composition is steady at F/In = $11.8 \pm 0.4\%$ throughout the growth reaction. This suggests that incorporation of subsurface fluorine species, as detected by ¹⁹F NMR, is sustained during NC growth.

To definitively assign the contributions to the multimodal FTIR peaks observed in faceted F:In₂O₃ NCs, we perform STEM-EELS mapping of individual cubes. Optical LSPR excitation in the FTIR only allows ensemble far-field extinction measurements of cubes, where the incidence IR excitation wavelength (1250–10 000 nm) is within the LSPR quasistatic

limit range.¹⁰ The sub Angstrom diameter probe available in the STEM can directly sample and map the near-field localization of LSPR modes, and thanks to recent advances in monochromation, these mid-infrared frequencies are now accessible using EELS.^{98,99} The spatial maps are acquired through spectrum imaging (SI), where the beam is rastered across the region of interest and a spectrum is acquired at each probe position, resulting in a three-dimensional dataset with two spatial dimensions and one spectral dimension. From here, individual plasmon modes are deconvoluted through the non-negative matrix factorization (NMF) method to produce spatially resolved EELS maps of individual LSPR modes.⁹⁵ For each structure, spatially and spectrally distinct corner and side modes can be observed and mapped through the deconvoluted spectrum imaging, which are plotted in Figure 9b. The corner modes of F:In₂O₃ cube (3% InF₃), sharp concave cube (2% InF₃), and concave cube (1% InF₃) NCs are observed at 4201, 3926, and 3752 cm⁻¹, respectively, with the side mode resonances centered at 5382, 5173, and 4861 cm⁻¹. It is important to note that for the side modes, the NMF-deconvolution results in a spectral component with multiple peaks, likely corresponding to spatially overlapped edge and face modes. The reported peak center is the average of these face and edge modes. Details of the deconvolution and the EELS experiments are presented in greater detail in Text S3, Supporting Information.

Although FTIR samples the ensemble behavior and EELS samples individual structures, the match is strong enough to determine the modal nature of the FTIR peaks from the EEL-SI. The STEM analysis supports that the high-energy FTIR peaks correspond to the edge and face modes, whereas the lower energy peaks correspond to the corner modes. As in FTIR, in EELS the edge mode is observed at higher energy for the cube (3% InF₃) than for the sharp concave cube (2% InF₃). The frequencies of the corner modes do differ significantly between FTIR and EELS, which can be understood as originating from differences in the dielectric function in the liquid-cell FTIR experiments and the SiN/ultra-high-vacuum

environment in the STEM.¹⁰⁰ The observed blue shift in the EELS mode relative to the FTIR spectrum is attributed to the lower refractive index ($n = 1$) of the surrounding vacuum in STEM, as compared with the TCE solution medium ($n = 1.5$) in the liquid-cell optical measurement.^{101,102}

CONCLUSIONS

Fluorine plays a dual role as a dopant, influencing preferential growth of certain crystal facets and directing morphology of colloidally synthesized In_2O_3 NCs, as well as inducing IR range LSPR by aliovalent doping within the In_2O_3 NC lattice. In this study, we have demonstrated that introducing fluorine precursors in a typical heat-up method colloidal synthesis yields highly faceted $\text{F}:\text{In}_2\text{O}_3$ cube NCs with a shape-dependent LSPR response. Morphological control is demonstrated for the formation of concave cubes by adjusting the dopant concentration during $\text{F}:\text{In}_2\text{O}_3$ NC synthesis. Small percentages (1–2 atom %) of fluorine species are shown to be at the surfaces of the $\text{F}:\text{In}_2\text{O}_3$ NCs and hinder growth of $\{100\}$ facets, as determined by combined XPS, solid-state 2D $^1\text{H}\{-^{19}\text{F}\}$ NMR and DFT analyses. By comparison, the majority of fluorine species are incorporated into subsurface metallic environments in the $\text{F}:\text{In}_2\text{O}_3$ lattice, consistent with F^- acting as an anionic dopant, as revealed by variable-temperature analyses of ^{19}F spin-lattice relaxation times and comparison to the Knight–Korringa relation. Complementary analyses of wide-line ^{115}In NMR spectra show that the majority of ^{115}In species in the $\text{F}:\text{In}_2\text{O}_3$ species interact with unpaired conduction band electrons, providing corroboratory evidence that the $\text{F}:\text{In}_2\text{O}_3$ NC lattice is heavily doped beyond the metal-insulator transition. Arising from the combined effects of dopant-induced free carriers and highly faceted NC shapes, multimodal LSPR extinction features are observed in the IR. Single-NC LSPR near-field modes spatially localized around sharp morphological features are directly observed by STEM-EELS.

With this understanding of the role played by fluorine both on the NC surface and in the lattice, $\text{F}:\text{In}_2\text{O}_3$ NCs provide a valuable platform material for exploring properties and applications of LSPR-active NCs. Analogous to Ag nanocubes that exhibit visible LSPR,⁹⁵ well-defined In_2O_3 nanocubes are able to be colloidally synthesized, with shape-dependent LSPR in the IR spectral range. Near-field localization of IR light will make these highly faceted $\text{F}:\text{In}_2\text{O}_3$ NCs a platform material to evaluate near-field enhancement effects and explore applications unique to the infrared, including coupling LSPR to molecular vibrational modes²⁰ and IR emissive excitons.¹⁰³ To meet these demands, control of NC sizes and LSPR spectral tunability need be advanced. Large cube NC sizes lead to greater magnitude in near-field enhancement,²⁰ and full NC size control ranging from small to large cubes may allow a range of near-field intensities to be achieved. Further synthetic advances, such as the systematic incorporation of co-dopants,¹⁹ may lead to additional LSPR tuning by increasing free-electron compensation in In_2O_3 NCs. However, synthetic questions remain as to fully understanding cationic co-dopant incorporation in metal oxides in the presence of anionic dopants.^{20,104} The understanding of the dual role of fluorine as an anionic dopant in $\text{F}:\text{In}_2\text{O}_3$ NCs is expected to provide a foundation for addressing these questions and challenges and further improving the properties of these versatile materials.

ASSOCIATED CONTENT

Supporting Information

The Supporting Information is available free of charge on the ACS Publications website at DOI: 10.1021/acs.chemmater.9b00906.

Details of nanocrystal characterization (SEM, EDX, TOF-SIMS, XPS, EPR, TGA, and XRD), nanocrystal aliquots (time and temperature series SEM, FTIR), solid-state NMR details (quantitative ^{19}F NMR, Knight–Korringa relation, ^{115}In simulated line shape parameters), DFT simulation (supercell, DFT calculation), and details of monochromated EELS (background subtraction, non-negative matrix factorization, and modal deconvolution) (PDF)

AUTHOR INFORMATION

Corresponding Authors

*E-mail: bradc@engineering.ucsb.edu (B.F.C.).

*E-mail: milliron@che.utexas.edu (D.J.M.).

ORCID

Shin Hum Cho: 0000-0002-0271-116X

Sandeep Ghosh: 0000-0002-1149-9199

Zachariah J. Berkson: 0000-0002-2157-4172

Jordan A. Hachtel: 0000-0002-9728-0920

Clayton J. Dahlman: 0000-0002-4555-4846

Yuan Yue Liu: 0000-0002-5880-8649

Bradley F. Chmelka: 0000-0002-4450-6949

Delia J. Milliron: 0000-0002-8737-451X

Author Contributions

*S.H.C., S.G., and Z.J.B. contributed equally to this work.

Notes

The authors declare no competing financial interest.

ACKNOWLEDGMENTS

S.H.C., S.G., L.C.R., C.J.D., and D.J.M. acknowledge the support from the National Science Foundation (NSF, CHE-1609656, CBET-1704634, NASCENT, an NSF ERC—EEC-1160494, and CDCM, an NSF MRSEC—DMR-1720595), the Welch Foundation (F-1848), and Fulbright Program (IIE-15151071). We thank A. Dolocan, K. Jarvis, and H. Celio in the Texas Materials Institute (TMI) for user facility assistance. Y.L. and X.Z. acknowledge support from the Welch Foundation (Grant No. F-1959-20180324). Y.L. thanks the startup support from UT Austin. This work used computational resources sponsored by the Department of Energy (DOE), Office of Energy Efficiency and Renewable Energy located at the National Renewable Energy Laboratory (NREL) and the Texas Advanced Computing Center (TACC) at UT Austin. Z.J.B. was supported by a grant from the BASF Corporation. The solid-state NMR measurements made use of the MRL Shared Experimental Facilities of the University of California, Santa Barbara, which are supported by the MRSEC Program of the NSF under Award No. DMR 1720256; a member of the NSF-funded Materials Research Facilities Network (www.mrfn.org). We thank Drs. Z. Gan, I. Hung, and X. Wang for assistance with the solid-state ^{115}In NMR measurements of the $\text{F}:\text{In}_2\text{O}_3$ NCs conducted at the National High Magnetic Field Laboratory, which is supported by the National Science Foundation Cooperative Agreement No. DMR-1644779 and the State of Florida. Some microscopy

research was performed as part of a user proposal at Oak Ridge National Laboratory's (ORNL) the Center for Nanophase Materials Sciences (CNMS), which is a U.S. Department of Energy, Office of Science User Facility (J.A.H., J.-C.I.). This research was conducted, in part, using instrumentation within ORNL's Materials Characterization Core provided by UT-Battelle, LLC, under contract No. DE-AC05-00OR22725 with the DOE. L.C.R. acknowledges the MMRRSA School at ORNL.

REFERENCES

- (1) Agrawal, A.; Cho, S. H.; Zandi, O.; Ghosh, S.; Johns, R. W.; Milliron, D. J. Localized Surface Plasmon Resonance in Semiconductor Nanocrystals. *Chem. Rev.* **2018**, *118*, 3121–3207.
- (2) Sasaki, T.; Endo, Y.; Nakaya, M.; Kanie, K.; Nagatomi, A.; Tanoue, K.; Nakamura, R.; Muramatsu, A. One-Step Solvothermal Synthesis of Cubic-Shaped ITO Nanoparticles Precisely Controlled in Size and Shape and Their Electrical Resistivity. *J. Mater. Chem.* **2010**, *20*, 8153–8157.
- (3) Xia, Y.; Xia, X.; Peng, H.-C. Shape-Controlled Synthesis of Colloidal Metal Nanocrystals: Thermodynamic versus Kinetic Products. *J. Am. Chem. Soc.* **2015**, *137*, 7947–7966.
- (4) Seo, D.; Park, J. C.; Song, H. Polyhedral Gold Nanocrystals with O_h Symmetry: From Octahedra to Cubes. *J. Am. Chem. Soc.* **2006**, *128*, 14863–14870.
- (5) Zhou, S.; Li, J.; Gilroy, K. D.; Tao, J.; Zhu, C.; Yang, X.; Sun, X.; Xia, Y. Facile Synthesis of Silver Nanocubes with Sharp Corners and Edges in an Aqueous Solution. *ACS Nano* **2016**, *10*, 9861–9870.
- (6) DeSantis, C. J.; Skrabalak, S. E. Size-Controlled Synthesis of Au/Pd Octopods with High Refractive Index Sensitivity. *Langmuir* **2012**, *28*, 9055–9062.
- (7) Alvarez, M. M.; Khoury, J. T.; Schaaff, T. G.; Shafiqullin, M. N.; Vezmar, I.; Whetten, R. L. Optical Absorption Spectra of Nanocrystal Gold Molecules. *J. Phys. Chem. B* **1997**, *101*, 3706–3712.
- (8) Naik, G. V.; Shalae, V. M.; Boltasseva, A. Alternative Plasmonic Materials: Beyond Gold and Silver. *Adv. Mater.* **2013**, *25*, 3264–3294.
- (9) Luther, J. M.; Jain, P. K.; Ewers, T.; Alivisatos, A. P. Localized Surface Plasmon Resonances Arising from Free Carriers in Doped Quantum Dots. *Nat. Mater.* **2011**, *10*, 361–366.
- (10) Agrawal, A.; Kriegel, I.; Milliron, D. J. Shape-Dependent Field Enhancement and Plasmon Resonance of Oxide Nanocrystals. *J. Phys. Chem. C* **2015**, *119*, 6227–6238.
- (11) Kanehara, M.; Koike, H.; Yoshinaga, T.; Teranishi, T. Indium Tin Oxide Nanoparticles with Compositionally Tunable Surface Plasmon Resonance Frequencies in the Near-IR Region. *J. Am. Chem. Soc.* **2009**, *131*, 17736–17737.
- (12) Buonsanti, R.; Llordes, A.; Aloni, S.; Helms, B. A.; Milliron, D. J. Tunable Infrared Absorption and Visible Transparency of Colloidal Aluminum-Doped Zinc Oxide Nanocrystals. *Nano Lett.* **2011**, *11*, 4706–4710.
- (13) Gordon, T. R.; Paik, T.; Klein, D. R.; Naik, G. V.; Caglayan, H.; Boltasseva, A.; Murray, C. B. Shape-Dependent Plasmonic Response and Directed Self-Assembly in a New Semiconductor Building Block, Indium-Doped Cadmium Oxide (ICO). *Nano Lett.* **2013**, *13*, 2857–2863.
- (14) Ghosh, S.; Manna, L. The Many “Facets” of Halide Ions in the Chemistry of Colloidal Inorganic Nanocrystals. *Chem. Rev.* **2018**, *118*, 7804–7864.
- (15) Xia, X.; Xie, S.; Liu, M.; Peng, H.-C.; Lu, N.; Wang, J.; Kim, M. J.; Xia, Y. On the Role of Surface Diffusion in Determining the Shape or Morphology of Noble-Metal Nanocrystals. *Proc. Natl. Acad. Sci. U.S.A.* **2013**, *110*, 6669–6673.
- (16) Liu, G.; Yang, H. G.; Pan, J.; Yang, Y. Q.; Lu, G. Q.; Cheng, H.-M. Titanium Dioxide Crystals with Tailored Facets. *Chem. Rev.* **2014**, *114*, 9559–9612.
- (17) Meyns, M.; Iacono, F.; Palencia, C.; Geweke, J.; Coderch, M. D.; Fittschen, U. E. A.; Gallego, J. M.; Otero, R.; Juárez, B. H.; Klinke, C. Shape Evolution of CdSe Nanoparticles Controlled by Halogen Compounds. *Chem. Mater.* **2014**, *26*, 1813–1821.
- (18) Ghosh, S.; Gaspari, R.; Bertoni, G.; Spadaro, M. C.; Prato, M.; Turner, S.; Cavalli, A.; Manna, L.; Brescia, R. Pyramid-Shaped Wurtzite CdSe Nanocrystals with Inverted Polarity. *ACS Nano* **2015**, *9*, 8537–8546.
- (19) Ye, X.; Fei, J.; Diroll, B. T.; Paik, T.; Murray, C. B. Expanding the Spectral Tunability of Plasmonic Resonances in Doped Metal-Oxide Nanocrystals through Cooperative Cation–Anion Codoping. *J. Am. Chem. Soc.* **2014**, *136*, 11680–11686.
- (20) Agrawal, A.; Singh, A.; Yazdi, S.; Singh, A.; Ong, G. K.; Bustillo, K.; Johns, R. W.; Ringe, E.; Milliron, D. J. Resonant Coupling between Molecular Vibrations and Localized Surface Plasmon Resonance of Faceted Metal Oxide Nanocrystals. *Nano Lett.* **2017**, *17*, 2611–2620.
- (21) Gordon, T. R.; Cargnello, M.; Paik, T.; Mangolini, F.; Weber, R. T.; Fornasiero, P.; Murray, C. B. Nonaqueous Synthesis of TiO₂ Nanocrystals Using TiF₄ to Engineer Morphology, Oxygen Vacancy Concentration, and Photocatalytic Activity. *J. Am. Chem. Soc.* **2012**, *134*, 6751–6761.
- (22) Avadhut, Y. S.; Weber, J.; Hammarberg, E.; Feldmann, C.; Schellenberg, I.; Pöttgen, R.; Schmedt auf der Günne, J. Study on the Defect Structure of SnO₂:F Nanoparticles by High-Resolution Solid-State NMR. *Chem. Mater.* **2011**, *23*, 1526–1538.
- (23) Sherry, L. J.; Chang, S.-H.; Schatz, G. C.; Van Duyne, R. P.; Wiley, B. J.; Xia, Y. Localized Surface Plasmon Resonance Spectroscopy of Single Silver Nanocubes. *Nano Lett.* **2005**, *5*, 2034–2038.
- (24) Hoang, T. B.; Akselrod, G. M.; Argyropoulos, C.; Huang, J.; Smith, D. R.; Mikkelsen, M. H. Ultrafast Spontaneous Emission Source Using Plasmonic Nanoantennas. *Nat. Commun.* **2015**, *6*, No. 7788.
- (25) Hsu, S.-W.; Tao, A. R. Halide-Directed Synthesis of Square Prismatic Ag Nanocrystals by the Polyol Method. *Chem. Mater.* **2018**, *30*, 4617–4623.
- (26) Hrelescu, C.; Sau, T. K.; Rogach, A. L.; Jäckel, F.; Feldmann, J. Single Gold Nanostars Enhance Raman Scattering. *Appl. Phys. Lett.* **2009**, *94*, No. 153113.
- (27) Stiles, P. L.; Dieringer, J. A.; Shah, N. C.; Duyne, R. P. V. Surface-Enhanced Raman Spectroscopy. *Annu. Rev. Anal. Chem.* **2008**, *1*, 601–626.
- (28) Coughlan, C.; Ibáñez, M.; Dobrozhan, O.; Singh, A.; Cabot, A.; Ryan, K. M. Compound Copper Chalcogenide Nanocrystals. *Chem. Rev.* **2017**, *117*, 5865–6109.
- (29) Hsu, S.-W.; On, K.; Tao, A. R. Localized Surface Plasmon Resonances of Anisotropic Semiconductor Nanocrystals. *J. Am. Chem. Soc.* **2011**, *133*, 19072–19075.
- (30) Sardar, K.; Deepak, F. L.; Govindaraj, A.; Seikh, M. M.; Rao, C. N. R. InN Nanocrystals, Nanowires, and Nanotubes. *Small* **2005**, *1*, 91–94.
- (31) Palomaki, P. K.; Miller, E. M.; Neale, N. R. Control of Plasmonic and Interband Transitions in Colloidal Indium Nitride Nanocrystals. *J. Am. Chem. Soc.* **2013**, *135*, 14142–14150.
- (32) Kim, J.; Agrawal, A.; Krieg, F.; Bergerud, A.; Milliron, D. J. The Interplay of Shape and Crystalline Anisotropies in Plasmonic Semiconductor Nanocrystals. *Nano Lett.* **2016**, *16*, 3879–3884.
- (33) Toby, B. H.; Von Dreele, R. B. GSAS-II: The Genesis of a Modern Open-Source All Purpose Crystallography Software Package. *J. Appl. Crystallogr.* **2013**, *46*, 544–549.
- (34) Kresse, G.; Furthmüller, J. Efficient Iterative Schemes for Ab Initio Total-Energy Calculations Using a Plane-Wave Basis Set. *Phys. Rev. B* **1996**, *54*, 11169–11186.
- (35) Kresse, G.; Joubert, D. From Ultrasoft Pseudopotentials to the Projector Augmented-Wave Method. *Phys. Rev. B* **1999**, *59*, 1758–1775.
- (36) Perdew, J. P.; Burke, K.; Ernzerhof, M. Generalized Gradient Approximation Made Simple. *Phys. Rev. Lett.* **1996**, *77*, 3865–3868.
- (37) Monkhorst, H. J.; Pack, J. D. Special Points for Brillouin-Zone Integrations. *Phys. Rev. B* **1976**, *13*, 5188–5192.

- (38) Yesinowski, J. P.; Ladouceur, H. D.; Purdy, A. P.; Miller, J. B. Electrical and Ionic Conductivity Effects on Magic-Angle Spinning Nuclear Magnetic Resonance Parameters of CuI. *J. Chem. Phys.* **2010**, *133*, No. 234509.
- (39) Thurber, K. R.; Tycko, R. Measurement of Sample Temperatures under Magic-Angle Spinning from the Chemical Shift and Spin-Lattice Relaxation Rate of ^{79}Br in KBr Powder. *J. Magn. Reson.* **2009**, *196*, 84–87.
- (40) Brouwer, D. H.; Kristiansen, P. E.; Fyfe, C. A.; Levitt, M. H. Symmetry-Based ^{29}Si Dipolar Recoupling Magic Angle Spinning NMR Spectroscopy: A New Method for Investigating Three-Dimensional Structures of Zeolite Frameworks. *J. Am. Chem. Soc.* **2005**, *127*, 542–543.
- (41) Hung, I.; Rossini, A. J.; Schurko, R. W. Application of the Carr–Purcell Meiboom–Gill Pulse Sequence for the Acquisition of Solid-State NMR Spectra of Spin-1/2 Nuclei. *J. Phys. Chem. A* **2004**, *108*, 7112–7120.
- (42) Krivanek, O. L.; Lovejoy, T. C.; Dellby, N.; Carpenter, R. W. Monochromated STEM with a 30 MeV-Wide, Atom-Sized Electron Probe. *Microscopy* **2013**, *62*, 3–21.
- (43) Spiegelberg, J.; Idrobo, J. C.; Herklotz, A.; Ward, T. Z.; Zhou, W.; Ruzs, J. Local Low Rank Denoising for Enhanced Atomic Resolution Imaging. *Ultramicroscopy* **2018**, *187*, 34–42.
- (44) Narayanaswamy, A.; Xu, H.; Pradhan, N.; Kim, M.; Peng, X. Formation of Nearly Monodisperse In_2O_3 Nanodots and Oriented-Attached Nanoflowers: Hydrolysis and Alcoholysis vs Pyrolysis. *J. Am. Chem. Soc.* **2006**, *128*, 10310–10319.
- (45) Pham, H. T.; Jeong, H.-D. Non-Monotonic Size Dependence of Electron Mobility in Indium Oxide Nanocrystals Thin Film Transistor. *Bull. Korean Chem. Soc.* **2014**, *35*, 2505–2511.
- (46) Bronstein, L. M.; Huang, X.; Retrum, J.; Schmucker, A.; Pink, M.; Stein, B. D.; Dragnea, B. Influence of Iron Oleate Complex Structure on Iron Oxide Nanoparticle Formation. *Chem. Mater.* **2007**, *19*, 3624–3632.
- (47) Nakamoto, K. *Infrared and Raman Spectra of Inorganic and Coordination Compounds: Part B: Applications in Coordination, Organometallic, and Bioinorganic Chemistry*; John Wiley & Sons, Inc.: Hoboken, NJ, 2008; Chapter 1, pp 1–273.
- (48) Jin, Y.; Yi, Q.; Ren, Y.; Wang, X.; Ye, Z. Molecular Mechanism of Monodisperse Colloidal Tin-Doped Indium Oxide Nanocrystals by a Hot-Injection Approach. *Nanoscale Res. Lett.* **2013**, *8*, 153.
- (49) Pavia, D. L.; Lampman, G. M.; Kriz, G. S.; Vyvyan, J. A. *Introduction to Spectroscopy*; Cengage Learning: Boston, MA, 2014.
- (50) Zhang, Z.; Zhong, X.; Liu, S.; Li, D.; Han, M. Aminolysis Route to Monodisperse Titania Nanorods with Tunable Aspect Ratio. *Angew. Chem., Int. Ed.* **2005**, *44*, 3466–3470.
- (51) Zhang, Z.; Lu, M.; Xu, H.; Chin, W.-S. Shape-Controlled Synthesis of Zinc Oxide: A Simple Method for the Preparation of Metal Oxide Nanocrystals in Non-Aqueous Medium. *Chem. – Eur. J.* **2007**, *13*, 632–638.
- (52) Wang, F.; Richards, V. N.; Shields, S. P.; Buhro, W. E. Kinetics and Mechanisms of Aggregative Nanocrystal Growth. *Chem. Mater.* **2014**, *26*, 5–21.
- (53) Lounis, S. D.; Runnerstrom, E. L.; Bergerud, A.; Nordlund, D.; Milliron, D. J. Influence of Dopant Distribution on the Plasmonic Properties of Indium Tin Oxide Nanocrystals. *J. Am. Chem. Soc.* **2014**, *136*, 7110–7116.
- (54) Wang, Y.; He, J.; Liu, C.; Chong, W. H.; Chen, H. Thermodynamics versus Kinetics in Nanosynthesis. *Angew. Chem., Int. Ed.* **2015**, *54*, 2022–2051.
- (55) Dean, J. A. *Lange's Handbook of Chemistry*; McGraw-Hill: New York, NY, 1992.
- (56) Yang, H. G.; Sun, C. H.; Qiao, S. Z.; Zou, J.; Liu, G.; Smith, S. C.; Cheng, H. M.; Lu, G. Q. Anatase TiO_2 Single Crystals with a Large Percentage of Reactive Facets. *Nature* **2008**, *453*, 638–641.
- (57) Karsi, N.; Lang, P.; Chehimi, M.; Delamar, M.; Horowitz, G. Modification of Indium Tin Oxide Films by Alkanethiol and Fatty Acid Self-Assembled Monolayers: A Comparative Study. *Langmuir* **2006**, *22*, 3118–3124.
- (58) Walsh, A.; A. Catlow, C. R. Structure, Stability and Work Functions of the Low Index Surfaces of Pure Indium Oxide and Sn-Doped Indium Oxide (ITO) from Density Functional Theory. *J. Mater. Chem.* **2010**, *20*, 10438–10444.
- (59) Jansons, A. W.; Plummer, L. K.; Hutchison, J. E. Living Nanocrystals. *Chem. Mater.* **2017**, *29*, 5415–5425.
- (60) Khurshid, H.; Li, W.; Chandra, S.; Phan, M.-H.; Hadjipanayis, G. C.; Mukherjee, P.; Srikanth, H. Mechanism and Controlled Growth of Shape and Size Variant Core/Shell $\text{FeO}/\text{Fe}_3\text{O}_4$ Nanoparticles. *Nanoscale* **2013**, *5*, 7942–7952.
- (61) Sadoc, A.; Biswal, M.; Body, M.; Legein, C.; Boucher, F.; Massiot, D.; Fayon, F. NMR Parameters in Column 13 Metal Fluoride Compounds (AlF_3 , GaF_3 , InF_3 and TlF) from First Principle Calculations. *Solid State Nucl. Magn. Reson.* **2014**, *59–60*, 1–7.
- (62) Shannon, R. D. Revised Effective Ionic Radii and Systematic Studies of Interatomic Distances in Halides and Chalcogenides. *Acta Crystallogr., Sect. A: Found. Adv.* **1976**, *32*, 751–767.
- (63) Ramaiah, K. S.; Raja, V. S. Structural and Electrical Properties of Fluorine Doped Tin Oxide Films Prepared by Spray-Pyrolysis Technique. *Appl. Surf. Sci.* **2006**, *253*, 1451–1458.
- (64) Maruyama, T.; Nakai, T. Fluorine-doped Indium Oxide Thin Films Prepared by Chemical Vapor Deposition. *J. Appl. Phys.* **1992**, *71*, 2915–2917.
- (65) Frank, G.; Köstlin, H. Electrical Properties and Defect Model of Tin-Doped Indium Oxide Layers. *Appl. Phys. A* **1982**, *27*, 197–206.
- (66) Zhou, X.-D.; Huebner, W. Size-Induced Lattice Relaxation in CeO_2 Nanoparticles. *Appl. Phys. Lett.* **2001**, *79*, 3512–3514.
- (67) Nadaud, N.; Lequeux, N.; Nanot, M.; Jové, J.; Roisnel, T. Structural Studies of Tin-Doped Indium Oxide (ITO) and $\text{In}_4\text{Sn}_3\text{O}_{12}$. *J. Solid State Chem.* **1998**, *135*, 140–148.
- (68) Akkad, F. E.; Joseph, S. Physicochemical Characterization of Point Defects in Fluorine Doped Tin Oxide Films. *J. Appl. Phys.* **2012**, *112*, No. 023501.
- (69) Costa, B. J.; Soufiane, A.; Messaddeq, Y. New Compositions of Fluoroindate Glasses with Higher Chemical Resistance. *Quím. Nova* **1998**, *21*, 370–371.
- (70) Li, J.; Liu, C.; Ye, Y.; Zhu, J.; Wang, S.; Guo, J.; Sham, T.-K. Tracking the Local Effect of Fluorine Self-Doping in Anodic TiO_2 Nanotubes. *J. Phys. Chem. C* **2016**, *120*, 4623–4628.
- (71) Kröger, F. A.; Vink, H. J. Relations between the Concentrations of Imperfections in Crystalline Solids. In *Solid State Physics*; Seitz, F., Turnbull, D., Eds.; Academic Press, 1956; Vol. 3, pp 307–435.
- (72) Walsh, A. Surface Oxygen Vacancy Origin of Electron Accumulation in Indium Oxide. *Appl. Phys. Lett.* **2011**, *98*, No. 261910.
- (73) Runnerstrom, E. L.; Kelley, K. P.; Sachet, E.; Shelton, C. T.; Maria, J.-P. Epsilon-near-Zero Modes and Surface Plasmon Resonance in Fluorine-Doped Cadmium Oxide Thin Films. *ACS Photonics* **2017**, *4*, 1885–1892.
- (74) Seo, J.-S.; Jeon, J.-H.; Hwang, Y. H.; Park, H.; Ryu, M.; Park, S.-H. K.; Bae, B.-S. Solution-Processed Flexible Fluorine-Doped Indium Zinc Oxide Thin-Film Transistors Fabricated on Plastic Film at Low Temperature. *Sci. Rep.* **2013**, *3*, No. 2085.
- (75) Schimpf, A. M.; Ochsenbein, S. T.; Buonsanti, R.; Milliron, D. J.; Gamelin, D. R. Comparison of Extra Electrons in Colloidal N-Type Al^{3+} -Doped and Photochemically Reduced ZnO Nanocrystals. *Chem. Commun.* **2012**, *48*, 9352–9354.
- (76) Schimpf, A. M.; Gunthardt, C. E.; Rinehart, J. D.; Mayer, J. M.; Gamelin, D. R. Controlling Carrier Densities in Photochemically Reduced Colloidal ZnO Nanocrystals: Size Dependence and Role of the Hole Quencher. *J. Am. Chem. Soc.* **2013**, *135*, 16569–16577.
- (77) Zhang, L.; Yin, L.; Wang, C.; lun, N.; Qi, Y.; Xiang, D. Origin of Visible Photoluminescence of ZnO Quantum Dots: Defect-Dependent and Size-Dependent. *J. Phys. Chem. C* **2010**, *114*, 9651–9658.
- (78) Whitaker, K. M.; Ochsenbein, S. T.; Polinger, V. Z.; Gamelin, D. R. Electron Confinement Effects in the EPR Spectra of Colloidal N-Type ZnO Quantum Dots. *J. Phys. Chem. C* **2008**, *112*, 14331–14335.

- (79) De Trizio, L.; Buonsanti, R.; Schimpf, A. M.; Llordes, A.; Gamelin, D. R.; Simonutti, R.; Milliron, D. J. Nb-Doped Colloidal TiO₂ Nanocrystals with Tunable Infrared Absorption. *Chem. Mater.* **2013**, *25*, 3383–3390.
- (80) Yamakawa, N.; Jiang, M.; Key, B.; Grey, C. P. Identifying the Local Structures Formed during Lithiation of the Conversion Material, Iron Fluoride, in a Li Ion Battery: A Solid-State NMR, X-Ray Diffraction, and Pair Distribution Function Analysis Study. *J. Am. Chem. Soc.* **2009**, *131*, 10525–10536.
- (81) Kiczynski, T. J.; Stebbins, J. F. Fluorine Sites in Calcium and Barium Oxyfluorides: F-19 NMR on Crystalline Model Compounds and Glasses. *J. Non-Cryst. Solids* **2002**, *306*, 160–168.
- (82) Kiczynski, T. J.; Stebbins, J. F. The Effect of Fictive Temperature on the Structural Environment of Fluorine in Silicate and Aluminosilicate Glasses. *J. Am. Ceram. Soc.* **2006**, *89*, 57–64.
- (83) Yesinowski, J. P. Solid-State NMR of Inorganic Semiconductors. In *Solid State NMR*; Chan, J. C. C., Ed.; Springer: Berlin, Heidelberg, 2012; pp 229–312.
- (84) Yesinowski, J. P.; Berkson, Z. J.; Cadars, S.; Purdy, A. P.; Chmelka, B. F. Spatially Correlated Distributions of Local Metallic Properties in Bulk and Nanocrystalline GaN. *Phys. Rev. B* **2017**, *95*, No. 235201.
- (85) Knight, W. D. Nuclear Magnetic Resonance Shift in Metals. *Phys. Rev.* **1949**, *76*, 1259–1260.
- (86) Slichter, C. P. *Principles of Magnetic Resonance*, 3rd ed.; Springer: Berlin, Heidelberg, 1990.
- (87) Korringa, J. Nuclear Magnetic Relaxation and Resonance Line Shift in Metals. *Physica* **1950**, *16*, 601–610.
- (88) Zapart, W.; Zapart, M. B.; Zhukov, A. P.; Popolitov, V. I.; Shuvalov, L. A. Phase Transition in In₃Sb₅O₁₂ by NQR of ¹¹⁵In Nuclei. *Phys. Lett. A* **1987**, *121*, 248–250.
- (89) Han, O. H.; Timken, H. K. C.; Oldfield, E. Solid-state “Magic-angle” Sample-spinning Nuclear Magnetic Resonance Spectroscopic Study of Group III–V (13–15) Semiconductors. *J. Chem. Phys.* **1988**, *89*, 6046–6052.
- (90) Jung, W.-S.; Han, O. H.; Chae, S.-A. Characterization of Wurtzite Indium Nitride Synthesized from Indium Oxide by In-115 MAS NMR Spectroscopy. *Mater. Lett.* **2007**, *61*, 3413–3415.
- (91) Schurko, R. W. Ultra-Wideline Solid-State NMR Spectroscopy. *Acc. Chem. Res.* **2013**, *46*, 1985–1995.
- (92) Pell, A. J.; Pintacuda, G. Broadband Solid-State MAS NMR of Paramagnetic Systems. *Prog. Nucl. Magn. Reson. Spectrosc.* **2015**, *84–85*, 33–72.
- (93) Kim, J.; Ilott, A. J.; Middlemiss, D. S.; Chernova, N. A.; Pinney, N.; Morgan, D.; Grey, C. P. ²H and ²⁷Al Solid-State NMR Study of the Local Environments in Al-Doped 2-Line Ferrihydrite, Goethite, and Lepidocrocite. *Chem. Mater.* **2015**, *27*, 3966–3978.
- (94) Yin, P.; Hegde, M.; Tan, Y.; Chen, S.; Garnet, N.; Radovanovic, P. V. Controlling the Mechanism of Excitonic Splitting in In₂O₃ Nanocrystals by Carrier Delocalization. *ACS Nano* **2018**, *12*, 11211–11218.
- (95) Nicoletti, O.; de la Peña, F.; Leary, R. K.; Holland, D. J.; Ducati, C.; Midgley, P. A. Three-Dimensional Imaging of Localized Surface Plasmon Resonances of Metal Nanoparticles. *Nature* **2013**, *502*, 80–84.
- (96) Naumov, I. I.; Li, Z.; Bratkovsky, A. M. Plasmonic Resonances and Hot Spots in Ag Octopods. *Appl. Phys. Lett.* **2010**, *96*, No. 033105.
- (97) Mulvihill, M. J.; Ling, X. Y.; Henzie, J.; Yang, P. Anisotropic Etching of Silver Nanoparticles for Plasmonic Structures Capable of Single-Particle SERS. *J. Am. Chem. Soc.* **2010**, *132*, 268–274.
- (98) García de Abajo, F. J. Optical Excitations in Electron Microscopy. *Rev. Mod. Phys.* **2010**, *82*, 209–275.
- (99) Hachtel, J. A.; Lupini, A. R.; Idrobo, J. C. Exploring the Capabilities of Monochromated Electron Energy Loss Spectroscopy in the Infrared Regime. *Sci. Rep.* **2018**, *8*, No. 5637.
- (100) Li, G.; Cherqui, C.; Bigelow, N. W.; Duscher, G.; Straney, P. J.; Millstone, J. E.; Masiello, D. J.; Camden, J. P. Spatially Mapping Energy Transfer from Single Plasmonic Particles to Semiconductor Substrates via STEM/EELS. *Nano Lett.* **2015**, *15*, 3465–3471.
- (101) Ringe, E.; DeSantis, C. J.; Collins, S. M.; Duchamp, M.; Dunin-Borkowski, R. E.; Skrabalak, S. E.; Midgley, P. A. Resonances of Nanoparticles with Poor Plasmonic Metal Tips. *Sci. Rep.* **2015**, *5*, No. 17431.
- (102) Johns, R. W.; Bechtel, H. A.; Runnerstrom, E. L.; Agrawal, A.; Lounis, S. D.; Milliron, D. J. Direct Observation of Narrow Mid-Infrared Plasmon Linewidths of Single Metal Oxide Nanocrystals. *Nat. Commun.* **2016**, *7*, No. 11583.
- (103) Akselrod, G. M.; Weidman, M. C.; Li, Y.; Argyropoulos, C.; Tisdale, W. A.; Mikkelsen, M. H. Efficient Nanosecond Photoluminescence from Infrared PbS Quantum Dots Coupled to Plasmonic Nanoantennas. *ACS Photonics* **2016**, *3*, 1741–1746.
- (104) Cao, S.; Zhang, S.; Zhang, T.; Lee, J. Y. Fluoride-Assisted Synthesis of Plasmonic Colloidal Ta-Doped TiO₂ Nanocrystals for Near-Infrared and Visible-Light Selective Electrochromic Modulation. *Chem. Mater.* **2018**, *30*, 4838–4846.

Supporting Information

Syntheses of Colloidal F:In₂O₃ Cubes: Fluorine-Induced Faceting and Infrared Plasmonic Response

Shin Hum Cho[†], Sandeep Ghosh[†], Zachariah J. Berkson[‡], Jordan A. Hachtel[§], Jianjian Shi^{||}, Xunhua Zhao^{||}, Lauren C. Reimnitz[†], Clayton J. Dahlman^{†±}, Yujing Ho[†], Anni Yang[†], Yuanyue Liu^{||}, Juan-Carlos Idrobo[§], Bradley F. Chmelka^{*‡}, Delia J. Milliron^{*†}

[†] McKetta Department of Chemical Engineering, The University of Texas at Austin, Austin, Texas 78712, United States

[‡] Department of Chemical Engineering, University of California, Santa Barbara, California 93106, United States

[§] Center for Nanophase Materials Science, Oak Ridge National Laboratory, Oak Ridge, Tennessee 37831, USA

^{||} Texas Materials Institute and Department of Mechanical Engineering, The University of Texas at Austin, Austin, Texas 78712, United States

[±] Materials Department, University of California, Santa Barbara, Engineering II Building 1355, Santa Barbara, CA 93106-5050, USA

Corresponding Author

D. J. Milliron, E-mail: milliron@che.utexas.edu.

B. F. Chmelka, E-mail: bradc@engineering.ucsb.edu

Author Contributions

S. H. Cho, S. Ghosh, and Z. J. Berkson contributed equally.

Contents

Figure S1. Cube and Concave Cube SEM Images.....	3
Figure S2. SEM Images of More Highly Doped F:In ₂ O ₃ NCs.....	4
Figure S3. EDX Spectra.....	5
Figure S4. TOF-SIMS	6
Figure S5. F:In ₂ O ₃ Cube Aliquots	7
Figure S6. Temperature and Reaction Time NC Series.....	8
Figure S7. Cl, Br Doped NC SEM Image.....	9
Figure S8. XPS Analysis.....	10
Figure S9. In ₂ O ₃ Supercell.....	11
Text S1. DFT Calculation	12
Text S2. Solid-State ¹⁹ F and ¹¹⁵ In NMR.....	18
Figure S10. Solid-State 1D ¹ H{ ¹⁹ F} MAS NMR Spectra.....	19
Figure S11. Quantitative ¹⁹ F MAS NMR Spectra	20
Figure S12. XRD Patterns.....	21
Figure S13. F:In ₂ O ₃ Cube NC TGA	22
Figure S14. Undoped In ₂ O ₃ and F-doped In ₂ O ₃ Band Structure.....	23
Figure S15. EPR Spectra.....	24
Figure S16. Knight-Korringa Relation.....	25
Table S1. ¹¹⁵ In Simulated Lineshape Parameter	26
Figure S17. XRD Pattern of Undoped Bulk In ₂ O ₃	26
Figure S18. Photograph of NC Dispersions.....	27
Figure S19. Drude Model Extinction Curve	27
Figure S20. F:In ₂ O ₃ Cube NC Aliquot FTIR.....	28
Text S3. Modal Deconvolution of Monochromated EELS Data.....	29
Figure S21. EELS Background Subtraction and Denoising.....	31
Figure S22. Corner and Edge Modes for 1%, 2%, and 3% InF ₃ Doping Concentrations.....	31
Figure S23. Effect of Number of Components on Deconvoluted Plasmon Modes.....	32
Text S4. Surface Fluorine Estimation	33
References	34

Figure S1. Cube and Concave Cube SEM Images

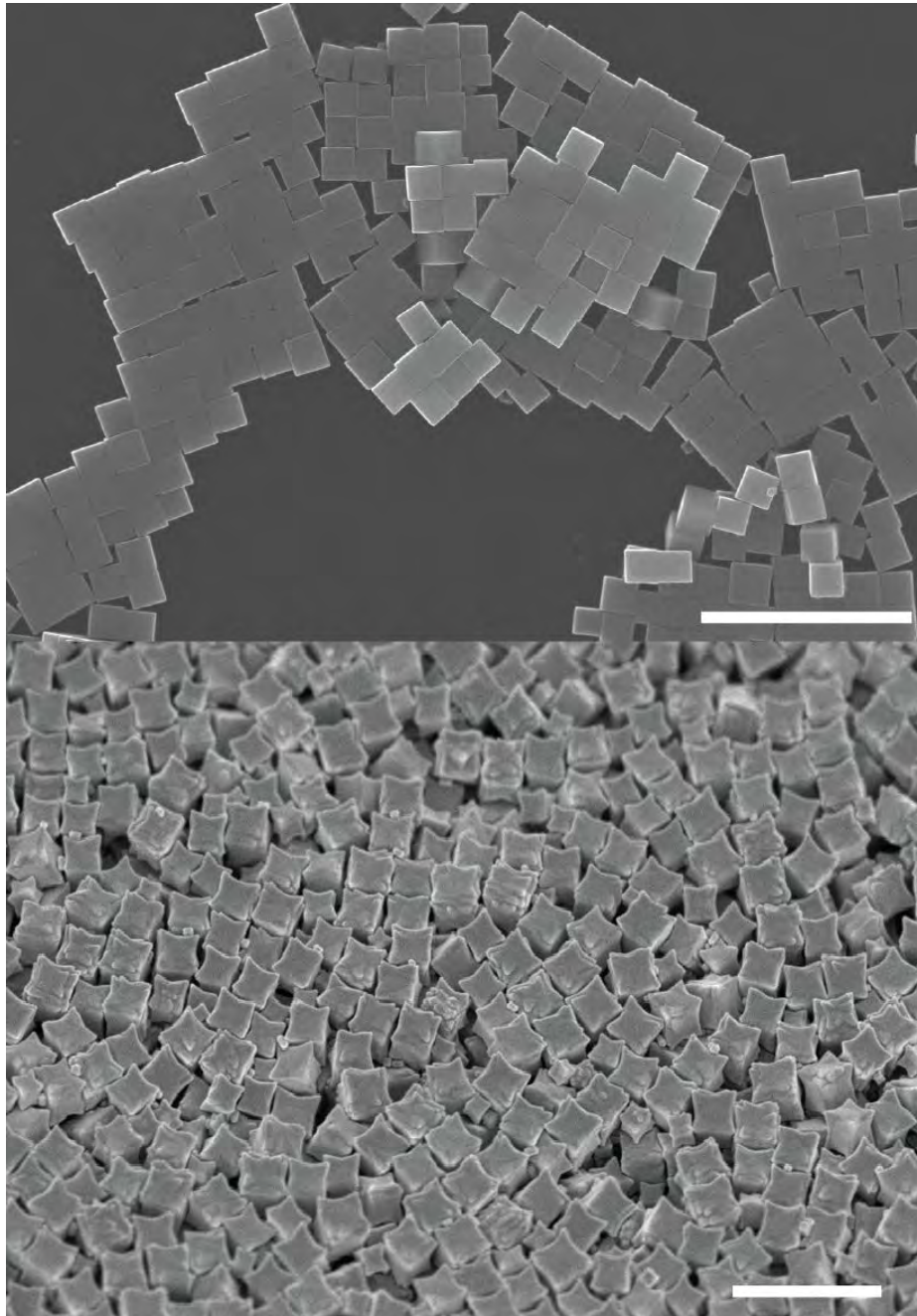


Figure S1. SEM image of F:In₂O₃ (3% InF₃) cube NCs (top) and F:In₂O₃ concave cube (1% InF₃) NCs (bottom left) dropcast on Si substrates. Scale bars are 1 μ m.

Figure S2. SEM Images of More Highly Doped F:In₂O₃ NCs

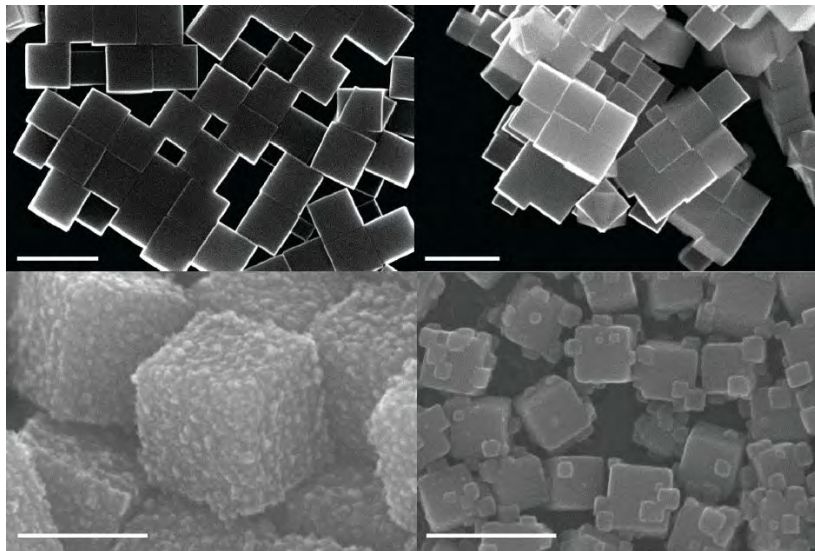


Figure S2. SEM images of F:In₂O₃ (4% InF₃) cube NCs (top left), F:In₂O₃ (5% InF₃) cube NCs (top right), F:In₂O₃ (6% InF₃) cube NCs (bottom left), and F:In₂O₃ (12% InF₃) NCs (bottom right). Defective surfaces are observed in F:In₂O₃ NCs using 6% and 12% InF₃. Scale bars are 500 nm, 500 nm, 200 nm, and 400 nm, respectively.

Figure S3. EDX Spectra

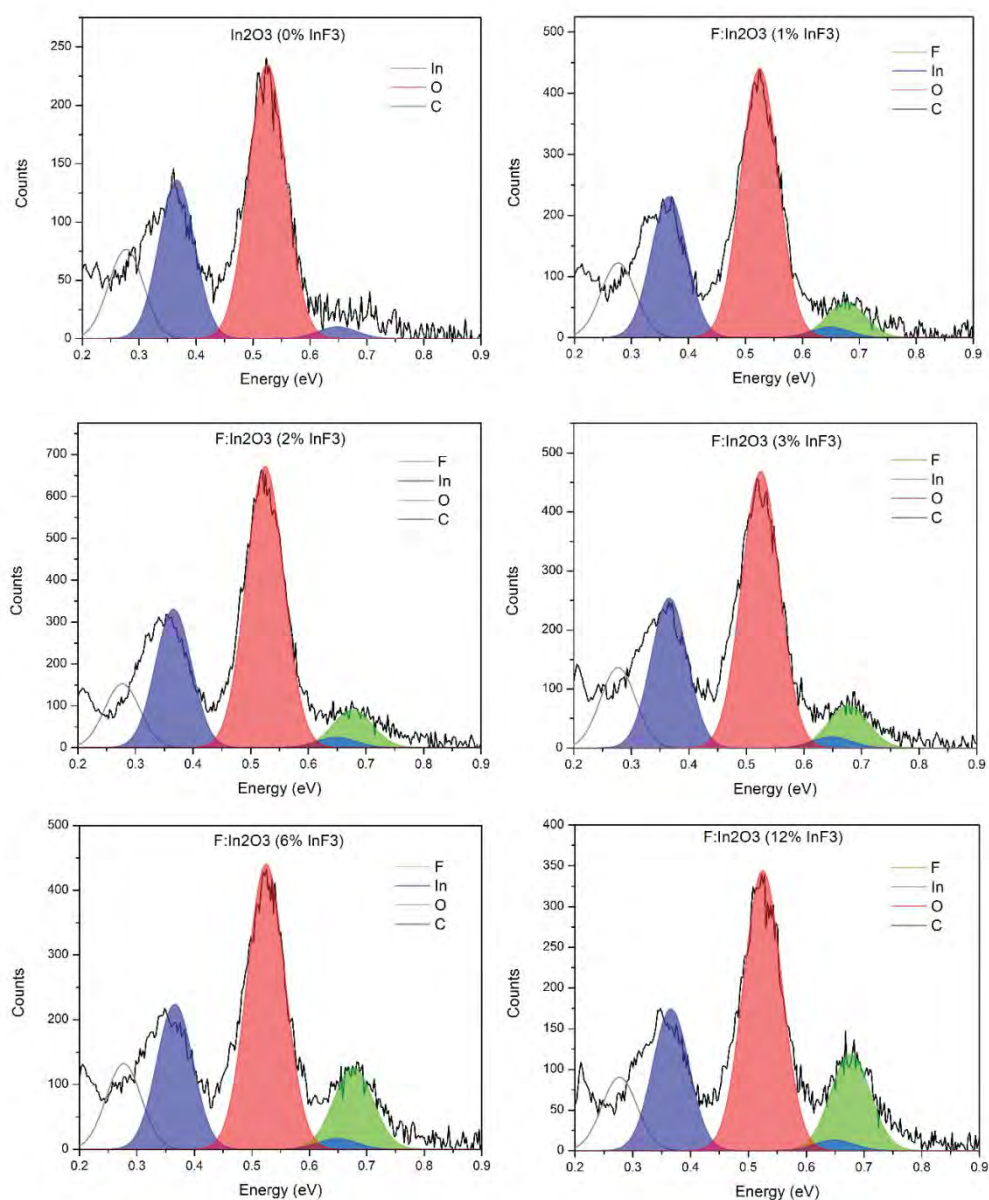


Figure S3. EDX spectra of F: In_2O_3 NCs. (a) In_2O_3 NCs (0% InF_3), (b) F: In_2O_3 NCs (1% InF_3), (c) F: In_2O_3 NCs (2% InF_3), (d) F: In_2O_3 NCs (3% InF_3), (e) F: In_2O_3 NCs (6% InF_3), and (f) F: In_2O_3 NCs (12% InF_3).

Figure S4. TOF-SIMS

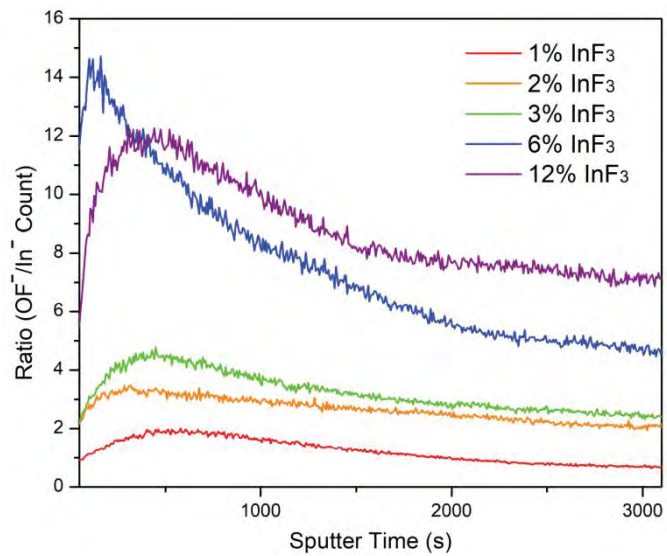


Figure S4. TOF-SIMS data acquisition of secondary ions (OF⁻, In⁻) ratio count from dropcast F:In₂O₃ NC (1-12% InF₃) films, with sputtering time until non-corrugated averaged composition ratio is attained for relative comparison with EDX.

Figure S5. F:In₂O₃ Cube Aliquots

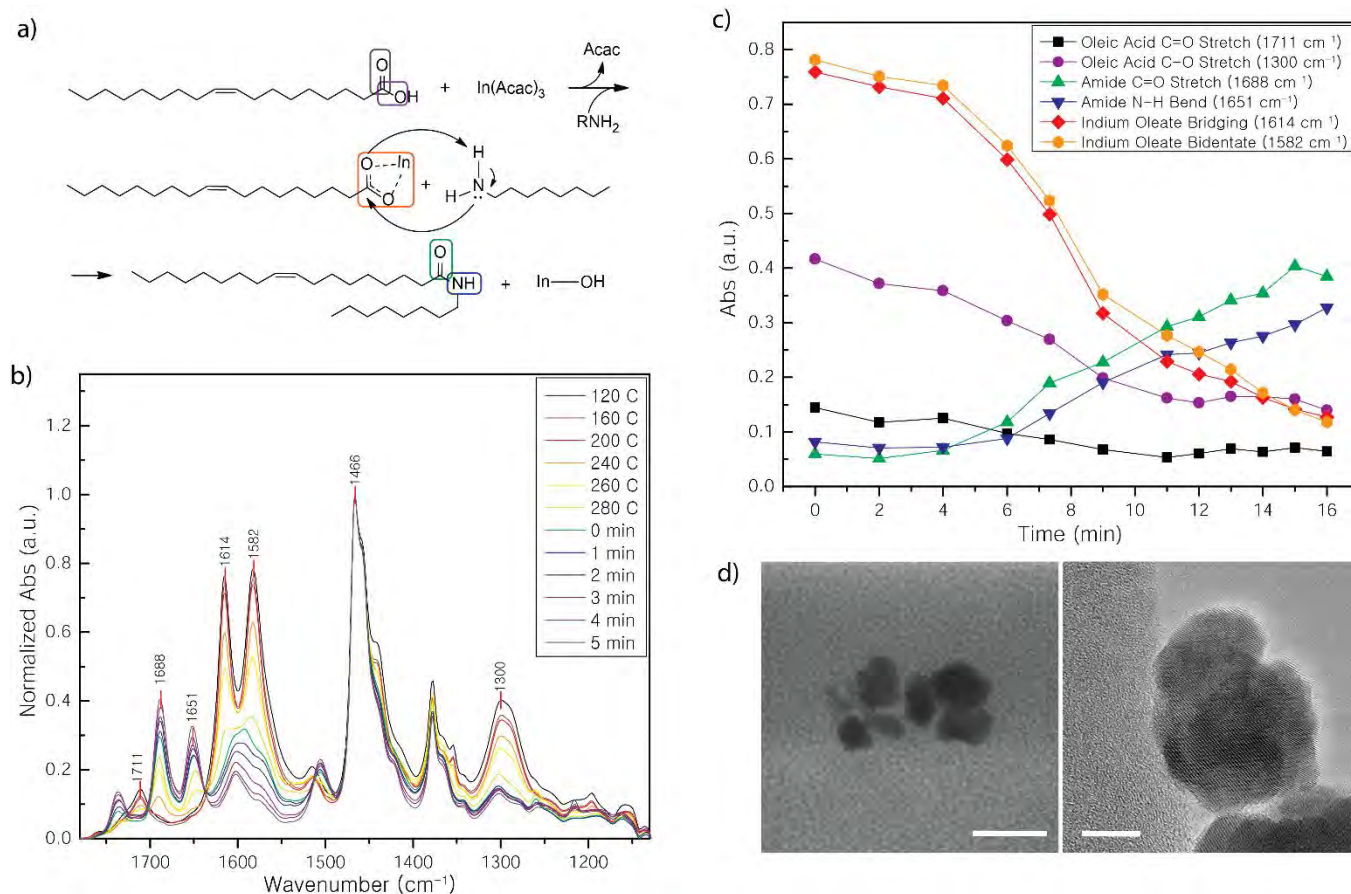


Figure S5. (a) Aminolysis scheme with indium oleate undergoing aminolysis with octylamine, leading to amide byproduct formation. (b) FTIR fingerprint region of F:In₂O₃ cube NC (3% InF₃) aliquots taken during reaction. (c) Bridging and bidentate peaks from indium oleate precursor are observed to rapidly decompose during heat-up synthesis. Increasing IR peak intensity from F:In₂O₃ cube aliquots are assigned to C=O stretching and N-H bending vibrations in the amide byproduct. (d) F:In₂O₃ (3% InF₃) irregular aggregate aliquot taken at 280 °C imaged with STEM (left). Lattice alignment is observed in HRTEM, indicative of nuclei oriented attachment (right). Scale bars are 200 nm, and 10 nm, respectively.

Figure S6. Temperature and Reaction Time NC Series

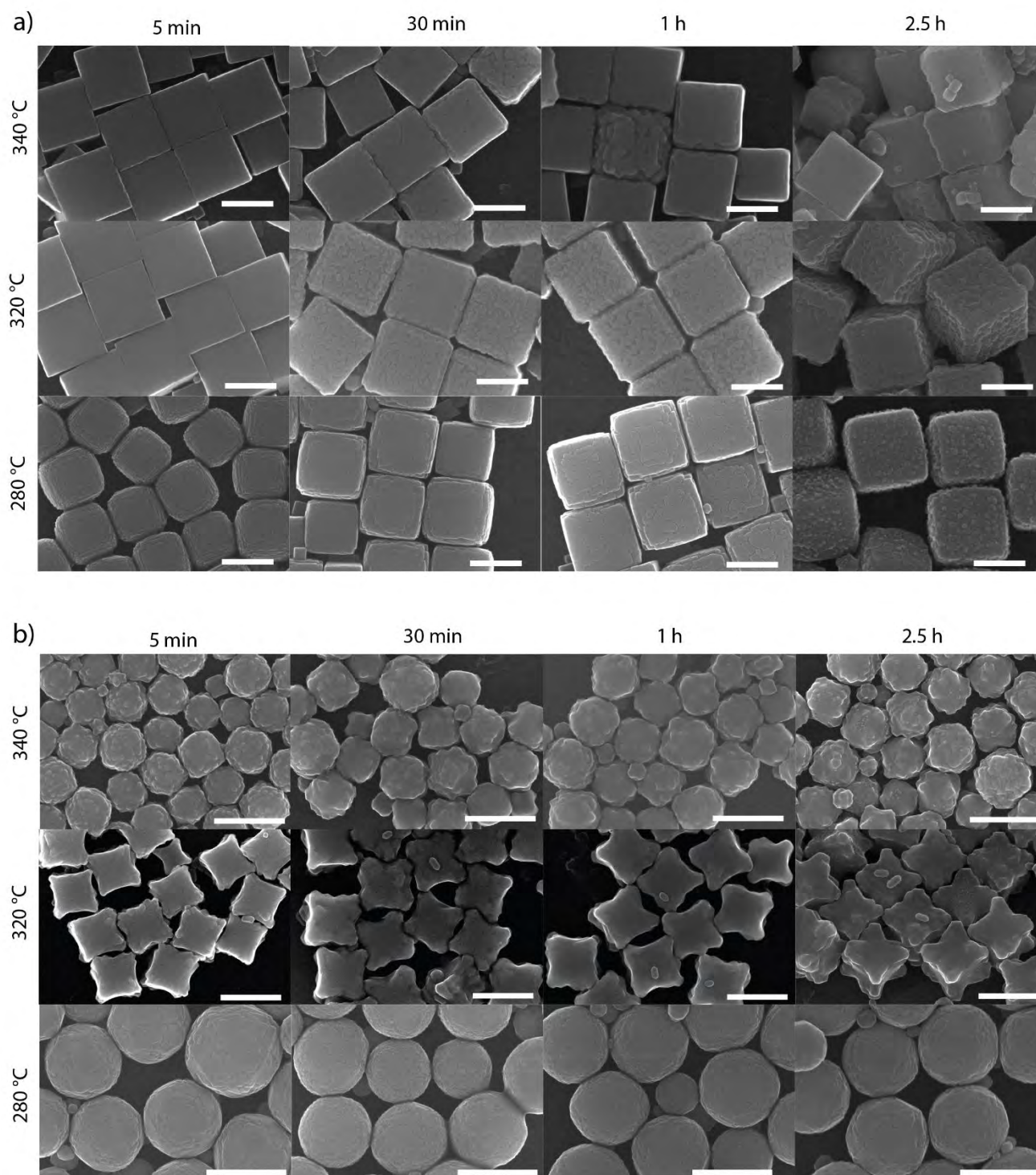


Figure S6. (a) Cube (3% InF₃) and (b) concave cube F:In₂O₃ NC (1% InF₃) growth aliquots at 5 min, 30 min, 1 h, and 2.5 h were taken to reveal growth time influence on NC shape. Reaction time aliquot series with varying reaction temperatures at 280 °C, 320 °C, and 340 °C. Scale bars are 250 nm in Figure a, and 500 nm in Figure b.

Figure S7. Cl, Br Doped NC SEM Image

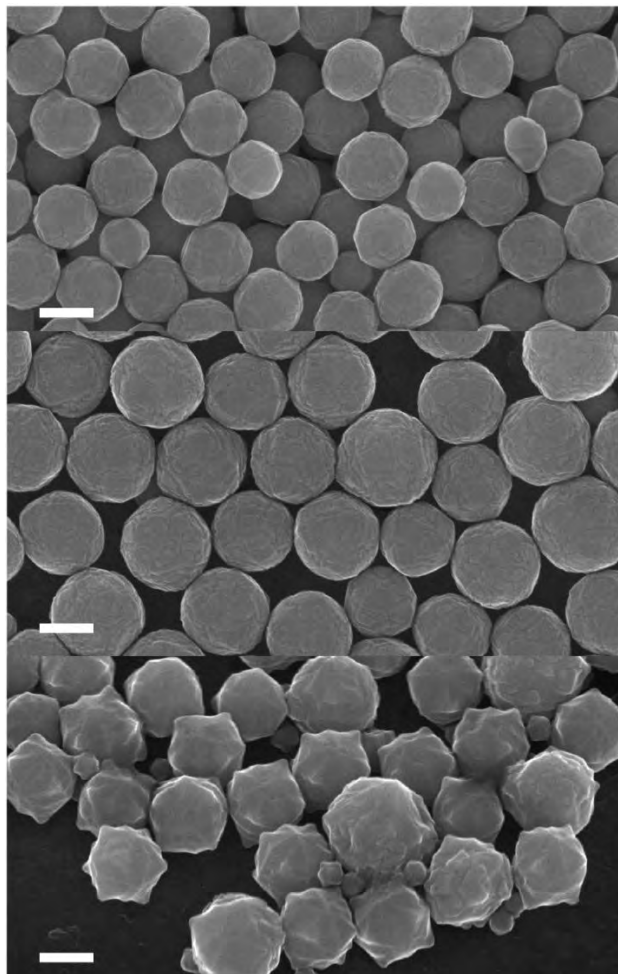


Figure S7. SEM images of rounded Cl:In₂O₃ (3% InCl₃) (top), Br:In₂O₃ (3% InBr₃) (middle), and undoped In₂O₃ (0% InF₃) NCs (bottom). Scale bars are 200 nm.

Figure S8. XPS Analysis

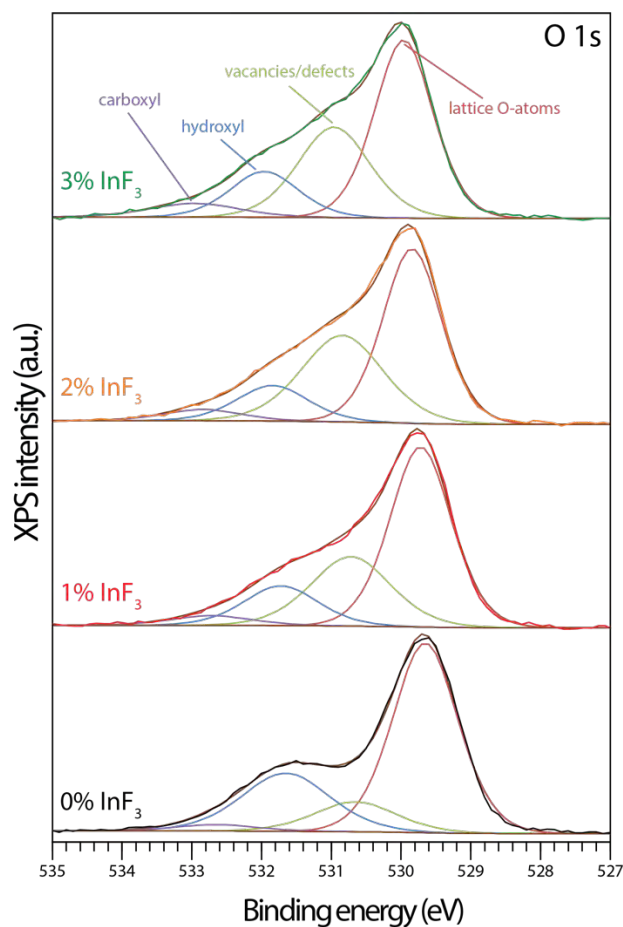


Figure S8. O 1s XPS spectra for undoped In₂O₃ NCs (black curve), concave cube (red curve), sharp concave cube (orange curve), cube (green curve) F:In₂O₃ NCs. The spectra were further deconvoluted into 530.0 eV, 531.0 eV, 531.8 eV, and 533.1 eV components assignable to lattice oxygen (red), oxygen adjacent to oxygen vacancies or other defects (green), and surface hydroxyl (blue), and carboxyl (purple) oxygen species, respectively.

Figure S9. In₂O₃ Supercell

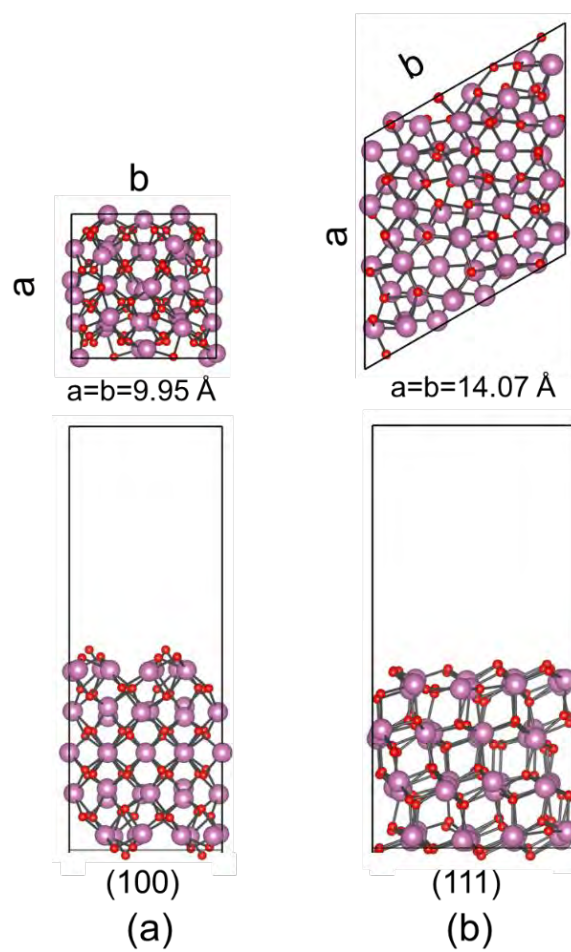


Figure S9. Top and side views of (a) In₂O₃ (100) and (b) In₂O₃ (111) supercells used in DFT calculations.

Text S1. DFT Calculation

DFT calculations were performed using the Vienna Ab-initio Simulation Package (VASP)^{1,2} with PAW pseudopotentials³ in the package. The Perdew-Burke-Ernzerhof (PBE) exchange-correlation functional⁴ was used in all the DFT calculations. A $3 \times 3 \times 1$ Monkhorst-Pack k point mesh for the Brillouin zone integration and a vacuum layer of 15 Å to prevent interactions between periodic images of the slab were used. A kinetic energy cut-off of 400 eV was used for the plane-wave expansion, and all atomic positions were fully relaxed until the final force on each atom was less than 0.01 eV/Å. For NMR calculations, a higher kinetic energy cut-off (600 eV) was used.

The formation energy of F substitution (F_O) is calculated as following

$$E_f = E(\text{surface w } F_O) - E(\text{surface}) + \mu(O)/2 - \mu(F)/2 \quad (1)$$

Where $E(\text{surface})$ and $E(\text{surface w } F_O)$ are the total energies of surface and surface with one F substituting O. $\mu(O)$ and $\mu(F)$ are chemical potentials of O and F. Since $\mu(O)$ and $\mu(F)$ are independent of different substitution sites, the relative formation energy depends only on the first two terms.

A linear relation was used for converting the DFT calculated NMR isotropic shielding σ_{iso} into the chemical shifts (δ). Five fluorides LiF, NaF, KF, CaF₂, BaF₂ were selected to get the linear relation, an expression agreeing with a previously published result⁵:

$$\delta = -0.83 \sigma_{\text{iso}} + 95 \quad (2)$$

Coordinates for In₂O₃ (100) and In₂O₃ (111) structures in VASP CONTCAR format are as follows:

In₂O₃ (100)

```
9.9479999542000002    0.0000000000000000    0.0000000000000000
0.0000000000000000    9.9479999542000002    0.0000000000000000
0.0000000000000000    0.0000000000000000    27.7336997986000000
```

```
In  O
40  60
```

Direct

```
0.7525169732919569    0.0296396430709342    0.1337636414651940
0.7477826996679984    0.4710382993187525    0.3253429990272371
0.2600062118907686    0.4766770192503617    0.1315532765146359
0.7497198736438193    0.7502797525315665    0.2293038077463887
0.4599288701440778    0.0003446014506734    0.2297026591439707
0.0017698430935349    0.7467022479679470    0.1448448708017381
0.4981164739838813    0.2467147270642133    0.1448860548847348
0.4979456256022348    0.7534195680840700    0.3141978917808199
0.0399981163248213    0.5003344941650454    0.2296848808841525
0.2501526969168987    0.7498834438026912    0.2292678509678731
-0.0047885174780774 -0.0574659863919370    0.0333044737218666
-0.0042503524105405    0.0563746103127683    0.4258866439707051
0.5050026671830469    0.4422890021584604    0.0333175862846791
0.5042343817789179    0.5564298911086245    0.4258823802554133
0.0020604979455072    0.2534160184889672    0.3142066020896721
0.2399995638756793    0.0229628782840355    0.3276359426849331
0.7502793484644377    0.2503321228746266    0.2293202744097023
```

0.2498089396404409	0.2499428868140885	0.2292822632356146
0.2600031523306698	0.5229652579071387	0.3276370324307730
0.2399421985619636	0.9766121746162600	0.1315575232085610
0.7522122471697704	0.9710351801311849	0.3253386906373043
0.2113979140157464	0.2865717132214902	0.0319566721134606
0.2889017461806254	0.2129191576747469	0.4272949439382301
0.9361674038988517	0.4784752040249644	0.0381305867042806
0.9361965410362508	0.5212675300149441	0.4211697661637093
0.4893766215369506	0.2535532304156948	0.3380040311979366
0.0106493262495978	0.7535452227859080	0.3379948479076575
0.0106768218830828	0.2471999959501957	0.1211238803246735
0.5638044778384135	-0.0214700561065124	0.0381399438889196
0.5638111183098856	0.0212089241596164	0.4211659947842135
0.7881682082562118	0.2331509133245561	0.0343569734073174
0.7124090361489703	0.2663289073340482	0.4247625537024564
0.5342590354486102	0.4999851386299261	0.2296377012729126
0.9657379314920804	-0.0000309288883032	0.2296444613560615
0.4893226625256925	0.7472019454628481	0.1211229706882783
0.7474463920191496	0.5296032637316064	0.1337167275970441
0.2886169305173190	0.7865955297889300	0.0319432736595537
0.2110757134266596	0.7130067673589524	0.4273022253393339
0.7119032296535994	0.7334314645938868	0.0343556795763899
0.7875929893143747	0.7663705886083737	0.4247388152022506
0.3884419833857574	0.1550157107652663	0.2799337171893533
0.6158999466758619	0.1040990141292275	0.1888855530569733
0.1174327257975349	0.8944746220722891	0.1904966953261887
0.1593899450025471	0.1300643020536721	0.0815947389622075
0.1439413335934321	0.1307423295655144	0.4723996315788169
0.1095194980830849	0.1591982133171590	0.3704731823972385
0.1176651014425633	0.1054837092421697	0.2685677598023457
0.1436196471068065	0.8685260962938727	-0.0131970692442131
0.1589731051490081	0.8704232590919755	0.3779995890429362
0.6157213737294746	0.8961636070758643	0.2702435831244483
0.3823306114131919	0.6054838144759236	0.2685656391121452
0.8840433842921706	0.6040557964378119	0.1888530593944245
0.9899096914445744	0.2948268570656142	0.0031812175192541
0.8847345251973645	0.3435454787822231	0.3831410200271899
0.1606452499276839	0.3798866868639343	0.2828842385223458
0.6076651832660396	0.3458572628973305	0.2803063222864412
0.8928849152334810	0.1542265218806211	0.1787823480318239
0.6155654116057114	0.1565053197573417	0.0760250474607713
0.5104012442276754	0.2048979430543249	0.4560765295087074
0.8842749174322980	0.3961748433692661	0.2702572042448862
0.3824965950742543	0.3945320848066564	0.1905087078870896
0.1601936534740032	0.6200153854533089	0.1760703434564908
0.1110855839945480	0.3457938588937585	0.1792055539063989
0.3405806582594754	0.6301359601502390	0.0816002010822904
0.3560456960149171	0.6308224271921790	0.4723967381185763
0.3397041259251773	0.1199959517441305	0.1760878600638962
0.3904752958914073	0.3406524284150912	0.0886874885386576
0.3393099877048139	0.8798578667126176	0.2828796309348585
0.3566137102232974	0.3682006466986895	-0.0131657219132079
0.3410017902058393	0.3703825517084519	0.3780000223471583
0.8844048165991567	0.6564758455585699	0.0759982139732335
0.9895988496436332	0.7049728305630563	0.4560736150000165
0.1114879291529695	0.5736888476594835	0.3797314790056293
0.7104029863806860	0.4162037990148684	0.0058613598785576
0.6071858437236053	0.4121832495239300	0.3812010105716666
0.6554473741649393	0.6235661590261274	0.2821723882838827
0.6071101112571776	0.6541979378741175	0.1787569478842874

0.6066778550311418	0.5877520185911750	0.0778786110678378
0.7098807725940578	0.5834208040981355	0.4533579961342082
0.6552492453086789	0.3769323005654893	0.1767905852062364
0.1116992162975002	0.4264715764536274	0.0793364461005822
0.8933594093354014	0.0876858132972737	0.0779475300044535
0.7900965406133152	0.0833190302267801	0.4533557807720184
0.3885298761429513	0.0736288416682970	0.3797292897079259
0.3888978565261295	0.8457797816745890	0.1792112916104437
0.6586335974106767	0.8644753820155902	0.0967791903878677
0.1095073129462155	0.8405984695469069	0.0886576474975356
0.3904803188671857	0.6592119385396182	0.3704650339317172
0.1115343662718217	0.6549808925068831	0.2799213290299286
0.3882922770634633	0.9264646767581304	0.0793451975262456
0.7897248171752193	0.9165078456184568	0.0058729495753927
0.8928312569140008	0.9121841666762877	0.3811787107038878
0.6582929050922557	0.1355779520084339	0.3624536751177566
0.5101836990114385	0.7949738088861631	0.0031551036292739
0.6152789110528384	0.8435395540508912	0.3831040463950261
0.8445591602815878	0.1235777095666033	0.2821818433161787
0.8417248571614886	0.6355753607003869	0.3624464501418229
0.8923208957783165	0.8458318922419762	0.2802988359865186
0.8413566805174200	0.3644189638308232	0.0967646116227202
0.8447284555368183	0.8769202921944323	0.1767924292001187

In₂O₃ (111)

14.0685997009000001	0.0000000000000000	0.0000000000000000
-7.0342998505000001	12.1837647367000006	0.0000000000000000
0.0000000000000000	0.0000000000000000	25.6667995453000017

In O
64 96

Direct

0.4777457936155412	0.5969713902261118	0.1536993152334679
0.1493200916028093	0.9355548285163289	0.3979098777408613
0.0012029428917768	0.1436799571452807	0.1427701379866635
0.6712212496064648	0.4823743805724157	0.3768676110307334
0.5018432345652923	0.1406297859445554	0.1349643778521953
0.1693135063379162	0.4770415458959228	0.3854230337916097
0.7387448616954033	0.8708347538435874	0.1478186141299877
0.3998994965084183	0.1917752829763495	0.3875537108944304
0.7486227798490087	0.6083022325095204	0.1348748213820898
0.4172768202551556	0.9403336557131279	0.3850775117104618
0.5129792652686549	0.8803943758426378	0.1534383447165133
0.1742564396334660	0.2140300687528076	0.3980575112544535
0.5118655536681940	0.3809868867934243	0.1570787533130880
0.1858175427574963	0.7173833059280648	0.3948398037948000
0.9669133300429804	0.8574880305374188	0.1428203200682283
0.6269914798228631	0.1880600806313497	0.3766278947733707
0.7290746865712340	0.1306643654899078	0.1572322505157548
0.3926841923772564	0.4685041825995336	0.3949486325003969
0.9116329394534674	0.6968613546463900	0.0279170728385452
0.5706165982743630	0.0347974972670420	0.2675655728519326
0.2292490336777616	0.6323400317265646	0.1535758890812799
0.8960971200504922	0.9605833342636130	0.3978462496317718
0.2527519244143506	0.1094212898134215	0.1429225534795110
0.9210611063357768	0.4384829527304826	0.3764780066572766
0.9692903412440022	0.3610850861307207	0.1350078343867638
0.6332648563979862	0.6924987397018818	0.3852865072911013
0.9789925209647861	0.5981627888535309	0.1569615337788820

0.6415461945644092	0.9239334868342661	0.3946271492122515
0.8949284603321520	0.1979001376979604	0.0280728663445722
0.5746841459215716	0.5391736215403158	0.2677741665815683
0.7399933749846727	0.3699492941645550	0.1452211880101193
0.4067686130534919	0.7033252010042185	0.3988162976976349
0.1425577211125581	0.9244755784149866	0.0390067064909375
0.8119566903967869	0.2628025397640671	0.2728760753384278
0.6637630291318821	0.4710066224112902	0.0174843670052533
0.3355799429797842	0.8098543432971518	0.2621065341408412
0.1712297704226059	0.4826000108133067	0.0209156302360639
0.8345617861957844	0.8085463348813582	0.2582410953130477
0.4130830730427816	0.2149856968599496	0.0280721871128993
0.0747794901864132	0.5356957016479980	0.2676312584396377
0.4209456810915189	0.9383092908014752	0.0206088579768672
0.0841303221835929	0.2758579104686794	0.2584287785414033
0.1858365472071559	0.2184561360618647	0.0391328662021356
0.8469094718734872	0.5492715336094870	0.2725516512696309
0.1803244421684663	0.7144972439300845	0.0304742391021761
0.8441801016531911	0.0455038014004826	0.2801822793519782
0.6388723543364473	0.1927144295719307	0.0176866434064047
0.3005815280238662	0.5266307086288585	0.2623545022066178
0.3955274671565610	0.4660178078117257	0.0305757823823934
0.0647586479885560	0.7984608926569755	0.2803538564910624
0.2423523525375610	0.3719907151784678	0.1481323107275126
0.9018981056298241	0.7098767782213888	0.3872642542585837
0.8916660638510129	0.9673044968667915	0.0389725450544476
0.5608390830460812	0.2976744734946505	0.2725798182318188
0.9167440508104224	0.4456354405440022	0.0175451920852449
0.5842272349201368	0.7742961600223025	0.2621345403326695
0.6269477664743361	0.6887237505120438	0.0206966541526557
0.3017459540134485	0.0262986641259026	0.2584484685124856
0.6438670463934494	0.9295126194146370	0.0302829922974411
0.3117071730799172	0.2666950899285792	0.2806571454324436
0.2395121832279784	0.8679151825446640	0.1479103479458852
0.9180979742341604	0.2079692937492138	0.3872099367655407
0.4063593660818670	0.7031661313748869	0.0171062892213825
0.0736864666032168	0.0368981005273858	0.2704902976681710
0.8105730588328142	0.5256257770664872	0.1889757521246807
0.4896723863821861	0.8662035868319680	0.4339559038969955
0.6024756295353096	0.5547841039247740	0.1808395136619828
0.2592536027517762	0.8837819349181523	0.4234145278797697
0.8327505655844052	0.5318377638167170	-0.0030912090566694
0.5070034971108772	0.8669136472338678	0.2446160400512731
0.5780302145971647	0.3008328832963026	-0.0030177279436457
0.2426104628183142	0.6400941253778007	0.2446712184288792
0.0623947249433775	0.5076155908988409	0.1806994348985420
0.7345337754020420	0.8507465053307814	0.4234505871128691
0.8953462413300212	0.4557450312124620	0.1020734890211449
0.5577964948859419	0.7794143887611454	0.3456691932444721
0.1315976021689074	0.7026649049023799	0.1201573623599496
0.8028168502203270	0.0410516143070050	0.3647492359148409
0.8005827033576541	0.7632161474776158	0.1735550389448515
0.4731206726617175	0.1024850989477098	0.4157225760944332
0.9687825888473938	0.8737292357674444	0.0397537075334636
0.6419037265550348	0.2099671709644683	0.2903210956391589
0.6808690977142446	0.9783075966313576	0.1200773140445572
0.3483780552230571	0.3072506308815789	0.3651728964814631
0.0727402022496548	0.3097553776239705	0.1737172277544432
0.7396485670403046	0.6365323310144265	0.4157802904777943
0.8247827608392787	0.2992693175586489	0.1891613593330777

0.4867475484969337 0.6204381897534201 0.4341527915584614
0.0149945792051961 0.1411774390297981 0.0399565474214143
0.6780939599120687 0.4674323563247764 0.2904934027129007
0.8089374749002642 0.2767572779374552 -0.0031304136180577
0.4702941762090675 0.6027435493231588 0.2447816337773330
0.4074894384645012 0.4291700894421952 0.1202560991280189
0.0688882268817681 0.7616764586079856 0.3648630796413163
0.8804695154963592 0.1840902386692324 0.1136271607378698
0.5447492227924404 0.5187089535628006 0.3529077387976006
0.5844629123469711 0.2850766534168785 0.1890210829388621
0.2438582722808197 0.6235629464241037 0.4341677332605185
0.5550820915695746 0.0473372114300804 0.1807082462826699
0.2262436577888775 0.3757276436561856 0.4235995445991550
0.6704712728720521 0.2144534701246205 0.1021571488798110
0.3318766778561487 0.5522140594684749 0.3458946074427623
0.3470763242808563 0.0374889220836147 0.1737201433345354
0.0066904574958942 0.3702792987466113 0.4156707716057306
0.6541521012582406 0.4395671679363240 0.1020617690525857
0.3301531236848629 0.7779077137070356 0.3456519709494881
0.4137908552137228 0.2296173497941459 0.1135446197266712
0.0839647011181771 0.5653301705616857 0.3528593408069676
0.9257449958260431 0.6963142522917266 0.1134338790845677
0.5911697615454808 0.0255581740793344 0.3526894284442319
0.2362912817872400 0.0951820298970834 0.0398388304491713
0.8995444133082935 0.4319690486033740 0.2902151602855768
0.4813977058401538 0.8545467788310275 0.0699156877098467
0.1428920724253692 0.1923735521293346 0.3135273407435739
0.2691195533345582 0.8882797021645757 0.0628337650855238
0.9327201004778048 0.2224249120486654 0.3017719072289488
0.1712827419977042 0.1968072342617855 0.1254118541599361
0.8448394221103870 0.5328801468221422 0.3762094591195124
0.9138451514773730 0.9746270124522467 0.1252663911994221
0.5770839354199777 0.3117013887913648 0.3766200962205244
0.7289898380786251 0.8408048674700221 0.0627702697370151
0.3999122518830114 0.1776422625835299 0.3020304916081021
0.5690859128568667 0.7828562405033295 -0.0183709292883462
0.2291700666931274 0.1221337386089679 0.2265906817142750
0.8063494824490809 0.0355883155336140 -0.0004504768417310
0.4666212997151856 0.3697770107329261 0.2418883089776728
0.4648747697541286 0.0996017871464790 0.0503296851127179
0.1325871093564097 0.4283638031824790 0.2954873884315021
0.3064318218764450 0.5398600056093088 0.1712078538215910
0.9804223348062976 0.8746557526867637 0.4185400540835959
0.3394237591967657 0.3038128219005038 -0.0002814327890143
0.0131761544152667 0.6434733322217403 0.2417510372229853
0.7445413479749010 0.6450250551612577 0.0502249313964772
0.4056166722087223 0.9776003580697362 0.2954313734376716
0.4830243849233466 0.6285321850555450 0.0701156928436184
0.1594442719280283 0.9672344104868397 0.3134240576724561
0.3432992889048544 0.8038902684070144 0.1710236240310908
0.0040368397842650 0.1293915488062204 0.4186996469226590
0.1357690126941366 0.9393242634045423 0.1252958384140583
0.7978815548171523 0.2647028912397503 0.3755268517506891
0.0742295237310190 0.7707357384791877 -0.0003552390344887
0.7402118623077822 0.0966924176320952 0.2418992720524071
0.5533906537974991 0.5223347805608070 -0.0078383218272891
0.2112747283049061 0.8523319068776731 0.2347146197363674
0.2553201709396458 0.6269391955948922 0.0700647669345943
0.9180504836491976 0.9507578964681181 0.3133301804032051
0.2216882393845286 0.3810267843777117 0.0630645406873187

0.8876254698989259	0.7102056776135426	0.3017847183746264
0.3233162234095224	0.5403695682707673	-0.0181821622467671
0.0100503639867891	0.3649781678284134	0.0503634708308370
0.6822421946459867	0.7044380315762081	0.2954162586401491
0.3266840861729716	0.7862167216657191	-0.0183666806742366
0.9887840431776279	0.1073438875160558	0.2264312977030123
0.0785156160336196	0.5562071475774245	-0.0076657647706440
0.7510188681050749	0.8989462307584405	0.2346552304728116
0.5873384337670650	0.0310852346889262	-0.0079187535056669
0.2581939340755960	0.3596110505842447	0.2349451871334644
0.5708683372344731	0.7667352761556054	0.1710503533219342
0.2350403633228986	0.1058012615311418	0.4186790243841245
0.0030563442172888	0.8813568764833930	0.2264602812329305

Text S2. Solid-State ^{19}F and ^{115}In NMR

The solid-state ^1H and ^{19}F magic angle spinning (MAS) nuclear magnetic resonance (NMR) spectra were acquired on a Bruker ASCEND 400 MHz (9.4 T) solid-state DNP NMR spectrometer operating at Larmor frequencies of 400.202 and 376.532 MHz for ^1H and ^{19}F nuclei, respectively and equipped with a variable-temperature 2.5 mm triple-resonance HFX MAS NMR probehead. MAS conditions of 25-35 kHz were used to average the strong ^{19}F - ^{19}F nuclear dipole-dipole couplings and improve spectral resolution. For the solid-state MAS NMR measurements, the $\text{F}:\text{In}_2\text{O}_3$ cube NCs (3% InF_3) were mixed with KBr powder in a 1:1 ratio by mass. Rapid magic-angle-spinning of conductive materials within an external magnetic field for solid-state NMR measurements gives rise to substantial heating effects due to electromagnetic eddy currents.⁶ The added KBr serves dual purposes: 1] as a diluent to improve penetration of the radiofrequency (rf) pulses throughout the sample and reduce interparticle contacts that exacerbate heating effects, and 2] to provide a highly sensitive internal temperature probe by measurement of the temperature-dependent ^{79}Br T_1 relaxation times.⁷ For all of the solid-state NMR measurements, the internal sample temperature was determined to ± 1 K by analysis of the ^{79}Br T_1 relaxation times.

The 1D ^{19}F Hahn echo spectrum in Figure 4a was acquired at 35 kHz MAS, a sample temperature of 395 K, and using a 90° - τ - 180° - τ pulse sequence with rotor-synchronized τ delay times of one rotor period and 100 kHz rf pulses. The 2D $^1\text{H}\{^{29}\text{F}\}$ NMR correlation spectrum in Figure 4b was acquired at 25 kHz MAS and a sample temperature of 327 K using a 2D dipolar-mediated *Heteronuclear Multiple Quantum Correlation* (HMQC) pulse sequence, where the ^1H - ^{19}F nuclear dipole-dipole couplings were reintroduced using 24 rotor periods (0.96 ms) SR26₄¹¹ recoupling⁸ and 50 kHz rf power for recoupling. The ^{19}F excitation frequency was 210 ppm. A recycle delay time of 2.5 s was used with a t_1 increment step size of 20 μs , 20 t_1 increments, and 512 transients for a total acquisition time of 7 h. For the ^{19}F spin-lattice (T_1) relaxation analyses in Figure 6, The ^{19}F T_1 relaxation times at different temperatures were measured using a saturation-recovery pulse sequence with Hahn echo detection. An array of 18 saturation recovery delay times were used with 512 transients for each and a recycle delay of 0.2 s. The ^{19}F saturation-recovery curves were fit in MATLAB to a single exponential functional from zero for each isochromat across the ^{19}F NMR spectra to obtain the ^{19}F relaxation times at each temperature as functions of the ^{19}F shift.

The solid-state ^{115}In NMR spectrum of undoped bulk polycrystalline In_2O_3 was acquired at a magnetic field strength of 18.8 T, while the ^{115}In NMR spectrum of $\text{F}:\text{In}_2\text{O}_3$ was acquired at 19.6 T. As noted in the main text, the bulk undoped In_2O_3 (cubic bixbyite phase by XRD, Figure S16) exhibits an isotropic ^{115}In shift of 170 ppm, consistent with diamagnetic ^{115}In environments in the In_2O_3 lattice. By comparison, the ^{115}In spectrum of $\text{F}:\text{In}_2\text{O}_3$ cube NCs (3% InF_3) exhibits an isotropic ^{115}In shift of 1400 ppm, displaced more than 1200 ppm from the position for diamagnetic In_2O_3 . This displacement cannot be accounted for by the slightly different magnetic field strengths used to acquire the two spectra, and instead manifests a substantial Knight shift affecting the ^{115}In nuclei in the $\text{F}:\text{In}_2\text{O}_3$ NCs.

Figure S10. Solid-State 1D $^1\text{H}\{^{19}\text{F}\}$ MAS NMR Spectra

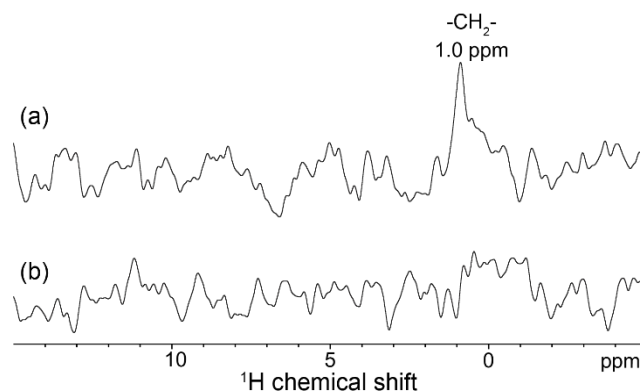


Figure S10. Solid-state 1D $^1\text{H}\{^{19}\text{F}\}$ MAS NMR spectra of F: In_2O_3 NCs (3% InF_3) diluted in 1:1 ratio by mass with KBr (the same sample as Figures 4 and 6), acquired at 9.4 T, 25 kHz MAS, at a sample temperature of 327 K, and with ^{19}F excitation at (a) -210 ppm, near the ^{19}F signals from InF_3 and surface In-F moieties, the same excitation frequency used to acquire the 2D $^1\text{H}\{^{19}\text{F}\}$ correlation spectrum in Figure 4b, and (b) 20 ppm, near the ^{19}F signals from F^- anions incorporated into the In_2O_3 lattice. No ^1H signal intensity is detected in the spectrum in (b), indicating that the F^- species embedded in the In_2O_3 lattice are not within nanoscale proximity of ^1H moieties on the organic surfactant molecules, within the detection limits of the measurement.

Figure S11. Quantitative ^{19}F MAS NMR Spectra

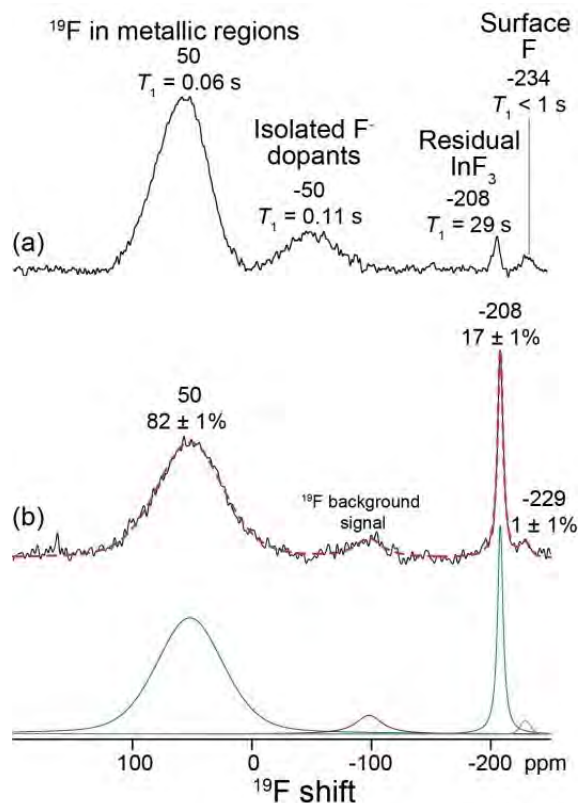


Figure S11. Solid state 1D (a) ^{19}F echo (same as Figure 4a) and (b) quantitative single-pulse ^{19}F MAS NMR spectra of $\text{F}:\text{In}_2\text{O}_3$ (3% InF_3) diluted with KBr in a 1:1 ratio by mass (the same sample as Figures 4, 6 and S10). The spectra were acquired at 9.4 T, 35 kHz MAS, and sample temperatures of 395 K. The ^{19}F spin-lattice T_1 relaxation times, measured under the same conditions, are given under the respective signal labels in (a). The dotted red line in (b) is the simulated ^{19}F spectrum, with the deconvolution shown offset below. The relative integrated signal intensities are shown above the corresponding signals. The ^{19}F signal at -50 ppm from isolated F^- dopant species is not detected or resolved in the quantitative 1D single-pulse ^{19}F spectrum in (b), indicating that the corresponding ^{19}F species comprise $<1\%$ of the total amount of fluorine atoms in the material. The relatively weak ^{19}F signal at ca. -100 ppm in (b) is a ^{19}F background signal from Teflon in the MAS NMR probehead, and was not included in the quantification of the ^{19}F NMR signals from the $\text{F}:\text{In}_2\text{O}_3$ NCs.

Figure S12. XRD Patterns

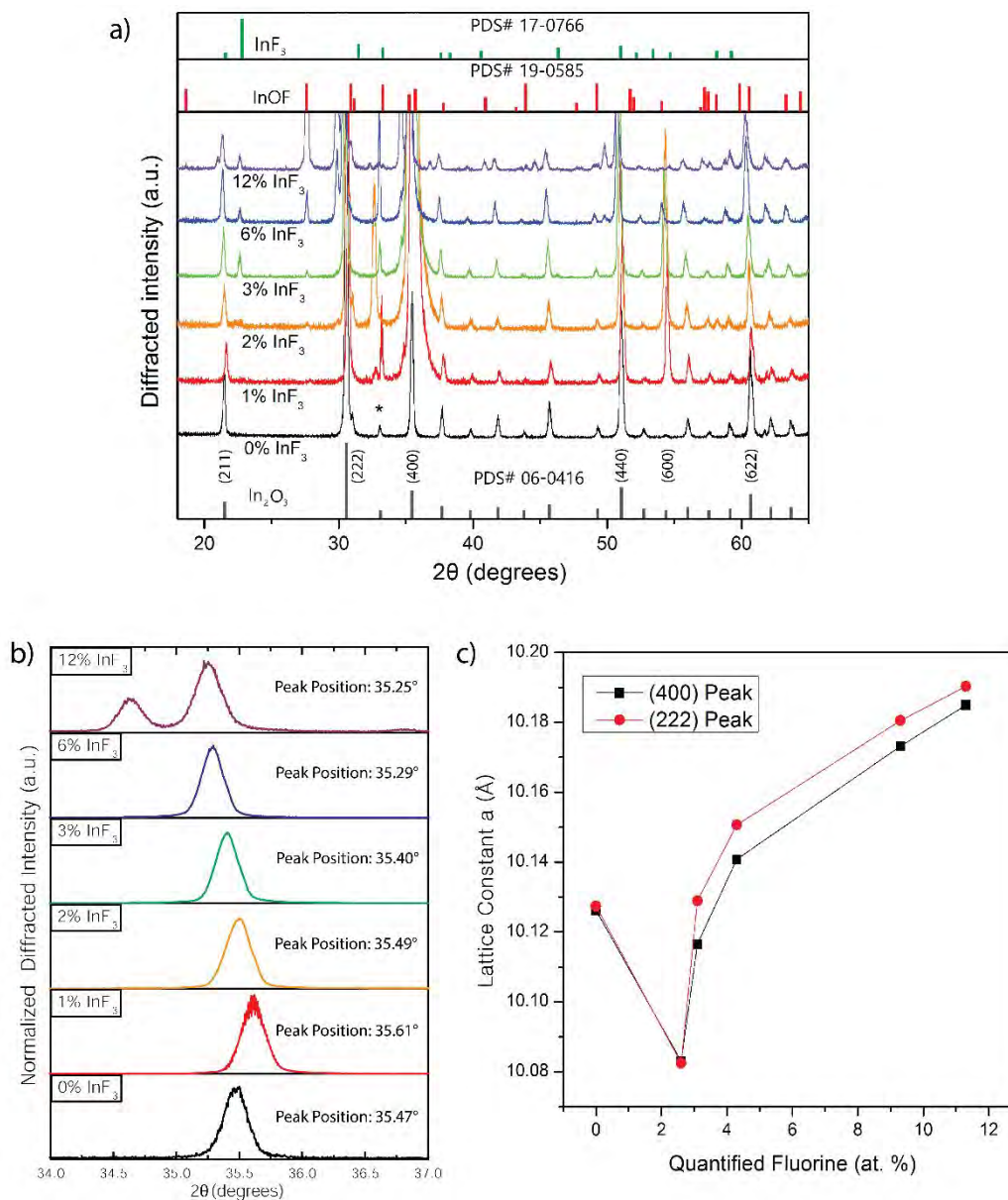
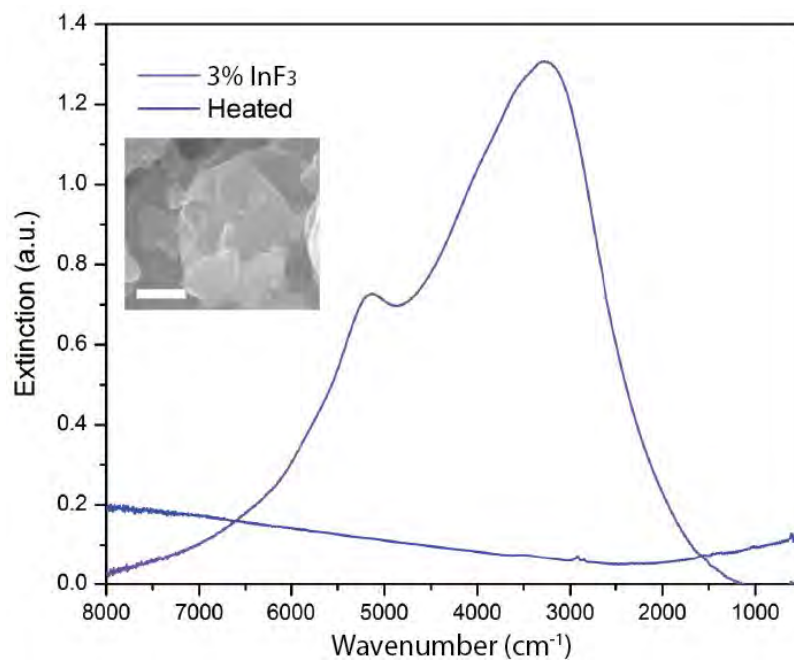


Figure S12. (a) XRD patterns from F: In_2O_3 NCs, with indium oxide (In_2O_3) PDS# 06-0416, indium fluoride (InF_3) PDS# 17-0766, and indium oxide fluoride (InOF) PDS# 19-0585 references. Asterisk denotes silicon substrate peak. (b) XRD patterns showing the shift of the (400) diffraction peak with InF_3 addition. (c) Rietveld refined⁹ XRD lattice constant shift correlated with fluorine incorporation quantified by EDX.

Figure S13. F:In₂O₃ Cube NC TGA



Medium	Refractive Index (n)	Peak Position (cm ⁻¹)
Tetrachloroethylene	1.50	3496
KBr	1.54	3306

Figure S13. KBr pellet sample FTIR spectra. F:In₂O₃ cube NC (3% InF₃) (purple), compared to F:In₂O₃ cube TGA sample (inset) heat treated at 1100 °C to remove fluorine (blue). Inset scale bar is 200 nm. LSPR peak position is observed to red-shift in higher refractive index KBr as compared to tetrachloroethylene medium (table).

Figure S14. Undoped In_2O_3 and F-doped In_2O_3 Band Structure

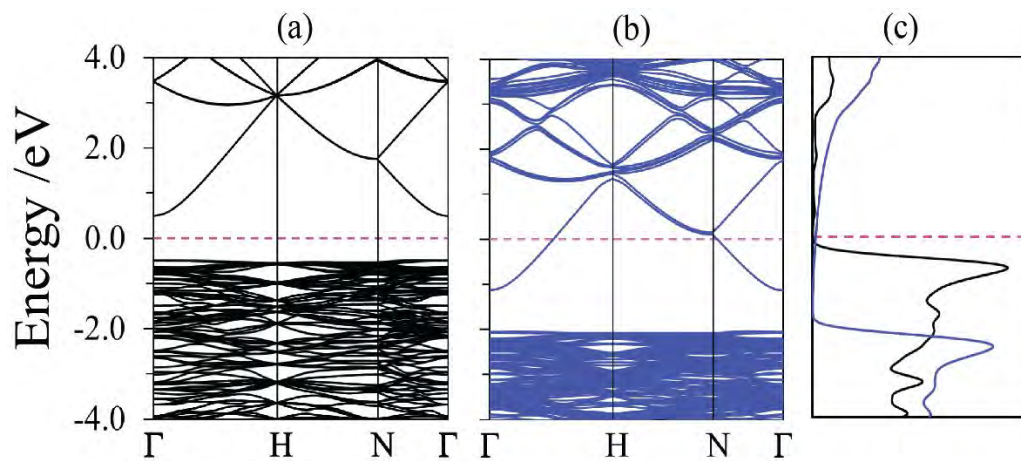


Figure S14. Band structures of (a) undoped In_2O_3 and (b) F-doped In_2O_3 (at the concentration of F : O = 1 : 47 by number of atoms). (c) Electronic density of states in undoped In_2O_3 (black lines) and F-doped In_2O_3 (blue lines), where Fermi level is set to zero. In F-doped In_2O_3 (F : O = 1 : 47), the Fermi level is 1.1 eV above the conduction band minimum.

Figure S15. EPR Spectra

Electron paramagnetic resonance (EPR) spectroscopy: Spectra were measured in a Bruker Biospin EMXplus 114 X-band spectrometer equipped with a liquid nitrogen variable temperature cryostat. Dried NC powders were loaded into quartz EPR tubes for the measurements.

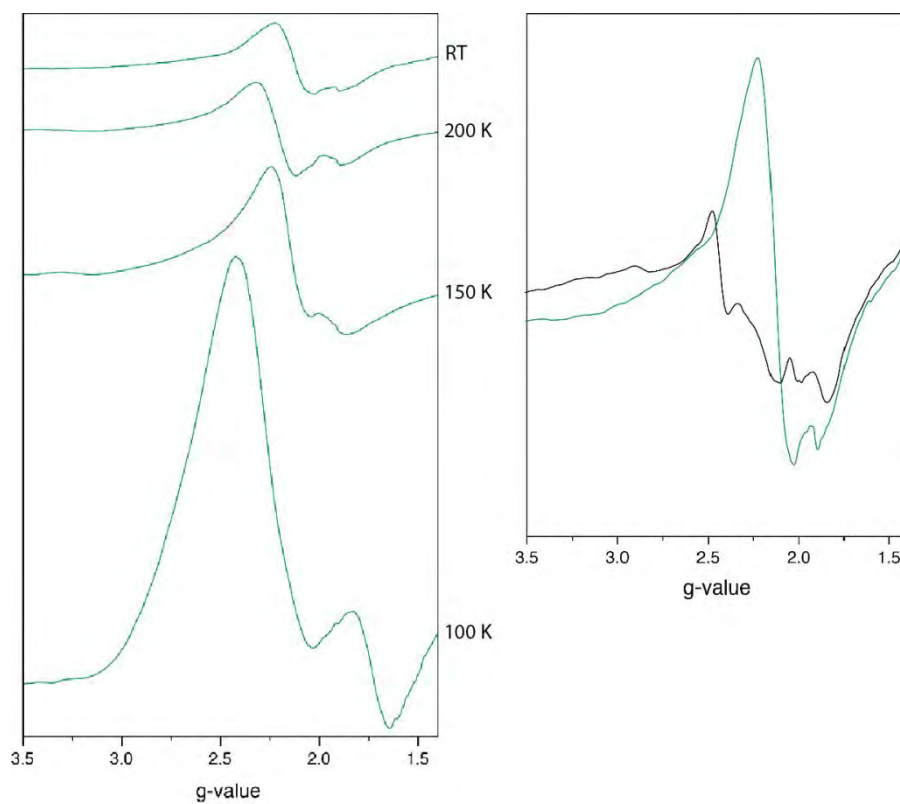


Figure S15. Temperature dependent X-band EPR spectra of (left) F:In₂O₃ cube NCs (3% InF₃), and (right) room temperature (RT) EPR spectrum F:In₂O₃ cube NC (3% InF₃) (green) and undoped In₂O₃ NCs (black).

Figure S16. Knight-Korringa Relation

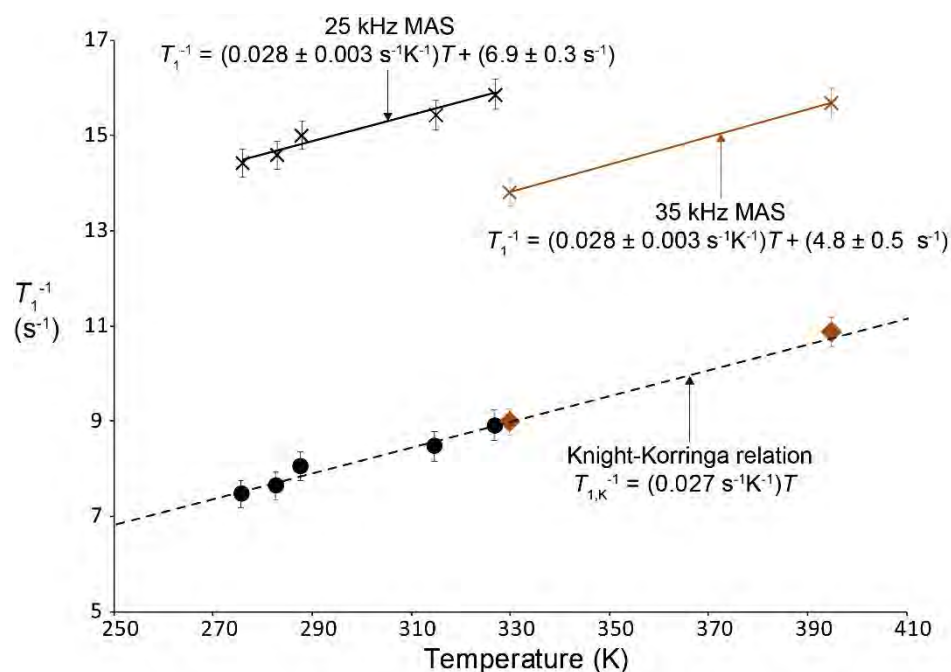


Figure S16. Plot of the experimental ^{19}F T_1^{-1} values (X symbols) measured at the peak maximum of the Knight shift distribution ($K = 100$ ppm) as a function of temperature. The black and brown data points were measured under MAS conditions of 25 and 35 kHz, respectively. The black and brown solid lines are linear fits to the data points, with the corresponding equations shown. The slopes of the linear fit equations are within experimental error of the slope predicted from the theoretical Knight-Korringa relation (black dashed line), and the intercept values are the temperature-independent $T_{1,0}^{-1}$ values for the different MAS conditions. The black circles and brown diamonds are the experimental data points corrected for the temperature-independent $T_{1,0}^{-1}$ terms (same points as in Figure 6c), which show excellent agreement with the Knight-Korringa relation, as discussed in the text. Error bars were calculated using standard error propagation methods and indicate uncertainties associated with the signal-to-noise ratios of the ^{19}F MAS NMR spectra and the quality of the fits to the ^{19}F saturation-recovery measurements.

Table S1. ^{115}In Simulated Lineshape Parameter

Parameters for the ^{115}In simulated lineshapes in Figure 7

	η^a	C_Q (MHz) ^b	δ_{iso} (ppm) ^c	Gaussian Line broadening ^d (ppm)
Bulk undoped In_2O_3	1	128	170	300
F: In_2O_3	1	139	1400	800

^a Asymmetry parameter

^b Quadrupolar coupling constant

^c Isotropic shift (including chemical and Knight shifts)

^d Gaussian line broadening apodization was applied to account for distributions of chemical shifts, Knight shifts, and/or quadrupolar parameters

Figure S17. XRD Pattern of Undoped Bulk In_2O_3

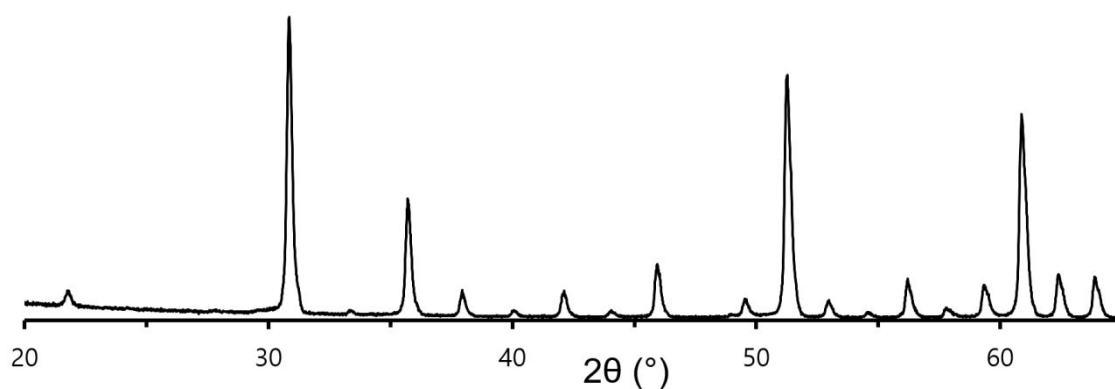


Figure S17. XRD pattern of the bulk undoped In_2O_3 material measured by solid-state ^{115}In NMR (same sample as Figure 7). All reflections are indexable to cubic bixbyite In_2O_3 .

Figure S18. Photograph of NC Dispersions

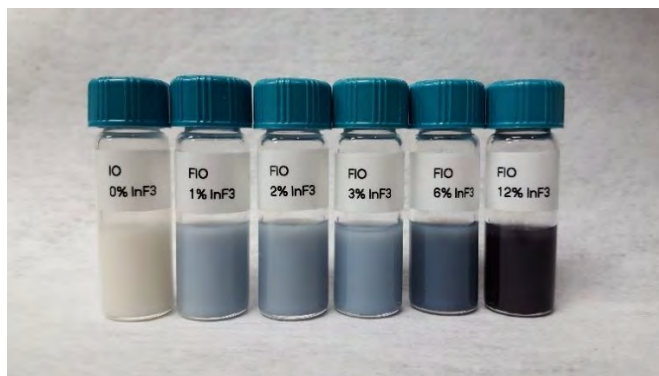


Figure S18. In_2O_3 and $\text{F}:\text{In}_2\text{O}_3$ NCs dispersed in toluene (10 mg/ml, average product yield: 54.3%) colloiddally synthesized with InF_3 dopant precursor ratio (0%, 1%, 2%, 3%, 6%, 12% InF_3) in increasing order, from left to right.

Figure S19. Drude Model Extinction Curve

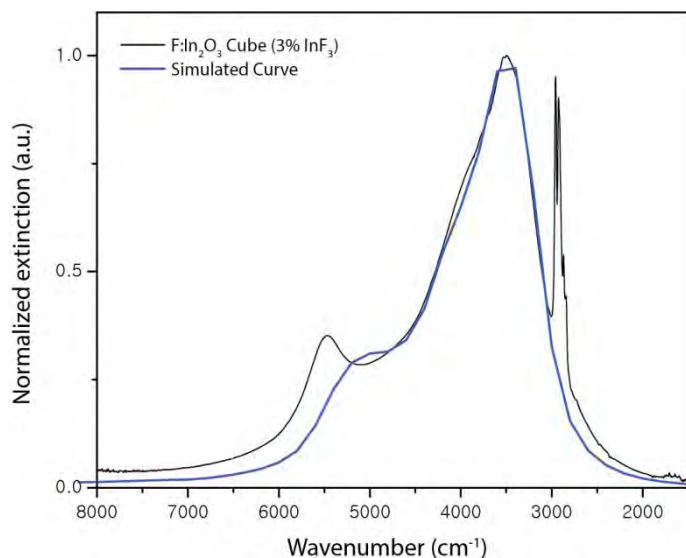


Figure S19. FTIR spectrum of $\text{F}:\text{In}_2\text{O}_3$ cube NCs (3% InF_3) dispersed in tetrachloroethylene (black) and simulated extinction curve (blue). A Drude model was used to define the NC dielectric function $\epsilon_p = \epsilon_\infty - \frac{\omega_p^2}{\omega^2 - i\gamma\omega}$ (Plasma frequency $\omega_p = 12300 \text{ cm}^{-1}$, damping parameter $\gamma = 600 \text{ cm}^{-1}$, $\epsilon_\infty = 4$). A cube shaped geometry model was input into the COMSOL design module based on experimental observations, using an edge-to-edge length of $a = 160 \text{ nm}$ and corner curvature of $a/20$, with surrounding medium refractive index of $n = 1.5$. The corresponding free electron concentration based on the derived plasma frequency was $n_e = 6.8 \times 10^{20} \text{ cm}^{-3}$.

Figure S20. F:In₂O₃ Cube NC Aliquot FTIR

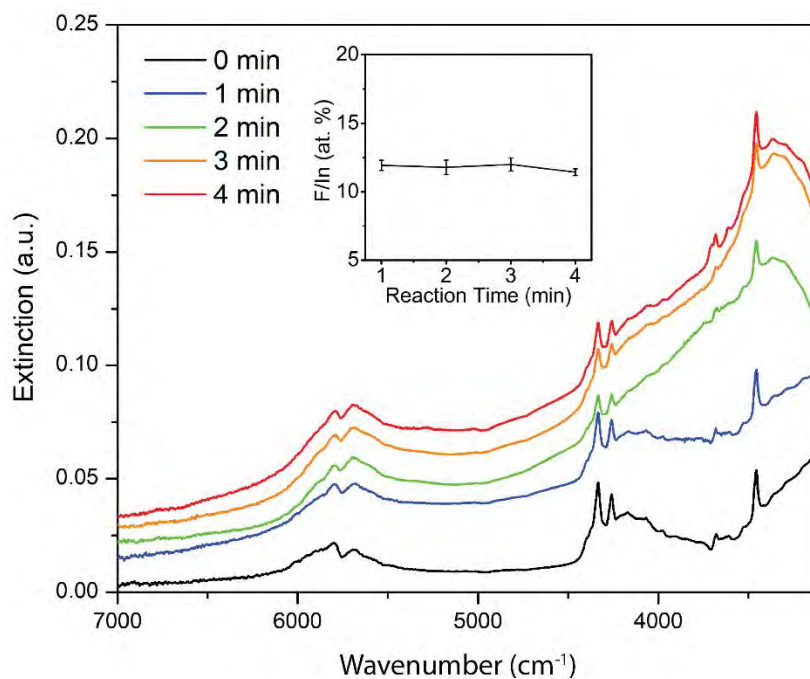


Figure S20. Liquid cell FTIR spectra of F:In₂O₃ cube NC (3% InF₃) aliquots taken from 0 min to 4 min growth reaction. The LSPR edge mode (higher wavenumber) and corner mode (lower wavenumber) LSPR peaks can be seen. (Inset) F:In₂O₃ cube NC F/In% atomic composition quantified by EDX retained as NC growth reaction time progress.

Text S3. Modal Deconvolution of Monochromated EELS Data

The spectrum images for the electron energy loss spectroscopy (EELS) analysis are all acquired as 60x60 pixels with 200 ms per pixel. We choose 200 ms per acquisition in order to leave the zero-loss peak (ZLP) unsaturated on the EELS detector. In EELS, the most prominent feature of any spectrum is the ZLP, which contains the signal for all electrons which did not interact with the sample or only underwent elastic scattering and hence lost no energy. Thus, the ZLP is important for accurate calibration of the energy offset, since the ZLP is centered on the true $\Delta E=0$ point of the spectrum.

Because the ZLP is so much higher in intensity than the plasmon peaks in the EEL spectra it needs to be removed before applying our deconvolution, as small variations in the ZLP result in much larger (in magnitude) changes to the spectrum and hence dominate the deconvolution. Additionally, to collect the data the NCs must be dispersed on an electron transparent substrate. We chose SiN due to its large band gap so that the surface plasmons in the cubes are as independent of the substrate as possible. However, SiN does have an infrared phonon signature at $\sim 1000\text{ cm}^{-1}$ which can be observed in EELS, we choose a background subtraction region from 1800 cm^{-1} - 2400 cm^{-1} to avoid influence from the SiN phonons and the ZLP from the EELS signal.

Lastly, due to the high level of monochromation the total signal in the beam is significantly reduced resulting in a high level of noise in the 200 ms spectra. To combat this we apply a local-low-rank (LLR) denoising algorithm to smooth the spectra and aid in the deconvolution.¹⁰ An example EEL spectrum acquired from the F:In₂O₃ cubes is shown in Figure S21. Here, the ZLP can be observed extending off the top of the figure as we approach lower energies, along with the shoulder corresponding to the SiN phonon. The denoising and background subtraction method removes the influence of noise as well as the ZLP while still accurately representing the as-acquired data.

To deconvolve the different plasmon modes in the signal, we use non-negative matrix factorization (NMF) a technique which deconvolves the spectral imaging (SI) dataset into all-positive spatial and spectral components and has been shown to provide accurate deconvolution in noisy data.¹¹ In NMF the number of components is chosen as an input parameter, that controls the dimensions of the optimized matrices. Cube structures like those examined in these experiments are known to have dominant corner and edge modes, so we compared the three structures in terms of a 2-component NMF deconvolution, which is shown in Figure S22.

Here it can be seen that the corner and edge modes are clearly separated by the NMF deconvolution, since the two spatial components are shown to be highly localized to the corners and edges respectively. Additionally, it can be seen (especially in the cases of the cube and concave cube structures) that the edge mode is a combination of multiple peaks. The two dominant peaks are likely the edge and face plasmon modes of the cubes, which are spatially overlapped in the 2D projection when the electron beam passes normal to the edges. This is supported by the fact that in the octapod structure, where the faces of the structure are highly recessed with respect to the edges, there is only one strongly observed peak. The peaks are found by fitting a Lorentzian to a small region around each peak, which are the peak

centers reported in Figure 9 of the main text. For the edge modes in the concave cubes and cubes where there are two distinct peaks, we report the average of the two in the main text.

It is also important to consider deconvolutions with a higher number of output components. In Figure S23 we show the NMF deconvolution of the spectrum image for the 3% InF₃-doped nanocube with 2, 3, 4, and 5 output components. The 2-component fit is a duplication of the one observed in Figure S22, but overlaid with the FTIR data. Here, the edge peaks closely overlap with the high energy FTIR peak, but the corner mode is observed at a significantly higher energy than the dominant low energy FTIR peak. However, in the 3-component fit it can be seen that now the corner mode has been split into a higher and lower energy component, and the low energy component is now much closer to the expected FTIR peak. The result is not so surprising, since the liquid cell FTIR observes the ensemble behavior of many cubes, while the EELS isolates individual locations on a single nanocube, and more importantly, such plasmon modes are highly sensitive to the dielectric environment. In FTIR, the cubes are surrounded by a fluid with $n > 1$, while the EELS measurements are conducted with an ultra-high vacuum surrounding the NC and one side of the NC adjacent to the SiN membrane. It is known that the interaction between LSPR modes and dielectric substrates causes shifts in plasmon peak energies, so likely the presence of the SiN membrane is significantly responsible for the disparities between energies of the modes observed by FTIR and EELS. This is supported by the 4-component deconvolution, where now the edge mode has also been split into a low-energy and high-energy component, indicating that substrate interaction has caused a split into a proximal and distal mode.¹² We also attempted to fit higher numbers of components, but at the 5-component fit the NMF deconvolution begins to return signals spatially localized in the background region with non-physical spectra, so we limited our analysis to four components or fewer.

Figure S21. EELS Background Subtraction and Denoising

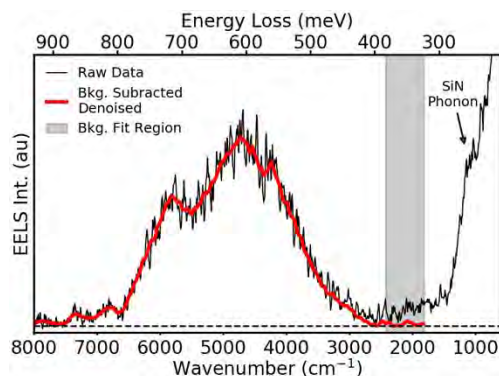


Figure S21. F:In₂O₃ cube (3% InF₃) NC raw EELS spectrum data, with zero loss background subtraction and LLR-denoising.

Figure S22. Corner and Edge Modes for 1%, 2%, and 3% InF₃ Doping Concentrations

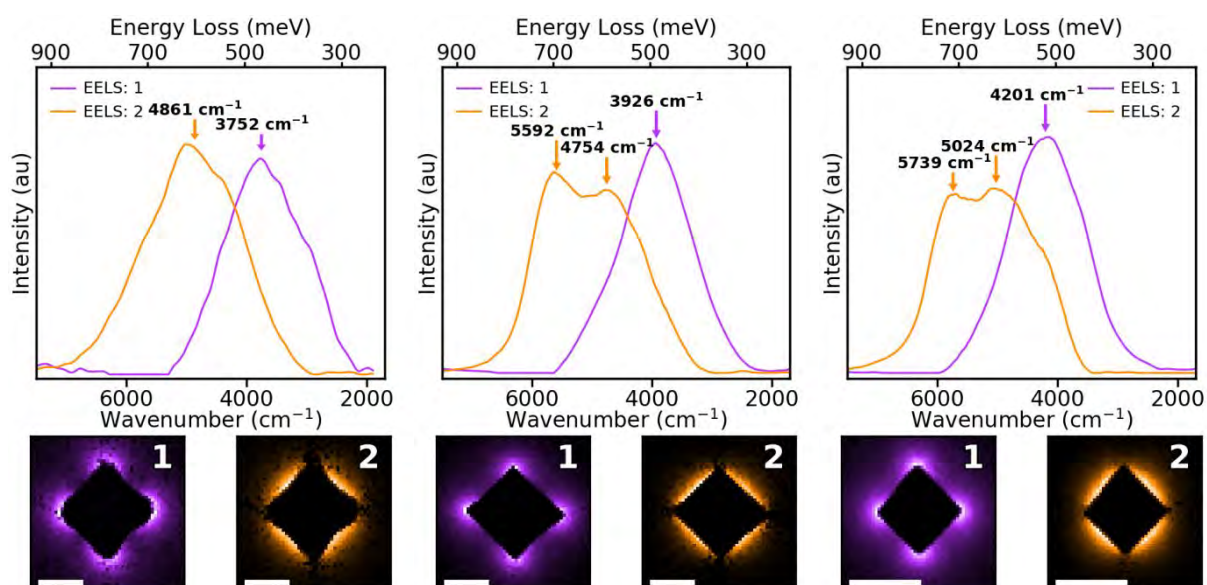


Figure S22. 2-Component non-negative matrix factorization (NMF) deconvoluted EELS signal and map of (left) F:In₂O₃ concave cube (1% InF₃) NC, (middle) F:In₂O₃ sharp concave cube (2% InF₃) NC, and (right) F:In₂O₃ cube (3% InF₃) NC.

Figure S23. Effect of Number of Components on Deconvoluted Plasmon Modes

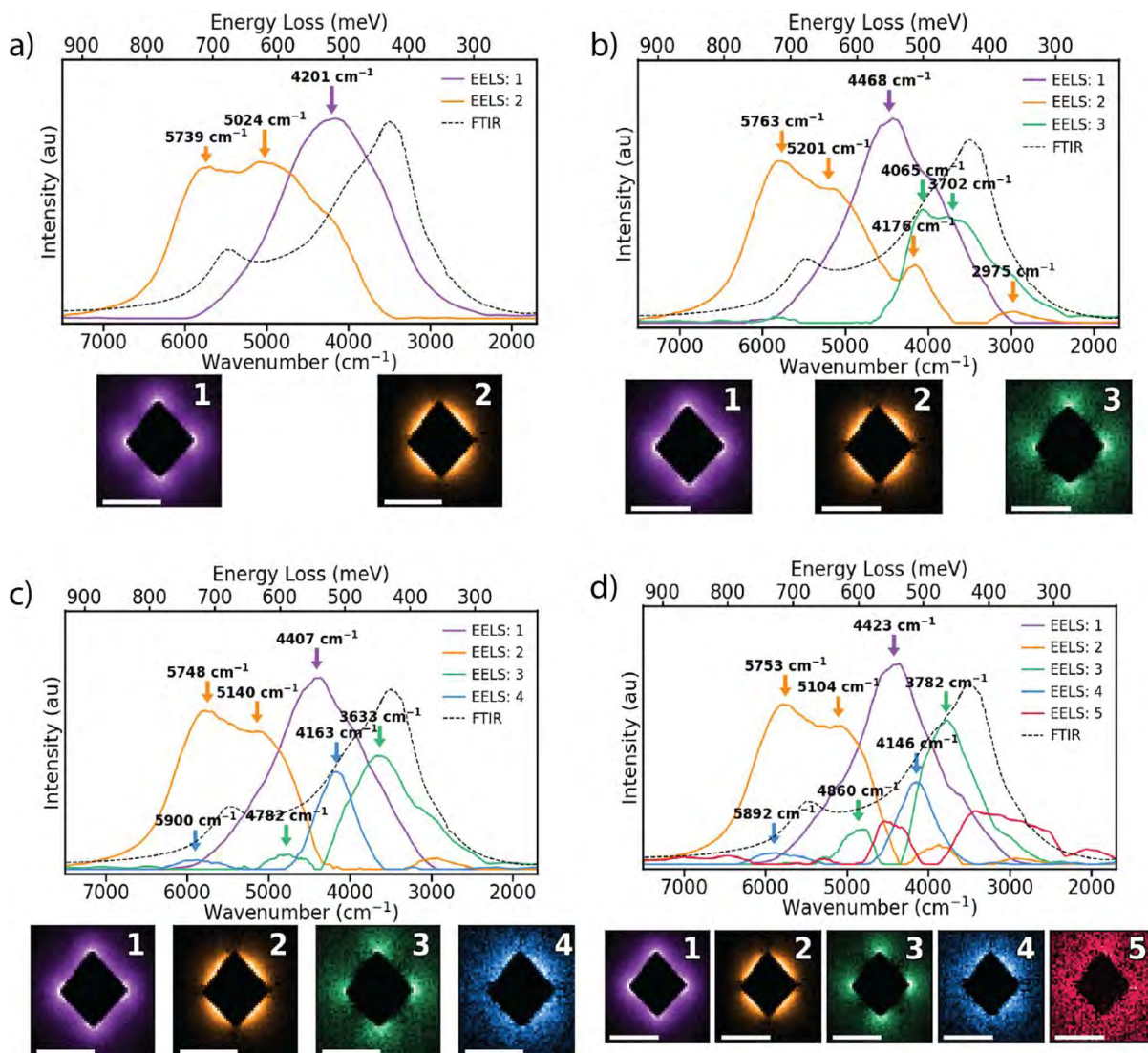


Figure S23. Higher component NMF deconvolutions of 3% InF₃ NC. (a) 2-Component NMF deconvolution. (b) 3-Component NMF deconvolution showing the splitting of corner mode into two different components. (c) 4-Component NMF deconvolution showing the splitting of the edge mode into two different components. (d) 5-Component deconvolution showing that now NMF begins to interpret noise and background as signal.

Text S4. Surface Fluorine Estimation

To estimate surface fluorine in F:In₂O₃ cube NC (3% InF₃), ¹⁹F NMR fluorine quantification is used in conjunction with total quantified fluorine from EDX. Relative bulk and surface ¹⁹F NMR signal is used to define the number of surface fluorine atom in DFT simulations of F:In₂O₃ cube NC. The ideal bulk cubic bixbyite phase In₂O₃ has a unit cell parameter of a = 1.012 nm, containing 32 In atoms, 48 O atoms. Substituting 4 F atoms per unit cell provides a F/In at.% ratio of $\frac{F_{bulk}}{In} = \frac{4}{32} = 12.50\%$. Fluorine atomic content in F:In₂O₃ cube NCs (3% InF₃) quantified by EDX, sensitive to bulk fluorine due to deep secondary electron profiling depth, is at 11.76% (F/In% ratio), corresponding to approximately 3.70 F atoms per unit cell.

$$F_{bulk} = 3.70 \text{ F atom/nm}^3$$

The quantification of our ¹⁹F NMR results indicates that 82% of the F is in a metallic environment and the relatively weak 1% signal identified as surface fluorine based on ¹H{¹⁹F} MAS NMR, allowing an experimental determination of the surface-to-bulk fluorine ratio to be obtained.

$$\text{NMR surface-to-bulk ratio: } \frac{F_{NMR\ surface}}{F_{NMR\ bulk}} = \frac{1\ atom}{82\ atom} = 1.22\ \%$$

The total surface fluorine on NC is estimated from the NMR surface-to-bulk ratio, bulk fluorine quantification, volume and surface area from 162.1 nm edge-to-edge sized F:In₂O₃ cube NC (3% InF₃). The estimation provides surface fluorine atom coverage of 1.14 F atom/nm². It can be ascertained that one F atom substitution for DFT surface modeling (1 F atom/nm²) reasonably corresponds to the experimental surface fluorine quantification.

$$\begin{aligned} \text{Surface F Estimation: } & V \times F_{bulk} \times \frac{F_{NMR\ surface}}{F_{NMR\ bulk}} \div S \\ (162.1\ nm)^3 \times 3.70\ F\ atom/nm^3 \times 1.22\ \% \div (6 \times (162.1\ nm)^2) &= 1.14\ F\ atom/nm^2 \end{aligned}$$

An ideal uniformly doped F:In₂O₃ cube NC can be assumed have surface-to-bulk fluorine atomic ratio corresponding to the surface-to-volume ratio of cubic shaped NC. Due to the large nature of 162.1 nm edge-to-edge sized NC cube, the surface-to-bulk ratio is low with most of fluorine found internally in the sub-surface NC lattice. The estimated fluorine surface coverage in F:In₂O₃ cube is physically within reasonable bounds.

$$F_{surface}(atom) : F_{bulk}(atom) = Surface\ (nm^3) : Volume\ (nm^3)$$

$$\text{Ideal surface-to-bulk ratio: } \frac{S}{V} = \frac{6 \times (162.1\ nm)^2}{(162.1\ nm)^3} = \frac{F_{surface}}{F_{bulk}} = 3.70\ \%$$

References

- (1) Kresse, G.; Furthmüller, J. Efficient Iterative Schemes for Ab Initio Total-Energy Calculations Using a Plane-Wave Basis Set. *Phys. Rev. B* **1996**, *54* (16), 11169–11186.
- (2) Kresse, G.; Joubert, D. From Ultrasoft Pseudopotentials to the Projector Augmented-Wave Method. *Phys. Rev. B* **1999**, *59* (3), 1758–1775.
- (3) Perdew, J. P.; Burke, K.; Ernzerhof, M. Generalized Gradient Approximation Made Simple. *Phys. Rev. Lett.* **1996**, *77* (18), 3865–3868.
- (4) Monkhorst, H. J.; Pack, J. D. Special Points for Brillouin-Zone Integrations. *Phys. Rev. B* **1976**, *13* (12), 5188–5192.
- (5) Sadoc, A.; Body, M.; Legein, C.; Biswal, M.; Fayon, F.; Rocquefelte, X.; Boucher, F. NMR Parameters in Alkali, Alkaline Earth and Rare Earth Fluorides from First Principle Calculations. *Phys. Chem. Chem. Phys.* **2011**, *13* (41), 18539–18550.
- (6) Yesinowski, J. P.; Ladouceur, H. D.; Purdy, A. P.; Miller, J. B. Electrical and Ionic Conductivity Effects on Magic-Angle Spinning Nuclear Magnetic Resonance Parameters of CuI. *J. Chem. Phys.* **2010**, *133* (23), 234509.
- (7) Thurber, K. R.; Tycko, R. Measurement of Sample Temperatures under Magic-Angle Spinning from the Chemical Shift and Spin-Lattice Relaxation Rate of ⁷⁹Br in KBr Powder. *J. Magn. Reson.* **2009**, *196* (1), 84–87.
- (8) Brouwer, D. H.; Kristiansen, P. E.; Fyfe, C. A.; Levitt, M. H. Symmetry-Based ²⁹Si Dipolar Recoupling Magic Angle Spinning NMR Spectroscopy: A New Method for Investigating Three-Dimensional Structures of Zeolite Frameworks. *J. Am. Chem. Soc.* **2005**, *127* (2), 542–543.
- (9) Toby, B. H.; Von Dreele, R. B. GSAS-II: The Genesis of a Modern Open-Source All Purpose Crystallography Software Package. *J. Appl. Crystallogr.* **2013**, *46* (2), 544–549.
- (10) Spiegelberg, J.; Idrobo, J. C.; Herklotz, A.; Ward, T. Z.; Zhou, W.; Ruzs, J. Local Low Rank Denoising for Enhanced Atomic Resolution Imaging. *Ultramicroscopy* **2018**, *187*, 34–42.
- (11) Nicoletti, O.; Peña, F. de la; Leary, R. K.; Holland, D. J.; Ducati, C.; Midgley, P. A. Three-Dimensional Imaging of Localized Surface Plasmon Resonances of Metal Nanoparticles. *Nature* **2013**, *502* (7469), 80–84.
- (12) Li, G.; Cherqui, C.; Bigelow, N. W.; Duscher, G.; Straney, P. J.; Millstone, J. E.; Masiello, D. J.; Camden, J. P. Spatially Mapping Energy Transfer from Single Plasmonic Particles to Semiconductor Substrates via STEM/EELS. *Nano Lett.* **2015**, *15* (5), 3465–3471.